Radio Frequency Non-destructive Testing and Evaluation of Defects under Insulation

Hong Zhang, BEng MSc

A thesis submitted for the degree of Doctor of Philosophy

School of Electrical and Electronic Engineering

Faculty of Science, Agriculture and Engineering

June 2014

Abstract

The use of insulation such as paint coatings has grown rapidly over the past decades. However, defects and corrosion under insulation (CUI) still present challenges for current non-destructive testing and evaluation (NDT&E) techniques. One of such challenges is the large lift-off introduced by thick insulation layer. Inaccessibility due to insulation leads corrosion and defects to be undetected, which can lead to catastrophic failure. Furthermore, lift-off effects due to the insulation layers reduce the sensitivities. The limitations of existing NDT&E techniques heighten the need for novel approaches to the characterisation of corrosion and defects under insulation.

This research project is conducted in collaboration with International Paint®, and a radio frequency non-destructive evaluation for monitoring structural condition is proposed. High frequency (HF) passive RFID in conjunction with microwave NDT is proposed for monitoring and imaging under insulation. The small-size, battery-free and cost-efficient nature of RFID makes it attractive for long-term condition monitoring. To overcome the limitations of RFID-based sensing system such as effective monitoring area and lift-off tolerance, microwave NDT is proposed for the imaging of larger areas under thick insulation layers. Experimental studies are carried out in conjunction with specially designed mild steel sample sets to demonstrate the detection capabilities of the proposed systems.

The contributions of this research can be summarised as follows. Corrosion detection using HF passive RFID-based sensing and microwave NDT is demonstrated in experimental feasibility studies considering variance in surface roughness, conductivity and permeability. The lift-off effects introduced by insulation layers are reduced by applying feature extraction with principal component analysis and non-negative matrix factorisation. The problem of thick insulation layers is overcome by employing a linear sweep frequency with PCA to improve the sensitivity and resolution of microwave NDT-based imaging. Finally, the merits of microwave NDT are identified for imaging defects under thick insulation in a realistic test scenario. In conclusion, HF passive RFID can be adapted for long term corrosion monitoring of steel under insulation, but sensing area and lift-off tolerance are limited. In contrast, the microwave NDT&E has shown greater potential and capability for monitoring corrosion and defects under insulation.

Acknowledgements

There are many people I wish to express my gratitude for helping me during the past years of PhD study. Firstly, special thanks to Professor Gui Yun Tian, my supervisor for providing regular help and guidance on this project.

I would like to thank my colleagues: Dr. John Wilson, Dr. Liang Cheng, Prof. Xianzhang Zuo, Dr. Yunze He, Dr. Libing Bai, Prof. Mengchun Pan, Dr. Aijun Yin, Dr. Danping Huang, Dr. Wei Li, Mr Jianping Peng, Mr Song Ding, Dr. Omar Bouzid, Dr. Abdul Qubaa, Mr Kongjing Li and all in the Sensor Technology research team at Newcastle University, who have provided fruitful discussions and advices.

Special thanks to Dr. Bin Gao, Mr Ali Imam Sunny and Dr. Mohammed Alamin for their advices and efforts to complete the thesis.

My deepest thanks go to my parents and families, for always supporting and encouraging me during my education.

Last but not least, I offer my regards and blessing to all those who support me in any respect during the completion of the study.

Contents

List of Figures and Tables

Abbreviations

AE	Acoustic Emission
ASTM	American Society for Testing and Materials
CUI	Corrosion Under Insulation
EC	Eddy Current
EIS	Electrochemical Impedance Spectroscopy
ECPT	Eddy Current Pulsed Thermography
EM	Electromagnetic
EMATs	Electromagnetic Acoustic Transducers
FBG	Fibre Bragg Grating
FFT	Fast Fourier Transform
GMR	Giant Magneto Resistance
HF	High Frequency
IC	Integrated Circuit
IR	Infrared
LF	Low Frequency
MFL	Magnetic Flux Leakage
MNDT	Microwave NDT
MPI	Magnetic Particle Inspection
NDE	Non-Destructive Evaluation
NDT	Non-destructive Testing
NDT&E	Non-Destructive Testing and Evaluation

NMF	Non-negative Matrix Factorization
PC	Principal Component
PCA	Principal Component Analysis
PEC	Pulsed Eddy Current
PIGs	Pipeline Inspection Gauges
QNDE	Quantitative Non-Destructive Evaluation
RF	Radio Frequency
RFID	Radio Frequency Identification
SCC	Stress Corrosion Cracking
SHM	Structural Health Monitoring
SNR	Signal-to-Noise Ratio
SVD	Singular Value Decomposition
THz	Terahertz
UHF	Ultra High Frequency
UT	Ultrasonic Testing
VI	Visual Inspection

List of Publications

Journal Papers

[J1] H. Zhang, B. Gao, G. Y. Tian, W. L. Woo, L. Bai, "Metal defects sizing and detection under thick coating using microwave NDT," *NDT & E International,* vol. 60, pp. 52-61, 2013.

[J2] H. Zhang, B. Gao, G. Y. Tian, W. L. Woo, A. Simm, "Spatial-Frequency Spectrum Characteristics Analysis With Different Lift-Offs for Microwave Nondestructive Testing and Evaluation Using Itakura-Saito Nonnegative Matrix Factorization," *IEEE Sensors Journal,* vol. 14, no. 6, pp. 1822-1830, 2014.

[J3] B. Gao, H. Zhang, W. L. Woo, G. Y. Tian, L. Bai, A. Yin, "Smooth Nonnegative Matrix Factorization for Defect Detection Using Microwave Nondestructive Testing and Evaluation," *IEEE Transactions on Instrumentation and Measurement,* vol. 63, no. 4, pp. 923-934, 2014.

[J4] Y. He, G. Y. Tian, H. Zhang, M. Alamin, A. Simm, P. Jackson, "Steel Corrosion Characterization Using Pulsed Eddy Current Systems," *IEEE Sensors Journal,* vol. 12, no. 6, pp. 2113-2120, 2012.

[J5] Y. K. Zhu, G. Y. Tian, R. S. Lu, H. Zhang, "A review of optical NDT technologies," *Sensors,* vol. 11, no. 8, pp. 7773-7798, 2011.

[J6] Y. He, M. Pan, G. Y. Tian, D. Chen, Y. Tang, H. Zhang, "Eddy current pulsed phase thermography for subsurface defect quantitatively evaluation," *Applied Physics Letters,* vol. 103, no. 14, pp. 144108-144108-4, 2013.

[J7] Y. He, G. Y. Tian, M. Pan, D. Chen, H. Zhang, "An investigation into eddy current pulsed thermography for detection of corrosion blister," *Corrosion Science,* vol. 78, no. 0, pp. 1-6, 2014.

Conference Papers

[C1] H. Zhang, G. Y. Tian, Y. He, P. Jackson, "Corrosion Detection using High Frequency Radio Frequency Identification Technology," *50th Annual Conference of The British Institute of Non-Destructive Testing*, Telford, UK, 2011.

[C2] H. Zhang, G. Y. Tian, Y. He, X. Zuo, "Defect depth effects in Pulsed Eddy Current thermography." *Proceedings of the 17th International Conference on Automation & Computing*, Huddersfield, UK, 2011.

[C3] H. Zhang, G. Y. Tian, A. Simm, M. Alamin, "Electromagnetic methods for corrosion under paint coating measurement." *International Symposium on Precision Engineering Measurement and Instrumentation*, Chengdu, China, 2012. (Invited Paper)

[C4] I. Dapo Adewale, H. Zhang, G. Y. Tian, T. Hope, "Defect mapping of steel substrate under fire protection layer using EM NDE methods." *Far East Forum on Nondestructive Evaluation/Testing: New Technology & Application (FENDT)*, pp. 166-171, Jinan, China, 2013.

[C5] G. Y. Tian, L. Cheng, M. Alamin, H. Zhang, Y. He, "Electromagnetic non-destructive methods for corrosion characterisation", *ISEM 2011-15th International Symposium on Applied Electromagnetics and Mechanics*, Napoli, Italy, 2011.

[C6] G. Y. Tian, Y. He, M. Alamin, H. Zhang, P. Jackson, "Corrosion characterisation using pulsed eddy current sensor systems." *Fifth International Conference on Sensing Technology (ICST)*, Palmerston North, New Zealand, 2011.

[C7] Y. He, G. Y. Tian, L. Cheng, H. Zhang, P. Jackson, "Corrosion Characterisation under Coating Using Pulsed Eddy Current Thermography," *50th Annual Conference of The British Institute of Non-Destructive Testing*, Telford, UK, 2011.

[C8] Y. He, G. Y. Tian, L. Cheng, H. Zhang, P. Jackson, "Parameters influence in steel corrosion evaluation using PEC thermography", *Proceedings of the 17th International Conference on Automation & Computing*, Huddersfield, UK, 2011.

Chapter 1. Introduction

This chapter starts with motivation of the study to detail the current situation and address challenges to existing non-destructive testing and evaluation (NDT&E) techniques for monitoring defects and corrosion under insulation (CUI). High frequency RFID and microwave NDT are then proposed for the evaluation of such corrosion and defects. Major research achievements are then listed. Finally, the structure of this thesis is described.

1.1 Research Background

Non-destructive testing and evaluation refers to the implementation of the defect detection of material, which at the same time does not affect the material's future performance. Corrosion is the deterioration in material properties due to interaction with the environment [1], and materials which corrode including metals and alloys, non-metals, woods, ceramics, plastics and composites [2].

Due to its relatively low cost, mechanical strength and ease of manufacture, mild steel is the preferred metal for use in many applications. Its main disadvantage is that it corrodes easily unless adequately protected, and then rapidly loses strength which will lead to structural failure. For better corrosion resistance, the steel is usually coated with insulation. A large number of different types of insulations are used to protect a variety of structural engineering materials from corrosion and to provide lubrication and thermal insulation [3].

At 10:30am on Friday 22nd November 2013, an explosion occurred when a pipeline which was leaking oil caught fire in Qingdao China, and 55 people were killed, as shown in Figure 1.1. The pipelines were not properly maintained, resulting in the original oil spills, and following these leaks the emergency procedures were insufficient.

For these pipelines, preventative measures using more efficient diagnostic NDT&E methods are required.

(a) (b)

Figure 1.1 (a) The 2013 pipeline explosion in Qingdao damaged cars and the road in Shandong province. (b) 55 people were killed after the explosion [4].

Corrosion and defects under insulation are major problems throughout the oil and gas industry. Moreover, not only are petrochemical industries affected, but also any power and manufacturing industries where pipelines are fitted with insulation. Furthermore, this problem is not specific to a particular geographical location, but occurs in facilities and pipelines all over the world.

CUI is associated mainly with the steel components of power plants and pipework. Undetected corrosion may develop beneath insulation which can lead to failure without curb. When steel is in contact with water and oxygen, it is likely to corrode. Usually, there are spaces within insulated plant and pipework which water can enter from the outside. This ingress of water into the insulation material results in water and air gaining access to the metal surface. The infiltration of water into insulation may be caused by poorly designed or installed protective coating finish, the breaking of cladding joint sealant, or cladding being removed and not properly replaced.

CUI is an extremely costly problem for industries and commercial sectors worldwide, and it has a significant impact on the global economy. However, the inspection of CUI would be very costly if all insulation had to be removed. Normally, localised checks

require inspection windows which are cut into the insulation. However, the selection of inspection areas and efficient examination require trained inspectors. In order to improve the efficiency of examination, various NDT&E methods have been adopted to detect corrosion and defects under insulation without removing the insulation [5-11], each of which has different capabilities. These NDT techniques are then used to target problem areas where further inspection is needed. However, some critical equipment may be inaccessible due to full insulation, and so the removal of insulation to secure proper inspection may still be required.

One reason why CUI is particularly challenging for NDT that, along with the usual problem of accurately detecting and quantifying corrosion, there may be large distances between the sensor and the metal surface due to the presence of the insulation layer, this distance is known as the lift-off. The immediate effect of a large lift-off is the reduction of sensitivity to small changes in corrosion or small defects such as metal loss. This is particularly problematic for traditional electro-magnetic NDT techniques, such as eddy current (EC) and magnetic flux leakage (MFL) methods which typically require surface/near surface inspection. Although commercial eddy current-based methods exist that can operate inspection through thick layers of insulation, they require large currents and bulky equipment. In addition, insulation layers may be variations in thickness, resulting in variations in lift-off which are also known as lift-off effects. This variation can cause errors in the detection and measurement of corrosion.

The importance of detection methods under insulation is threefold. Firstly, the loss of material and failures of various structures and components caused by corrosion will result in a considerable economic impact. Recent studies have estimated that the direct cost of corrosion is between 3% and 4% of the gross domestic product (GDP) in every country [12]. Secondly, the failure of vessels, petrochemical plants and aircraft parts may lead to thousands of personal injuries and deaths, yet safety can be improved with

improved detection methods. Corrosion detection under insulation potentially represents a very large market, which would benefit from economies of scale thus lowering costs [13]. Thirdly, early corrosion detection can conserve resources, since corrosion leads to the wastage of energy, water and materials.

To address the aforementioned problems, this research investigates how radio frequency based methods can be applied for detection and monitoring under insulation. Because of the insulation can be easily penetrated by radio frequency signals. Meanwhile, multiple characters (such as amplitude, phase etc.) can be provided by using radio frequency. Therefore, high frequency RFID-based sensing in conjunction with microwave NDT is employed for inspection under insulation.

RFID is a wireless non-contact method by using radio frequency signals for communication and sensing applications. The advantage of RFID over traditional electromagnetic NDT methods such as EC is illustrated in the Figure 1.2. The insulation problem, where d is the thickness of the insulation, is overcome by placing the sensing element tag directly upon the target surface in the high frequency RFID-based sensing method. HF RFID is adopted in this study due to its low-legal restrictions. HF RFID has a better performance in metal environment than that of LF RFID. Lager communication range can be realized as a result of more power can be transmitted by HF RFID. Compared to UHF RFID, the operational frequency of HF is standard and multi-tags can be chosen due to the existence of ISO 14443 and 15963 standards. The other advantages of RFID are its cost-effectiveness and the off-the-shelf availability of hardware. The limitation of RFID-based sensing is that the reading distance between the tag and reader is significantly reduced in the metal environment [14]. Furthermore, the sensing area of RFID-based sensing depends on the coil size of the tag.

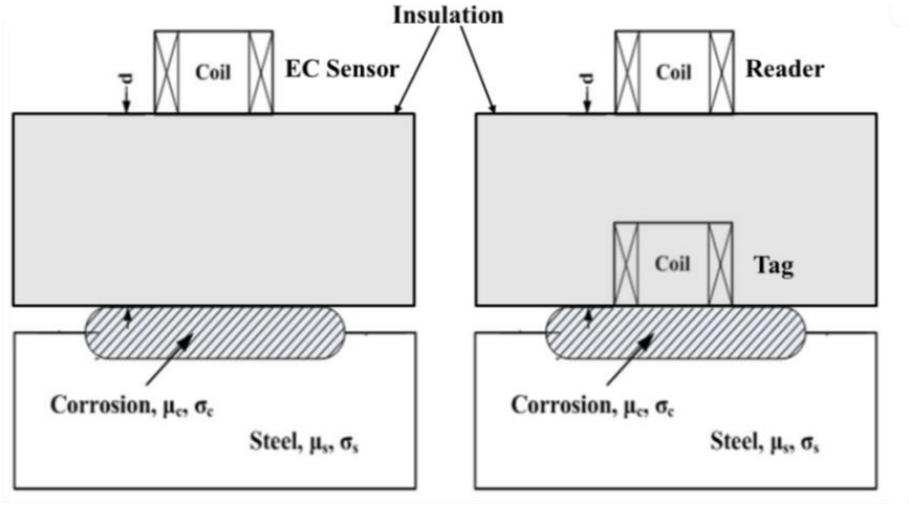

Figure 1.2 Illustration of the difference between the traditional EC method and the proposed RFID-based method.

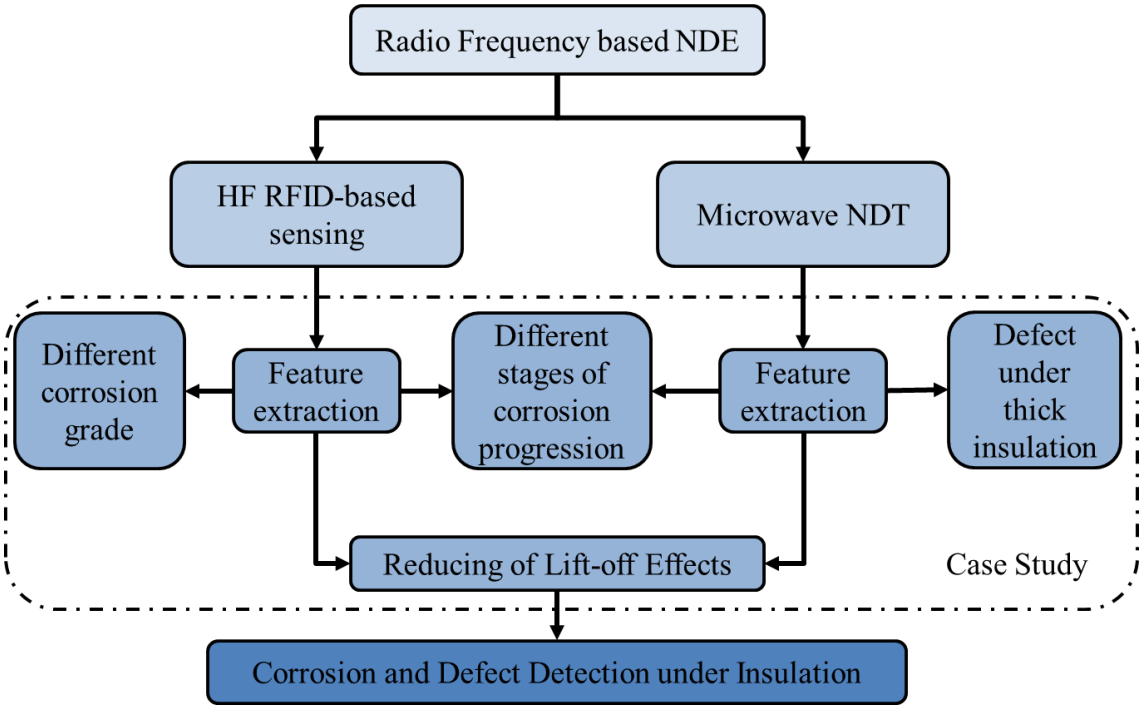

Figure 1.3 Research diagram for proposed RFID-based and microwave-based methods.

Due to the limitations of RFID-based sensing, it is only appropriable for the monitoring of small areas with limited thickness. To inspect corrosion and defects under thick insulation, a microwave NDT system is proposed. Microwave NDT is very suitable for examining structures with thick insulation due to the fact that while dielectric insulation materials exhibit low absorption levels of microwaves, the microwave radiation still

interacts strongly with corrosion and defects. In certain circumstances, such as high temperature applications, microwave NDT techniques can be a unique solution.

To address the challenges posed by insulated structures, a research diagram for an RFID and microwave system is shown in Figure 1.3. This includes the development of radio frequency-based NDE with theoretical concerns and experimental case studies, different levels of investigation and characterisation using proposed systems in line with the challenges. The research work also identifies their strengths and limitation of different proposed methods.

1.2 Aim and Objectives

The overall aim of this project is design and development a new generation of non-destructive evaluation and structural health monitoring systems.

The objectives of this research can be summarized as follows:

1) To undertake a literature survey and investigation of the applications of optical, eddy current, magnetic flux leakage and thermal systems developed for corrosion and defect detection, and to identify the challenges for NDT&E for characterisation under insulation.

2) To overcome challenges introduced by insulation and to design and develop a radio frequency-based sensing system for detection and characterisation under insulation, which includes the elements listed below:

    a. To design a high frequency RFID for steel corrosion sensing and characterisation under insulation; to demonstrate its capability for corrosion monitoring through case studies, and to verify the experimental results with standard methods.

b. To develop a microwave NDT for imaging and characterisation under thick insulation; to implement a linear sweep frequency for defects imaging classification in order to improve the resolution of the microwave imaging through case studies conducted in conjunction with specific industrial companies.

c. To reduce the effect of lift-off by applying algorithms for feature extraction under insulation using RFID-based sensing systems.

d. To compare processing algorithms and identify the most suitable processing method according to the different levels of complexity of insulation layers.

e. To identify the most suitable processing algorithms to use in different conditions with microwave NDT-based imaging. To reduce the effects of lift-off and non-homogeneity, for example.

1.3 Main Achievements

The main achievements of this research are:

1. The design of a high frequency RFID-based system for monitoring corrosion in steel, analysing response signals and extracting features, and the determination of successful approaches for corrosion characterisation via experimental case studies.
2. The reduction of lift-off effects introduced by the insulation layer through the application of PCA in conjunction with impedance, along with the extraction of features for corrosion characterisation from lift-off effects, and implementation of maximum 25 mm height.

3. The development and implementation of a microwave NDT system for imaging under thick insulation. This involves the investigation of microwave NDT measurement data with NMF, and reducing lift-off effects with NMF along with the extraction of features appropriable for detection. The most suitable evaluation algorithms are then identified depending on the scanning type and insulation texture complexity:
    a. For a line-scan, NMF is the most efficient for identifying surface defects at large lift-off.
    b. For a c-scan, PCA is most effective in identifying the most dominant feature correlating with defects information under thick insulation.
4. The implementation and validation of the reflection coefficient through experimental case studies. Defects are inspected under a maximum 40 mm of insulation, and non-homogeneous and large lift-off effects are reduced through the use of a linear sweep frequency in conjunction with PCA.

1.4 Thesis Layout

The overall layout of the thesis is as follows:

Chapter 1 gives a brief introduction, including the research background, aim and objectives, main achievements and an outline of the thesis.

Chapter 2 presents a literature survey of corrosion, specifically focusing on corrosion and defect detection under insulation. Meanwhile, the most common and widespread inspection methods and the suitability of primarily electromagnetic techniques for non-destructive testing and evaluation are analysed. The advantages and shortcomings of current methods are then discussed. The challenges in the detection of corrosion and defects under insulation are outlined, and finally the application of RFID-based and microwave-based sensing for condition monitoring is also reviewed.

Chapter 3 presents the theoretical background of HF passive RFID, followed by a describing operation of the transponder as a corrosion-sensing element. To overcome the limitations of HF RFID-based sensing, such as in monitoring size and lift-off, microwave NDT has been proposed for imaging under thick insulation. The theoretical background of microwave NDT is then presented. Techniques of statistical analysis for feature extraction with NMF and PCA are also presented in this chapter.

Chapter 4 starts with an initial feasibility study for different corrosion grades using the proposed HF RFID-based sensing system. Subsequent experiments investigate the detection of progression of corrosion over different exposure times. The thickness, conductivity and permeability of corrosion layer have been used to denote the corrosion stages, and compared with measurement result using proposed methods.

Chapter 5 establishes the experimental case studies for reducing lift-off effects. A custom feature is extracted by PCA. An independent lift-off feature for monitoring corrosion stages is experimentally demonstrated. The reduction of lift-off effects using microwave NDT in conjunction with NMF is also demonstrated. The improvement in defect detection with the proposed microwave NDT is detailed.

Chapter 6 provides an introduction to the case study of evaluating under thick insulation layer using the proposed microwave NDT system. The extraction feature to mitigate the effects of thick insulation layers is discussed. Feature extraction is proposed involving PCA in conjunction with a linear sweep frequency. PCA is used here to reduce the dimensionality of the original data via linear transformation. The experimental results are compared with the proposed solution. The improvement in the resolution of the microwave imaging achieved by the proposed method is presented and discussed in this chapter.

Chapter 7 summarises the research work so far, derives conclusions from the findings and outlines further work based on the current investigation.

1.5 Chapter Summary

This chapter introduces the research work which has been conducted on radio frequency based evaluation of corrosion and defects under insulation as part of a collaborative project with International Paint Ltd. The research background is elaborated, and the aim and objectives of the research are presented. Following this, the major contributions of the research are listed. Finally, the layout of this thesis is outlined and the contents of each chapter are summarised.

Chapter 2. Literature Survey

Having given a motivation to this study in the previous chapter, this chapter begins with a discussion of the causes, problems and challenges associated with defects and corrosion under insulation. Secondly, reviews are given of the most common NDT&E and SHM methods used for the detection and monitoring of defects and corrosion, including brief introductions to these systems and their strengths and weaknesses, before the state-of-the-art of NDT&E and SHM methods for corrosion detection is subsequently discussed in terms of acoustic, optical, electromagnetic, radioactive, thermal and electrochemical aspects. Thirdly, passive RFID and microwave NDT are discussed. In the end, the identified problems are summarised, detailing the need for a new, cost-effective passive RFID method in conjunction with an outline of microwave NDT for the monitoring of defects and corrosion under insulation.

2.1 Corrosion and Defects under Insulation

For many applications, the preferred metal is still mild steel with its virtues of relatively low cost, mechanical strength and ease of fabrication. The fact that it corrodes easily is the main drawback, which means that it rapidly loses strength which readily leads to structural failure. Therefore, steel pipes or other metal structures such as vessels are typically insulated to control corrosion and maintain structural health [7]. The purpose of insulation is to prevent corrosion from occurring by inserting a barrier between the environment and the metal surface. Although insulation provides a high level of protection against corrosion, the metal is still prone to corrosion under the insulation. This form of corrosion occurs on steel fitted with thick insulation, and it is very difficult to detect due to the corrosion being concealed by the insulation layer. The development of undetected corrosion can lead to serious failure. Serious consequences include the risk to the safety of persons, damage to the environment and economic impacts.

Corrosion under insulation is a major problem faced by many industries, primarily the oil and gas industry. However, it not only affects the petrochemicals industry, but also chemical, power and manufacturing industries. It can occur wherever insulated metals are fitted with insulation, and is a major cause of failure which is not an isolated problem limited to a particular geographical location. It occurs in facilities and on metal components all over the world. Therefore, billions of pounds are allocated in budgets for maintenance, inspection and the control of CUI.

In order to improve the reliability of insulated metal, NDT&E approaches are used to investigate the structural health condition and existence of corrosion. From the literature it is clear that further study is required to give information about the causes of CUI, how it occurs and where defect is most likely to occur. In this research, the further study of CUI can be categorised into three types of corrosion as discussed next [15].

2.1.1 Types of Corrosion

Unfortunately, metals are susceptible to corrosion. The occurrence of reactions among the metal surface, oxygen and water will result in the loss of electrons and the transformation of metal atoms into metal ions. Examples of the mechanisms of corrosion are [1]:

at the anode: $\mathrm{Fe} \longrightarrow \mathrm{Fe}^{2+} + 2e^{-}$

at the cathode: $\mathrm{O}_2 + 2\mathrm{H}_2\mathrm{O} + 4\,\mathrm{e}^{-} \longrightarrow 4\mathrm{OH}^{-}$

Corrosion is formed by the interaction of positively charged Fe^{2+} ions with negatively charged OH^{-} ions, as in $\mathrm{Fe}^{2+} + 2\mathrm{OH}^{-} \longrightarrow \mathrm{Fe(OH)}_2$. The hydroxide is insoluble and separates from the electrolyte. A more familiar name for $\mathrm{Fe(OH)}_2$ is rust, a white-green precipitate.

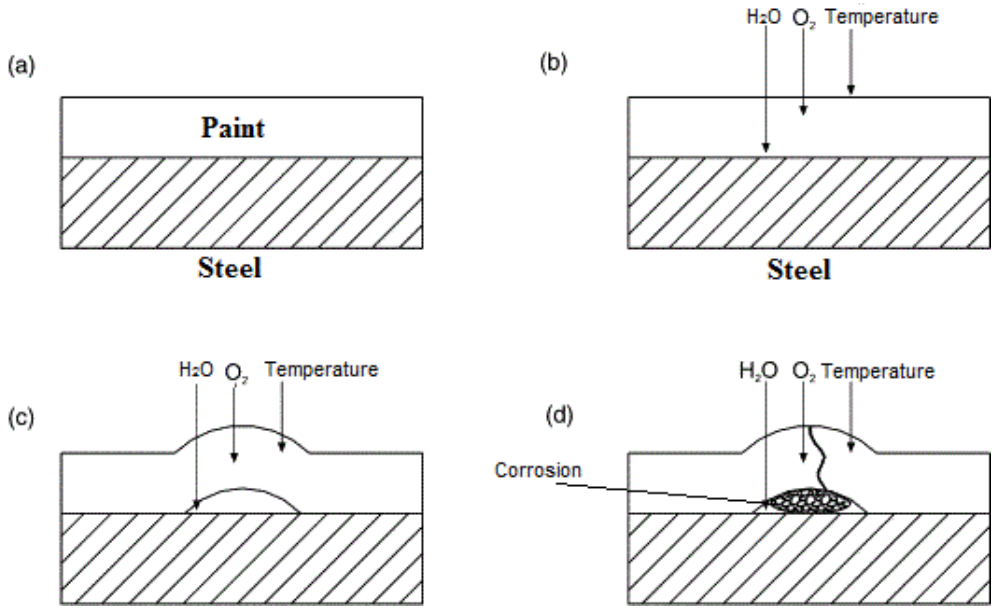

Figure 2.1 The mechanism of corrosion formation.

With further access to oxygen, $Fe(OH)_2$ oxidizes to ferric hydroxide $Fe(OH)_3$, which in turn converts to Fe_2O_3 (reddish-brown rust) and H_2O:

$$4Fe(OH)_2 + O_2 \longrightarrow 2Fe_2O_3 + H_2O \text{ (rust).}$$

Different types of corrosion, such as Fe_3O_4 (black magnetite), $\gamma - Fe_3O_4$ (brown rust) γ(FeOOH) (yellow rust), are observed depending on the nature of the interaction in the environment, and the general mechanism of corrosion formation is shown in Figure 2.1. Metal can be affected by corrosion in many different ways, depending on the nature of corrosion and the prevalence of specific environmental conditions. There are various forms of corrosion, and three major types have been identified as broad categories for CUI, which are presented in the following:

1. Uniform corrosion

   This is characterized by the entirety of the surface area considered corroding at the same (or a similar) rate [16]. Uniform corrosion (or general corrosion) is relatively easily measured and predicted. This type of corrosion causes the loss of metal thickness and weight.

2. Localized corrosion

   As opposed to general corrosion, localized corrosion occurs at specific areas of metal, whilst the rest is non-corroding or corroding at a much lower rate [17, 18]. Localized corrosion can be classified as one of the following three types:

   a. Pitting

      This kind of corrosion develops rapidly in discrete regions of a material, although the vast majority of the surface remains almost unaffected [19, 20]. The main characteristic of this corrosion is that it is extremely localized and penetrates deeply into the relevant region. It is one of the most dangerous forms of corrosion.

   b. Crevice corrosion

      Crevice corrosion occurs at a specific location, and is similar to pitting. This kind of corrosion is often associated with a stagnant micro-environment [21, 22]. Crevice corrosion occurs under acidic conditions or when oxygen is consumed in a crack.

   c. Stress corrosion

      This type of corrosion occurs with stresses applied to insulated surfaces. This process involves the conjoint corrosion and straining of a metal which begins with small cracks in the metal and then spreads, resulting in structural weakness [23].

3. Galvanic corrosion

   This kind of corrosion generally results from the presence of wet insulation with an electrolyte or salt, so that current flows between dissimilar metals [24].

Appropriate NDT&E methods can be applied to detect corrosion with an understanding of the types of corrosion occurring under insulation. The detection of corrosion under insulation is more than simple corrosion detection, since it concerns corrosion

underlying the insulation. In the following section, the challenges of corrosion and defect detection under insulation are outlined.

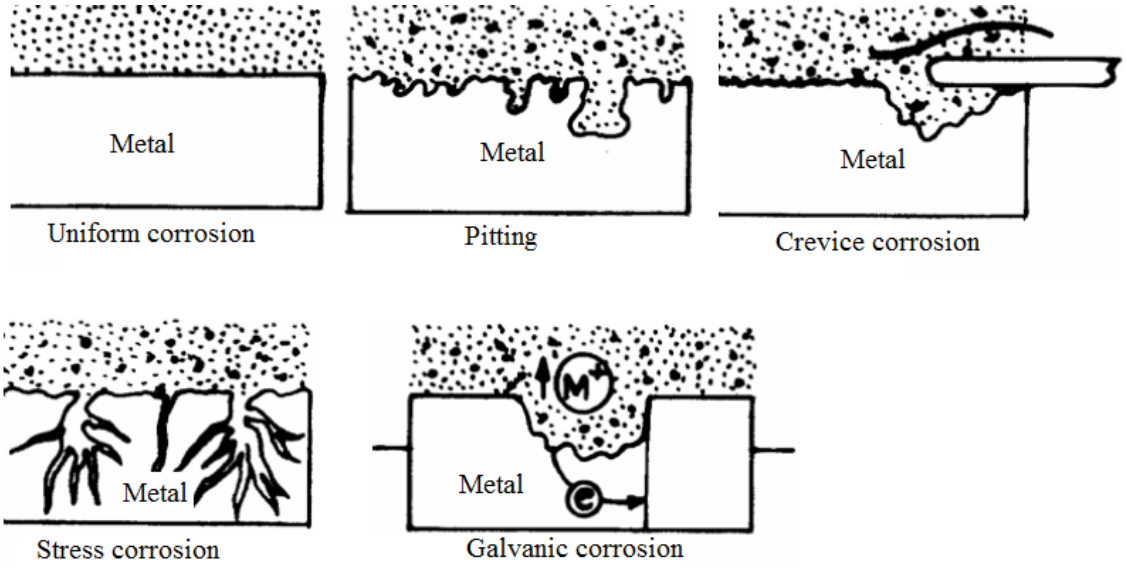

Figure 2.2 Diagrammatic summaries of the various types of corrosion [12].

2.1.2 Challenges Posed by Corrosion and Defects under Insulation

Currently the most effective method of inspecting under insulation requires the removal of insulation [25]. This is an expensive process which may require the shutting down of operations. Instead of removing entire sections of insulation, small inspection holes are often cut to gain access to the metal surface. Once there is access to the insulated metal surface, various techniques such as electrochemical impedance spectroscopy [26, 27] can be used to determine the condition of the metal and determine the level/severity of any corrosion.

Challenges of NDT&E for detection under insulation are diverse. Along with the usual challenges of accurately detecting and quantifying corrosion, the task is made more difficult due to the large distance between the sensor and the metal surface introduced by the inaccessible insulation layer. This distance is known as the lift-off. The immediate effect of a large lift-off is the reduction in sensitivity to small changes accompanying corrosion, such as variation in thickness or loss of mass. Meanwhile, the

thickness of the insulations may be different, resulting in variations in lift-off leading to lift-off effects. This lift-off effect will cause errors in detection.

In addition, the challenges associated with the characterization of metal corrosion require an understanding of the micro-structural and physical changes occurring prior to corrosion initiation and growth. In most cases of corrosion, changes in the intrinsic material properties are dominant in the early stages. Physical damages such as defects will be observable when the accumulation of these changes exceeds a critical limit. Therefore, there is no universal method for the detection of corrosion under insulation because the behaviour of corrosion is affected by the mix of these diverse factors.

For example, corrosion under insulation in pipelines includes both internal and external corrosion. Apart from exceptional cases involving corrosive fluid components, internal corrosion is usually a much more gradual process resulting in a lowering of pipeline efficiency. Pipeline inspection gauges (PIGs) have been used to probe the insides of vast pipelines. PIGs were originally developed to solve removal of deposits problems because the flow through a pipeline can be obstructed by these deposits. Regular line cleaning and inspection with intelligent PIGs can be utilized to take care of the pipe internally in most installations [28]. As a result of further advances in technology, PIGs have become more intelligent. With a technique known as magnetic flux leakage, PIGs can be used to detect internal leaks, corrosion, or flaws [29-32]. In general, external corrosion is more serious in that it can drastically reduce the life of the pipeline and impair its safety. Therefore, it is important to develop an advanced corrosion sensing system for external monitoring.

Based on the study of corrosion under insulation and its challenges, reviews of the use of NDT&E and SHM for corrosion detection are provided in the next section. NDT&E includes use of a wide variety of techniques to test and evaluate the integrity of a

material, component or system without causing any damage [33]. SHM is continuously monitoring the structural condition with embedded sensor systems to maintain structural integrity [10, 34]. It refers to recognition and characterisation of defects in structure. SHM can be used to help owners, builders and designers of structures in making rational decisions.

NDT&E is a well-established manual testing and evaluation technique which focuses on the detection and characterisation of damages in materials. It has been extended to metal under insulation. For example, acoustic emission has been used to locate pitting in steel plates [35], ultrasonic [36] and radiography [37] have been adopted to acquire and analyse images to detect corrosion, and fibre optics have been employed for the corrosion monitoring of steel in reinforced concrete [38]. SHM can provide real-time data concerning the health and operational conditions of components or systems. Compared with NDT&E, SHM emphasises the real-time and continuous monitoring of corrosion. Therefore, smart materials and sensors are used in life cycle monitoring [39], such as Fibre Bragg Grating (FBG) sensors for bridge monitoring [40].

To detect corrosion and defects on the metal surface under insulation, NDT&E and SHM are both powerful tools. In the next section, the state-of-the-art of NDT&E and SHM techniques for detecting corrosion and defects in metal are reviewed. The advantages and disadvantages of each method are summarised, followed by the challenges for the evaluation and monitoring of metal underlying insulation.

2.2 State-of-the-art NDE and SHM Techniques

Non-destructive evaluation is defined by the American Society [41]. The physical condition of material is determined by non-destructive testing techniques to indicate the presence of defects. To this end, non-destructive testing can be considered equivalent to non-destructive evaluation.

Several NDT&E techniques have been applied for corrosion and defect detection, and each has certain advantages and disadvantages. For example, eddy current-based techniques have been used for corrosion inspection, where a relatively small probe is employed and no physical contact with the specimen is needed [42]. However, these methods can only be used to detect defects on the surface or near-surface. Furthermore, they are sensitive not only to variations in conductivity and magnetic permeability of the specimen, but also to lift-off variations [43, 44].

Specific methods used for detecting corrosion and defects are reviewed in the following sections. These can be categorised as optical, acoustic, electromagnetic, radioactive, thermal and electrochemical methods, as shown in Figure 2.3.

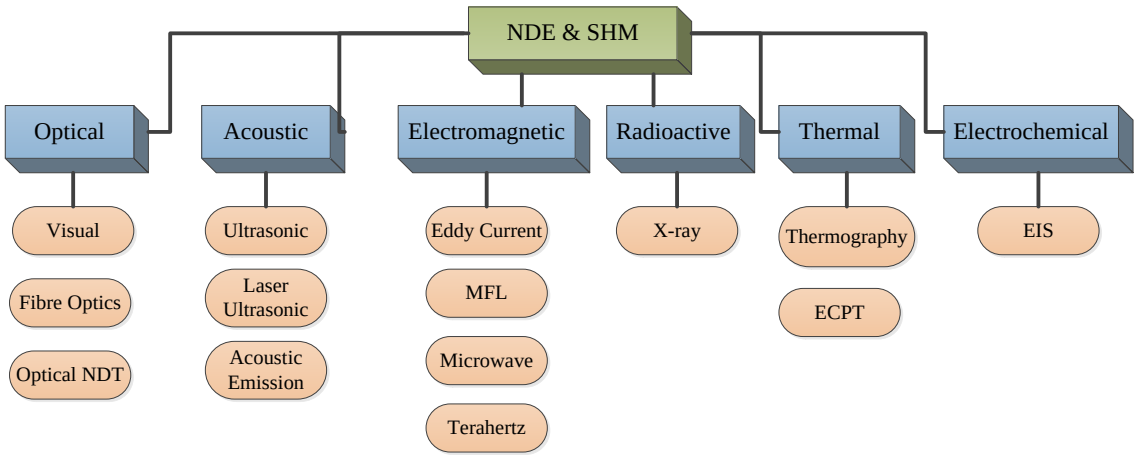

Figure 2.3 Categories of NDT&E techniques.

2.2.1 Optical Methods

2.2.1.1 Visual inspection (VI)

Visual inspection is one of the most common NDT methods. In many situations, a well-trained operator holding simple tools (such as flashlights) can perform a very effective inspection. For enclosed systems, the application of the visual inspection method can be challenging and possibly ineffective. A borescope (as shown in Figure 2.4) is basically a fibre optic cable with a miniaturized camera placed on the end, which enables the

operator to inspect difficult-to-see areas. The extension of visual inspection is the biggest advantage of this method. Therefore, the status of an inner surface can be observed because the direction of inspection can be arbitrarily changed [45]. These visual examinations can be used for detecting corrosion and other physical defects.

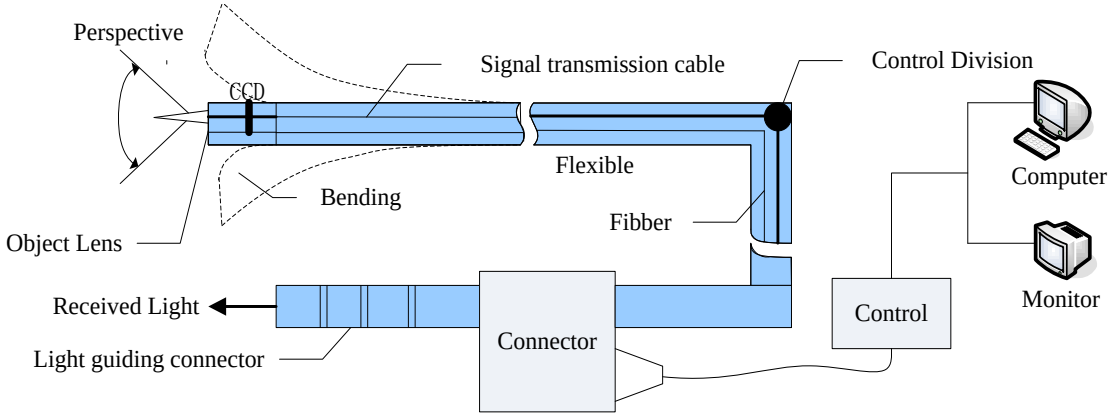

Figure 2.4 The structure of the electronic endoscope.

2.2.1.2 Fibre optics

Optical fibre can be used in extreme environments. Electromagnetic interference and corrosion resist optic transmission. The use of the optical fibre has very little influence on the structure being monitored due to its small-size and light-weight. Therefore, it can be either embedded or attached to the structure under monitoring. The optical fibre can be adopted to measure many parameters which include electric field, pressure, chemistry, liquid level, strain of vibration, temperature and corrosion. There are numerous kinds of fibre optic which including Bragg, intrinsic Fabry Perot interferometer (IFPI) and extrinsic Fabry Perot interferometer (EFPI).

These fibre sensors are usually embedded in concrete structures. The properties of optical signals, including polarization, phase, wavelength and light intensity, are analysed to determine variations in the structure's properties, such as structural strain, temperature, corrosion and overload. Therefore, several studies have used optical fibres

for condition monitoring and NDT&E purposes [46-48]. Samer *et al.*[49] reported long period grating-based technique for measuring refractive index changes in ion concentration of the surrounding environment to monitor the corrosion of reinforcement in concrete. Zhao *et al.* [50] employed Fibre Bragg Gratings to directly monitor the corrosion at the steel-concrete interface based on the white light interferometer sensing technique. Colum *et al.*[51] employed birefringent photonic crystal fibres based sensors to measure temperature changes to monitor corrosion rate along the length of reinforcing steel in situ and thus evaluate the service lift of the structures.

2.2.1.3 Optical NDT

There are a variety of optical NDT methods available. In terms of corrosion detection, these methods are generally used to measure deformations on surfaces. These deformations are caused by either pitting on the exposed surface or sub-surface corrosion and defects in the structure. Laser speckle interferometry is an efficient non-destructive optical technology with the advantages of being contactless, and with no limitations in terms of geometry and size of the specimen. It also provides high detection rates and sensitivity, and has been widely used in automotive, marine, aerospace and manufacturing high-performance materials. A number of relevant investigations have been based on laser speckle interferometry and holography [52].

As shown in Figure 2.5, a laser shearography employs the Michaelson interferometer. Two speckles in the image plane are caused by tilting the shear reflecting mirror, and then they will use to shear each other. Sheared speckles are then superimposed to form speckle interference patterns which are recorded by a CCD camera. Any deformation of the object under test will lead to changes in speckle patterns. The CCD camera is used to digitize speckle patterns of the deformation, which are then processed by computer to form laser shearography image in the monitor.

Furthermore, optical surface topography systems have also been used for the characterization of corrosion and defects [53, 54]. Direct optical metrology methods such as laser interferometry have been used to measure the dissolution of the micro-surface, such as mass loss, caused by pitting and crevice corrosion on a stainless steel alloy under seawater [55].

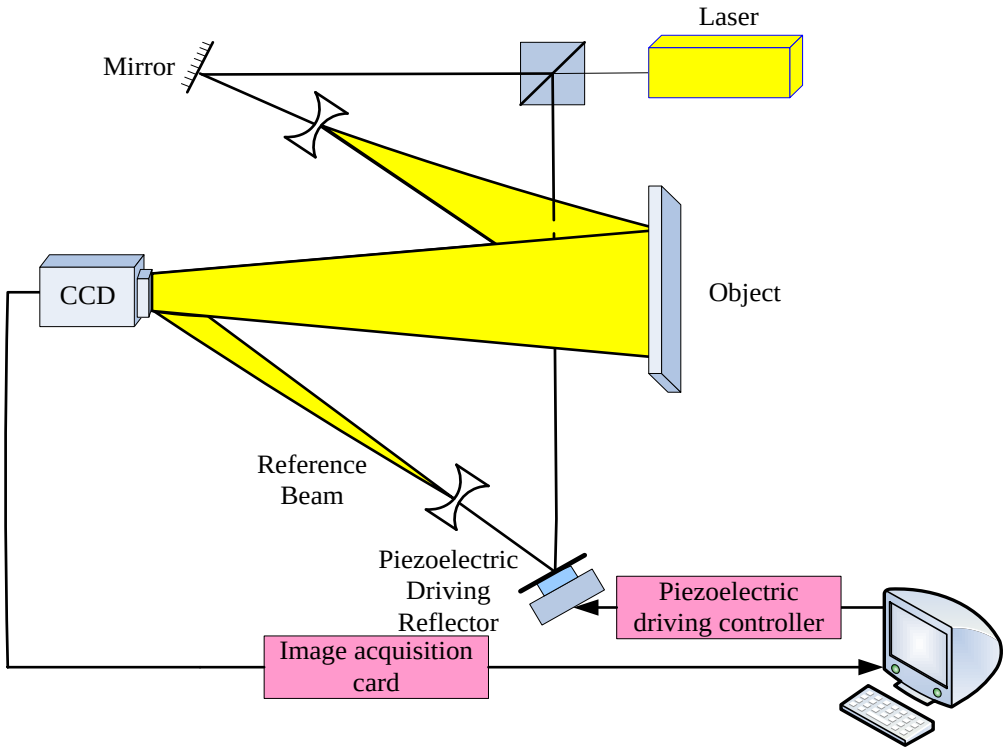

Figure 2.5 A laser speckle NDT system [52].

2.2.2 Acoustic Methods

2.2.2.1 Ultrasonic testing (UT)

Ultrasonic testing is based on generating and detecting mechanical waves or vibrations within samples under test. These samples are not limited to solids. A majority of ultrasonic techniques adopt 1 MHz to 100 MHz as operating frequencies. The term ultrasonic refers to those sound frequencies beyond human hearing restrictions. The traveling speed of ultrasonic waves in a material is dependent on the material's density and elastic modulus. Therefore, ultrasonic methods are very suitable for the

characterizing properties of materials. Furthermore, changes in material properties will strongly reflect ultrasonic waves at the boundaries, as shown in Figure 2.6. Thus, ultrasonic methods are often used for the measurement of thickness [56] and corrosion monitoring [57].

Although UT has the capability to detect corrosion, these methods suffer from a difficulty in distinguishing between reflections from surface/near-surface corrosion and reflections from multiple material surfaces. Another disadvantage is that they require coupling media such as water or gel to acoustically couple pulses from the transducer to the material. This makes traditional UT unsuitable for certain situations due to the requirements for surface preparation.

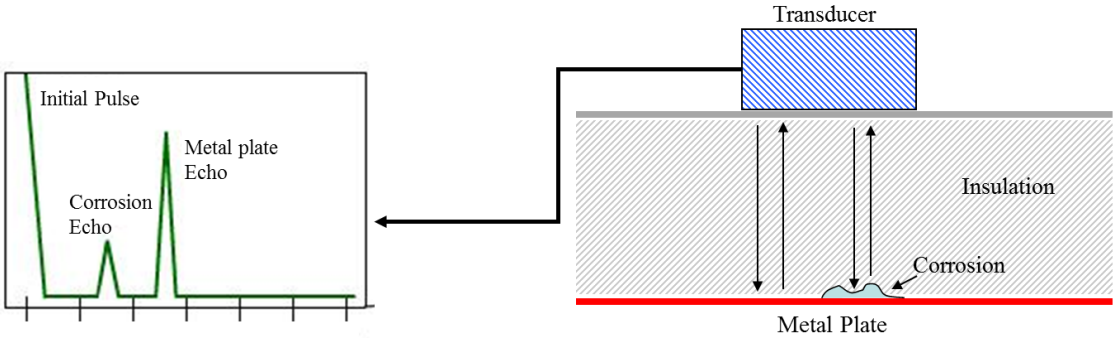

Figure 2.6 Ultrasonic testing.

Much work has been done in recent years to develop non-contact ultrasonic techniques for defects characterisation without requiring surface preparation. Air-coupled techniques include adaptations of traditional piezoelectric transducers [58], which are more suitable for most inspection conditions. However, an appropriate angle for the introduction of the ultrasound into samples to be inspected is a strict requirement. Electromagnetic acoustic transducers (EMATs) have also been developed [59], in which electromagnetic non-contact transducers are used to generate and receive acoustic signals, although this does mean that EMATs are limited to electrically conductive materials [60].

Nowadays, developments in the field of ultrasonic techniques have led to phased array ultrasonic in instruments which can be portable [61]. The precise tailoring of ultrasonic waves is introduced into the sample by using the phased firing of ultrasonic arrays in one transducer. Naoyuki *et al.*[62] used a phased array ultrasonic probe for the detection and sizing of stress corrosion cracks in austenitic stainless steel welds. This method employs a single phased array probe with focal laws for two kinds of sectorial scans (S-scans) separately based on transverse and longitudinal wave velocities. The transverse wave S-scan with an angle beam transverse wave method is used for the detection of stress corrosion cracks. The longitudinal wave S-scan uses a multiple beam method to determine the size of stress corrosion cracks.

2.2.2.2 Laser ultrasonic

Given recent advances in laser ultrasonic techniques, lasers can be used to generate and detect ultrasonic waves [63]. This non-contact technique has been used for the measurement of material thickness, flaw detection and materials characterization. A laser ultrasonic system is composed of a laser ultrasonic generator and an interferometric sensor.

Francisco *et al.* [64] employed laser ultrasonic for the detection and locating of SCC (stress corrosion cracking) in stainless steel pipes. A laser is adopted to generate ultrasonic waves which will interact with cracks, and then changes in generated wave-modes are examined using time-frequency analysis techniques. The geometric images of these defects can be provided by scanning the samples for defects identification. The limitation of this technique is that access to the surface of the sample under test is required. Furthermore, this technique is sensitive to surface-breaking defects, and thus its scope is limited.

2.2.2.3 Acoustic emission (AE)

AE is defined as strain energy suddenly released within or on the surface of a material, which generates a transient elastic wave. Therefore, the dynamic process associated with the degradation of a structure can be detected by AE. When an external stimulus, such as a change in pressure, load, or temperature, is applied to a structure, an energy released causes localized sources to form stress waves, and these waves then propagate to the surface, where sensors are used to record them (as shown in Figure 2.7).

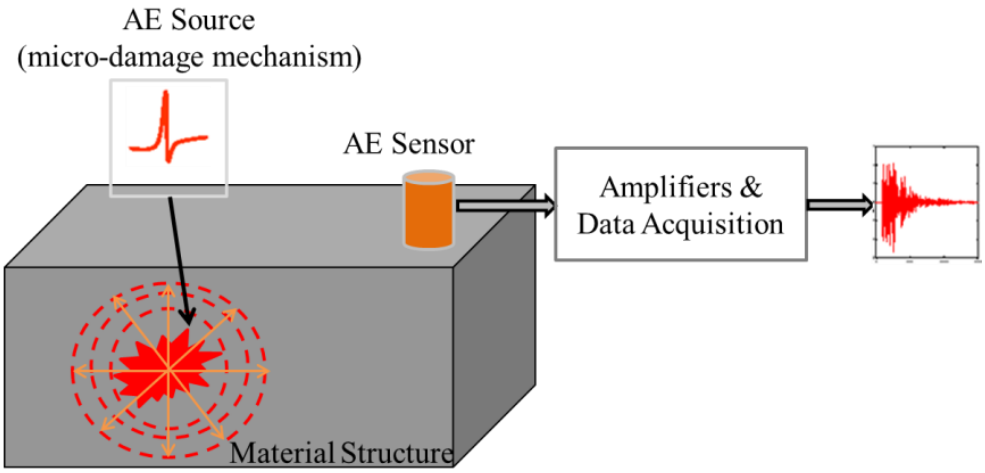

Figure 2.7 Basic principle of acoustic emission testing.

In the majority of studies, AE techniques have been used to detect pitting corrosion. Fregonese *et al.* [65] used an AE technique to monitor progression of pitting corrosion in austenitic stainless steels. Mazille *et al.* [66] confirmed that AE can be applied in fundamental research on pitting corrosion because it offers many potential advantages over other techniques. Cakir *et al.* [67] evaluated hydrogen in the growing pitting.

Unfortunately, AE systems can only be used for qualitative testing. Additional NDT methods are required to obtain quantitative results in regard to the size and depth of defects. Furthermore, environment noise affects the AE signals receiving. Therefore, the use of signal discrimination and noise reduction techniques is essential during real-world applications.

2.2.3 Electromagnetic Methods

2.2.3.1 Eddy current (EC)

Eddy current technique is one of the most effective methods for the detection and characterisation of surface defects and corrosion in conductive samples. This technique is based on holding a conducting coil with alternating currents close to the sample. A primary magnetic field is established in an axial direction around the coil. This electrical current then creates its own secondary magnetic field, which is opposite in direction at all times and opposes the coil's magnetic field in accordance with Lenz's Law, as illustrated in Figure 2.8. The interaction between the magnetic field generated by the coil and the magnetic field generated by eddy currents are then examined with sensors or coils.

EC methods can be very effective and have been adopted to detect the presence of corrosion on the surface of metal samples. Thus, EC methods are the most common NDT method for aircraft measurement, and have become extremely portable and relatively inexpensive. Lepine *et al.* [68] employed an eddy current scanning method for corrosion detection in thick skin aircraft structures with a calibration specimen. However, conventional EC techniques have difficulties detecting and quantifying small metal loss due to corrosion in multilayer structures. This is because the ability of EC techniques to detect subsurface defects is largely determined by the skin effect phenomenon. Most of the current flow occurs on the surface of a conductor due to the skin effect, exponentially decaying with increasing depth. This penetration depth conforms to:

$$\delta \approx \frac{1}{\sqrt{\pi f \mu \sigma}} \tag{2.1}$$

where δ is the penetration depth (mm), f is operational frequency (Hz), μ is permeability of sample under test (H/mm), and σ is conductivity of sample under test (S/mm).

The development of EC technology has led to the introduction of the pulsed eddy current (PEC). This is a natural evolution of EC method and has been developed to improve penetration depth. With conventional EC methods, a fixed frequency sinusoidal current is used to generate eddy currents on the surface of a conductor. However in PEC the shape of the excitation current is a square pulse or step function. Looking at the Fourier transform of a step function, it is clear that it contains a continuum of frequency components compared to just one for sinusoidal EC. Because penetration depth is dependent on operating frequency, the PEC response signal will contain information from multiple depths, which is thus equivalent to multiple-frequency EC. The detection capabilities of PEC has been demonstrated in corrosion characterisation [42], flaw detection [69] and stress measurement [70]. PEC can be automated and it has the advantages of greater penetration, the ability to locate corrosion, and only moderate cost.

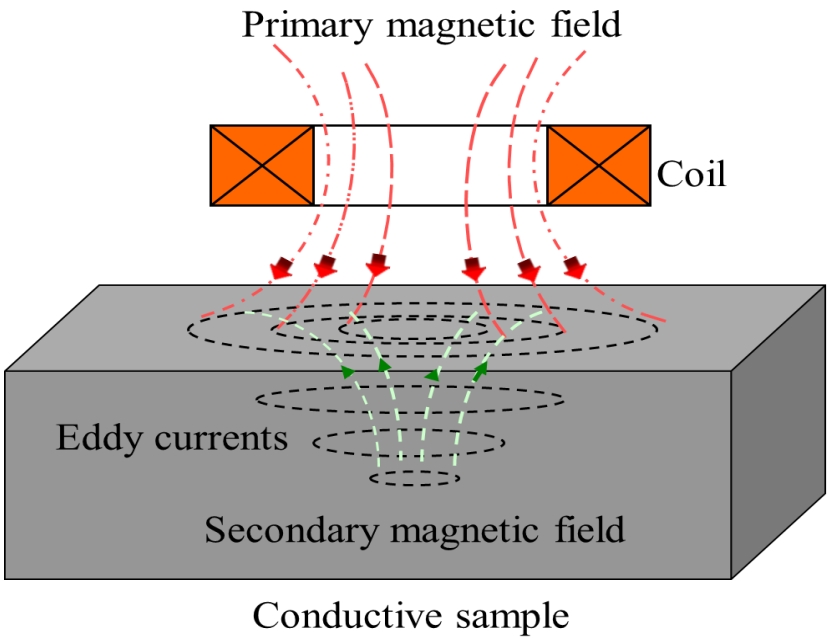

Figure 2.8 Eddy current interactions with a conductive sample.

Safizadeh *et al.* [71] have presented the results of a method based on a multi-frequency eddy current along with signal processing to characterize material loss in a two-layer lap joint structure. The thicknesses of the individual layers of the lap joint have been mapped with this technique. Applying this method to aircraft lap joints shows that corrosion can be quantified with an error of less than 4% for one layer thickness. Furthermore, recent developments in eddy current technology have led to multichannel portable instruments which allow the faster inspection of larger areas. Meanwhile, new magnetic sensors have been developed to replace coils [72], such as giant magneto resistive (GMR) sensors. However, EC based methods are limited to electrically conducting materials. Furthermore, these methods are very sensitive to lift-off effects, and the surface of the material must be accessible.

2.2.3.2 Magnetic flux leakage (MFL)

MFL is a derivative of magnetic particle inspection (MPI). It is based on measuring the leakage of magnetic flux caused by the presence of defects and corrosion. In practice, magnetisation is provided by a permanent magnet or an electromagnet by DC, AC or pulsed excitation. The difference between MPI and MFL is that the latter measures flux leakage using magnetic field sensors such as Hall devices or magneto resistive sensors, as shown in Figure 2.9. Thus, the data acquired can be processed using computer-based analysis, signal processing and quantitative assessment. However, MFL is only appropriate for the characterisation of corrosion and defects in ferromagnetic-material.

MFL techniques are popular in the inspection of pipelines. Muhammad *et al.* [73] employed an adaptive filter and a wavelet based de-noising technique for seamless pipeline inspection. Larsen *et al.* [74] used a high-resolution MFL to generate magnetic fields to determine any corrosion and defects in pipelines. With advanced sensor technology, leakage and mass loss can also be detected with MFL. The precise location

of corrosion can also be provided. Wang *et al.* [75] adopted MFL with a pulsed exciting signal to examine the traditional magnetic path for corrosion detection in metal pipelines. Both penetrating depth and detecting sensitivity have been improved due to the abundant components of the pulsed exciting signal.

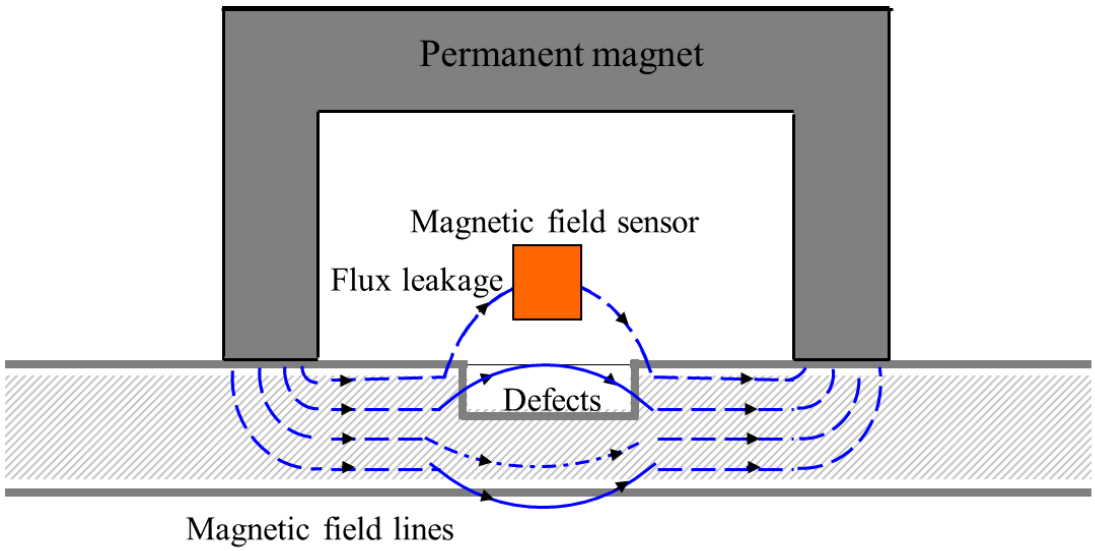

Figure 2.9 Magnetic flux leakage (MFL) inspection.

Corrosion in insulated pipelines can lead to catastrophic failure. MFL-based PIGs have been successfully applied to many pipelines for corrosion and defects inspection. However, there is a subset of pipelines not suitable for MFL-based PIGs. Most of these are limited by the bulky size of the MFL-based PIGs. Sufficiently bulky PIGs are needed to provide sufficient magnetic force. Therefore, MFL-based PIGs are too big to pass through some pipelines. A more suitable technology is required to inspect those pipelines which often referred to as 'Unpiggable' pipelines. These pipelines cannot be inspected due to internal restrictions and MFL-based PIGs cannot pass through them due to their large bulky magnets.

Most commonly, a pipeline with thick insulation would increase the difficulty of detection from outside using MFL, because the magnets can't move away from the magnetic sample's surface as is needed during inspection. Therefore, external corrosion

under insulation cannot be examined by PIGs. This type of corrosion is more serious in that it can drastically reduce the life of the pipeline and impair its safety. Hence, it is important to develop an advanced corrosion sensing system for external corrosion monitoring through insulation.

2.2.3.3 Terahertz (THz) technology

THz refers to electromagnetic waves with frequencies ranging from 0.1 THz to 10 THz. Wavelengths of THz radiation are between the microwave and infrared spectra which are approximately from 0.03 mm to 3 mm. A THz wave with known wavelength is used to illuminate a sample during inspection. This THz wave is examined at or near the radiation source after interaction with the sample under test. The inner structure of the sample is determined by analysing changes in the THz signal, because the dielectric characteristics of the sample or a discontinuity will affect the THz signal.

Since the mid-1980s, THz-based methods have made important advances. THz wave has a better penetration through most dry, non-metallic materials such as foams, ceramics, glass, resins, paint, rubber and composite materials [76, 77]. Therefore, these methods have been applied in the NDT&E fields, and can be divided into continuous THz and pulse THz methods. THz-based NDT has unique advantages in detecting inner defects in non-metallic materials compared to other NDT techniques. The THz wave can penetrate non-transparent materials and evaluate inner defects. Moreover, THz-based NDT has been used to inspect insulated materials. The ability of THz-based imaging for corrosion under insulation has been studied by the U.S. Army Research Laboratory and NASA. Corrosion under insulation leads nominally smooth surfaces to become rough and irregular, and erosion can be detected by THz-based imaging [78].

Figure 2.10 illustrates a typical THz system for detection of defects in SOFI (Spray on Foam Insulation) layers for space shuttle, and researches have shown that THz-based

NDT can provide an effective evaluation for shuttle fuel tank under insulation materials. THz-based imaging has been chosen by NASA which will be used for future launches inspection.

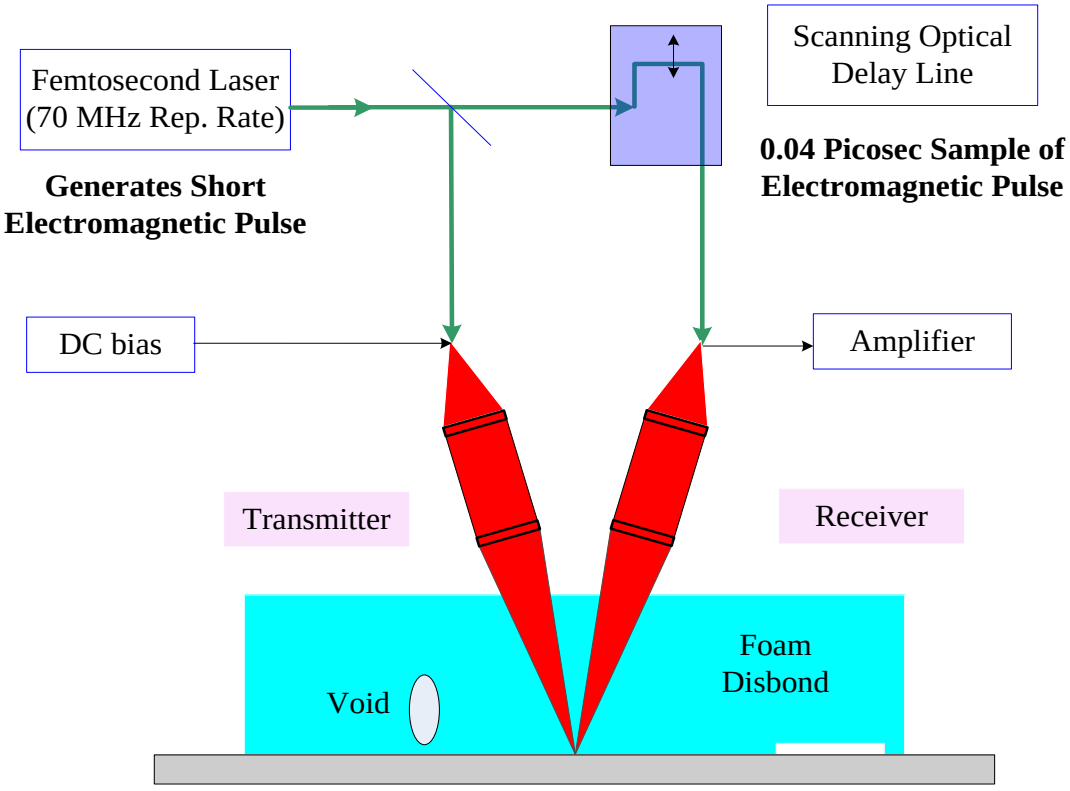

Figure 2.10 A reflected pulse THz system used for detection in SOFI.

Zimdars *et al.* demonstrated a THz-based system for a large area imaging, in which a high-speed time domain is employed for non-destructive evaluation of the bubble [79]. Moreover, many studies have been shown that signal processing methods can be adopted for THz-based NDT. Chiou *et al.* adopted a direct approach to extract defects information from responses, which overcomes the limitations of traditional indirect methods, where reflection signals from a metal base are used for further analysis [80].

Nair *et al.* employed a wavelet-based technique for enhancing image in SOFI THz-based imaging [81]. Redo-Sanchez *et al.* [82] employed THz spectroscopy to inspect large voids under a 101mm thick foam, good correlation has been demonstrated between measured results and visual inspection results. In order to obtain accurate

images, several signal processing methods have been compared, including the use of time-domain, fast Fourier transform and power spectral density. Aldrin *et al.* developed a quantitative assessment protocol for the SOFI evaluation [83]. However, the THz wave cannot penetrate metallic material, which limits the scope of its application. Furthermore, THz-based methods have disadvantages of high costs and strong water absorption.

2.2.4 Radiographic Methods

Radiography is one of the most common NDT&E methods, and is based on differences in the attenuation of penetrating radiation in materials depending on radiation energy, and material density and thickness. Different thicknesses and types of materials give different attenuation coefficients, and variations in transmitted radiation intensity are caused by defects and corrosion. Therefore, the value of radiographs for detecting defects, corrosion and welds in metals has been proven [84, 85].

There are several different radiographic techniques, including profile radiography, digital radiography, flash radiography and real-time radiography. These techniques are based on the use of either gamma rays or X-rays to image the profile of a structure or to provide information about the thickness of an inner structure. In many cases, discontinuities in insulated metals are readily detected. Radiography is still widely used in spite of its expense and the fact that ionising radiation poses health and safety risks. Recent developments in digital radiography have helped to eliminate the use of film, thus reducing costs. Apart from the above issues, however, there are several notable limitations on the use of radiography. For example, it is not suitable for the detection of surface defects and it is also not possible to extract quantitative information for the estimation of defects' depth.

2.2.5 Thermal Methods

2.2.5.1 Infrared thermography

Infrared (IR) thermography methods measure thermal variance for a characterized sample which undergoes a response to a stimulus. Improvements in IR cameras have led to more advanced forms of thermography. The advantages of thermography are that it is real-time, non-contact and a large area can be inspected in a short time. With an IR camera, a thermal image is produced by infrared light which is invisible to the human eye and which is emitted from objects due to their thermal condition.

Infrared thermography detection is based on differences in temperature conditions. There are two types of thermography: active and passive [86, 87]. Active thermography (AT) is defined as the application of a stimulus to heat up the target to allow a wide range of its characteristic to be determined. These obtained characteristics can be defects or corrosion. Passive thermography (PT) is defined as measuring temperature differences among target material, surrounding materials and ambient temperature conditions. Normally, active thermography-based methods are the most commonly used.

Sfarra *et al.* [88] employed an infrared thermography for the cellular structure detection in honeycomb structures. A sample with a 3-layer structure with a thickness is 18 mm was measured where the outer two layers were made of carbon fibre and the middle layer was made of aluminium. Holes with diameters of 4 mm at 6 mm depth and 6 mm at 10 mm depth were detected.

Maierhofer *et al.* [89] studied the use of infrared thermography for voids and cellular hollows testing. Eight different sizes of holes were created in a concrete sample. Different thermal infrared images were produced with different heating times, along with thermal conductivity curves for different densities of concretes. The capability of

infrared thermography to measure defects in concrete materials near the surface, at depth less than 100 mm, was proven. However, 1.5 hours of heating time was required to detect deeper defects, where only a few minutes of heating time were needed to detect defects of 20 mm in depth.

One drawback of the IR method is the high cost of quality thermal cameras, but recent developments have led them to become significantly less expensive.

2.2.5.2 Eddy current pulsed thermography (ECPT)

ECPT involves an application of a high frequency electromagnetic wave (typically 50 kHz – 500 kHz) at a high current around 256 A to 380 A to the material under inspection for a short period of typically 20 ms – 1 s [90, 91]. Induced eddy currents are forced to divert when they encounter a discontinuity, which leads to increases and decreases in the density of the eddy current in that area. Areas with increased density of the eddy current are exhibiting higher levels of Joule (Ohmic) heating, and thus defects can be obtained from sequenced thermograms during the heating and cooling periods.

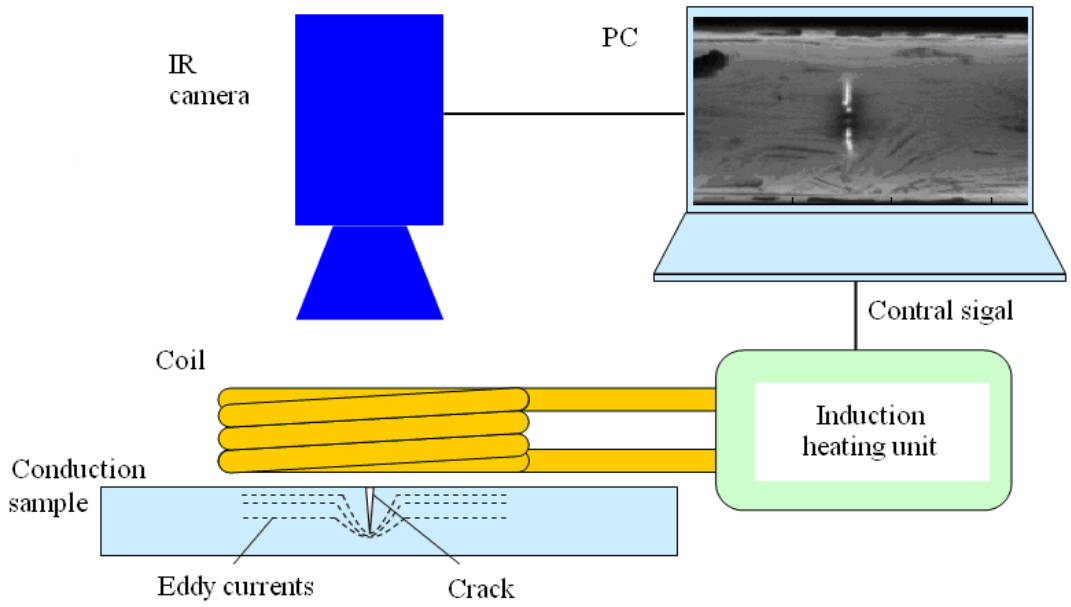

Figure 2.11 A basic configuration of ECPT system [92].

The configuration of an ECPT system is shown in Figure 2.11. It consists of an induction heating system which induces eddy currents in the sample under inspection and generates a heat; the generated heat is recorded by an IR camera to form digital data, then these digital data will be displayed on a monitor and stored in PC.

He *et al.* [93] reported an application of ECPT for the detection of corrosion blisters in mild steel under insulation. A wide range of defects can be considered based on interactions between the distribution of eddy current density and heat conduction. The corrosion blister areas were easily detected using sequenced thermograms from an IR camera during the experimental study. However, ECPT has the disadvantages of a limited ability to be used to inspect conductive material, and furthermore the heat inducing equipment is very bulky.

2.2.6 Electrochemical Methods

Electrochemical methods are those concerned with the interrelation of electrical and chemical effects. Electrochemical impedance spectroscopy (EIS) is one of common electrochemical methods which adopt an AC source to measure impedance as a function of frequency. Therefore, many materials, including insulation layers and corrosion inhibitors, can be evaluated using this non-destructive method. Detailed information about samples under test can be provided. This data can be also used to determine parameters such as corrosion rate, electrochemical mechanisms and reaction kinetics.

Moreover, many studies have been established based on EIS for a variety of applications. EIS has been adopted for corrosion rate testing [94] and protective coating properties investigation [95]. The application of electrochemical methods has multiple advantages. Firstly, real-time measurements of corrosion rates can be provided by electrochemical tests. Secondly, corrosion rate data over time can be provided too. Thirdly, they can be performed quickly.

Therefore, most of previous researches employing EIS are focused on corrosion behaviour and mechanisms investigations [96, 97]. However, electrochemical measurements require high levels of technical expertise to perform data analysis and comparatively expensive equipment [98]. They are also not suitable for in-situ corrosion detection or monitoring under thick insulation.

2.2.7 Summary Review of NDT&E and SHM

Five categories of NDT&E techniques (acoustic, optical, electromagnetic, radioactive and thermal) and one electrochemical method have been discussed. A comparison of these technologies is provided in Table 2.1, giving an overview of each method and identifying the advantages and limitations of current techniques.

Corrosion effects are a complex combination of multiple factors, including variations in conductivity, permeability, and permittivity and changes in thickness. The probability of corrosion detection is affected by these factors. There is no universally applicable method for corrosion detection, due to the complex combination of these different factors [21]. Therefore, none of the NDT&E techniques discussed above can address all the challenges of detecting corrosion and defects under insulation, since thick insulation layers induce a large lift-off between sensors and the inspected surface.

Selection of an NDT&E technique requires consideration of more than the detection capabilities. The application, portability of equipment, inspection schedule, inspection area, types of materials, accessibility, costs and expected defects types are also important. Some techniques provide good quantitative information but perform poorly when insulation is introduced. Therefore, new methods are required to monitor corrosion which can be used for long-term operation, minimal volume, and at lower cost and risk.

Table 2.1 Advantages and limitations of NDT&E technologies for corrosion characterisation.

NDE & SHM Methods	Advantages	Limitations
Optical	Non-contact; fast; full-field; can be operated by at higher temperatures; real-time.	Special safety regulations for laser operation; very sensitive to environmental conditions; can't penetrate the insulation layer.
Ultrasonic	Fast; inspect large area; penetrate deeply in materials; excellent for corrosion and defect detection; can be automated.	Requires coupling material and contacting with surface; reference standards are required; surface needs to be smooth.
Radiography	Broad range of materials and thicknesses can be inspected; inspection film can be recorded.	Requires a minimum intensity difference; radiation safety requires precautions; expensive; requires to access to both sides of the structure.
MFL	Portable; Inexpensive; sensitive to surface and near-surface flaws and corrosion.	Bulk size; limited to ferromagnetic materials; requires post-inspection and surface preparation.
EC	Quick to perform; moderate cost; no probe contact required.	Limited to materials with electrically conducting; penetration depth is limited; surface must be accessible and smooth.
PEC	Penetrating deeper without altering the insulation; non-contact.	Limited inspection area; inability to detect localised corrosion.
ECPT	Good for surface corrosion; high sensitivity; remote sensing; fast; inspect large area.	Expensive; requires heating and cooling of the system; reference standards required; poor resolution on thick sections.
THz	Non-contact; good resolution; inspect insulation layer properties; real-time; one-side manner; high sensitivity.	Expensive; complex wave interactions; sensitive to environments (moisture etc.).
EIS	Very sensitive; quick to perform; time dependent data is available; can detect non-visible damaged areas.	Expensive; complex data analysis for quantification; localized detection requires knowledge of damaged area.

2.3 RFID and RFID Sensing Survey

There are several developed wireless sensing technologies based on surface acoustic wave and Lamb wave transducers [99, 100]. Also, several battery-free approaches to the

passive RFID sensing of physical, chemical, and biological characteristics have been explored based on low frequency [101] and high frequency RFID sensors [102]. Nonetheless, none of above methods has used HF RFID sensors for corrosion detection. This section reviews the literature regarding HF passive RFID-based sensors for corrosion detection.

Table 2.2 Types of RFID with different operating frequencies.

Type of RFID	Frequency Range	Advantages	Disadvantages
Microwave	2.45 GHz and 5.8 GHz	Fastest read rates; large read distance.	Very expensive; sensitive to liquids and metals.
Ultra High Frequency (UHF)	868 MHz ~ 956 MHz	Good read distance; faster read rate	Application restrictions; environment influence.
High Frequency (HF)	13.56 MHz	Inexpensive; fast read rate; tag can be passive; cheap device.	Limited read distance;
Low Frequency (LF)	125 kHz ~ 134.2 kHz	Tag can be passive; cheap; very small size of devices.	Relative small communication distance (up to 0.5 m); slow read rate.

Radio frequency identification utilizes radio frequencies to transfer power and data between a reader and a tag. RFID systems employ a broad range of operating frequencies for a wide variety of applications, depending on various factors such as cost, communication distance and tolerance to certain environmental conditions such as

proximity to near metals or liquids. Table 2.2 shows a list of the most common RFID operating frequencies.

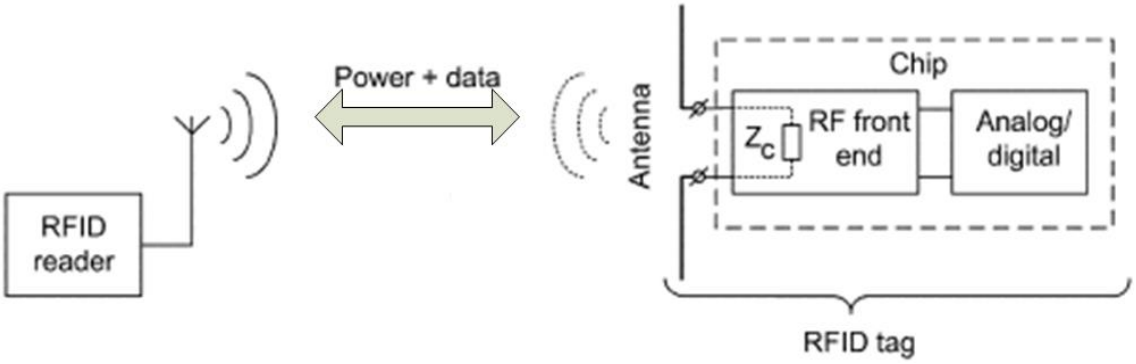

Figure 2.12 Operating diagram of an RFID system [103].

A typical RFID system is shown in Figure 2.12. It consists of a reader and a transponder (tag). The operating principles of RFID systems are as follows:

- Reader: the energy is transferred from the reader to the tag by emitting electromagnetic waves through coils. The functions of the reader include: (1) to transfer enough power to the tag to energise it; (2) to receive the data stored in the tags memory via a response signal from the tag; and (3) to rewrite data to the tag's memory.
- Transponder (tag): the tag absorbs energy from the reader to become charged up, and begins transmitting its modulated response signal.
- There are two kinds of tags: passive and active [103]. The main difference between the two is that no batteries are needed for the passive transponder's circuit.
- Passive tags can be charged in two ways: near-field coupling (for LF and HF) or far-field emission (for UHF and Microwave frequency band).

RFID tags are originally developed to be electronic labels with low cost [104], and a redesigned integrated circuit (IC) chip with a self-powered approach [105] or a battery

is required by most of typically RFID-based sensing approaches. This prevents many RFID devices from being used in sensing applications [106]. Although RFID sensors with battery power can provide large communication distances [107], unfortunately high costs due to system maintenance and complexity are compounded by the need for a battery, and the lifetime of such systems is reduced compared to passive ones.

Therefore, passive tags become more relevant when there is a requirement for small sensor size. Moreover, passive tags can be used for cost-effective long-term monitoring. Hence, passive RFID tags have been used for a variety of sensing applications, such as of temperature [108], humidity [109], strain [110], food permittivity [111] and chemical sensing [112]. In the following discussions, passive RFID applications for sensing in general are considered first, and more specific cases of passive RFID-based sensors for corrosion detection are then reviewed.

Marrocco [113] presented a special antenna design for human body bio-monitoring. A planar UHF tag antenna was introduced which is based on the nested slot suspended feeding patch. The sensing mechanism detects mismatches between the antenna's input impedance with respect to a change in the tagged human body.

Emran *et al.* [109] demonstrated a novel low-cost UHF RFID tag for the sensing of the relative humidity of objects. This tag consists of passive microwave circuit including a humidity sensitive polymer material. This polyimide material absorbs and holds moisture near the antenna of the tag, thus changing its operating characteristics, where a change in moisture can be detected as a shift in the power transmission from the tag's antenna. This study achieved a reduction in the overall size of the tag sensor to 15 mm × 6.8 mm, and used a transmission coefficient with a single bit for humidity sensing.

Potyrailol *et al.* [114] developed cost-efficient passive 13.56 MHz RFID tags which were coated with a solid polymer electrolyte sensing film for multiple-purpose sensing,

where the physical and chemical properties of interest are correlated with the obtained complex impedance of the resonant frequency of the RFID coils. Principal component analysis is applied to several parameters from the measured complex impedance with RFID-based sensing. An independent lift-off feature is extracted to improve the sensitivity of RFID-based sensing to the position of the reader [115].

Carkhuff and Cain [116] proposed a passive RFID-based wireless sensor to monitor corrosion in concrete bridges. Their wireless sensors employed short-range RFID to power the sensor and to read measurements. Unlike other RFID-based sensors, the prototype presented by the authors adopted inductive coils: one for picking up the power from the reader, while the other was for communication. Temperature and bulk resistance were measured by these sensors.

Walter *et al.* [117] also presented a corrosion sensor based on RFID to be embedded in concrete. This sensor employed a potentiostat to examine the linear polarization of corrosion areas. An RFID reader was adopted to generate an electromagnetic field transmitting power to the sensor. The measurement of data transmission also depended on this field. Repositioning effects were compensated for by digitally modulating the measured data with the carrier signal.

Mohammed *et al.* [118] developed the use of passive 125 kHz low frequency RFID tags as corrosion sensors. Each sensing tag was placed on the metal surface and then the reader positioned at a certain height was used for specific to provide power and receive measurement data. Three uninsulated steel samples were exposed to the atmosphere and thus corroded over different durations of 1, 3 and 6 months. The amplitude of the tag's responding signal depended on the stage of corrosion reached.

The use of passive RFID tags for sensing can be found across the literature to detect a variety of phenomena. Its low cost, small size and battery-free operation are the most

important factors leading researchers to further explore this technology for sensing. Most of these works of passive RFID sensing involve modifications to tags through attaching either special reactive thin films or sacrificial elements to the tags. These modifications not only increase costs but also limit the lifetime capability of the tags. The method proposed in this study overcomes these problems by using the interaction of the coil of tag with corrosion and metal as the sensing mechanism. No modifications to the tag are required, which allows commercial off-the-shelf tags to be used. Nevertheless, the sensing area and lift-off tolerance of RFID-based sensing is limited by the size of tags. In the following section, the use of microwave NDT is proposed for detection under thick insulation.

2.4 Microwave and Millimetre Wave NDT Survey

Microwave frequencies range is between 300 MHz to 300 GHz. Unlike ultrasound signals, dielectric insulation materials can be easily penetrated by microwave signals without suffering from high attenuation and then internal structures of materials can interact with these microwave signals. These microwave signals would then totally reflect at the metal surface. Therefore, these signals travel twice through the areas of corrosion and defects, which increases the possibility of detecting them under insulation. With the measurement of transmitted or reflected microwave signals, microwave NDT techniques examine magnitude or phase in inspecting the specimen. Furthermore, reflection and transmission properties are influenced by lift-off and the frequency of operation during inspection [119].

In the last decade, researchers have shown an increased interest in microwave-based NDT&E techniques to replace previously mentioned methods. These methods have been utilized in various studies [120-122], including in ground penetrating radar (GPR) [123], radar sensors [124, 125], open-ended waveguides [126], and coaxial probes

[127]. The potential of using microwave NDT&E for defect detection has already been demonstrated [128], and Yeh and Zoughi initially developed microwave NDT&E techniques to detect and quantify surface defects on metals with an open-ended waveguide [129].

Moreover, many studies have established the basis for the modelling of defect detection. Huber *et al.* [130, 131] used transverse magnetic fields to obtain orthogonal mode vectors, and then expanded the method to the estimation of unknown equivalent magnetic currents with the method of moments. In addition, they provided an analysis for the modelling of fatigue. Mazlumi and Sadeghi [132] presented a technique adopting the Max-Lloyd quantization algorithm to predict the output signal for scanning of arbitrarily shaped fatigue cracks on metal.

Maierhofer *et al.* [133] employed 2.5 GHz GPR to detect damage on concrete up to 500mm. Kharkovsky and Zoughi [122] gave an overview of microwave- and millimetre wave-based NDT&E methods. A wide range of applications was discussed, which included detecting corrosion and the precursors of pitting in insulated structures backed by aluminium and steel. Case *et al.* [134] demonstrated inspection results of a 25.4 mm thick honeycomb sandwich panel with millimetre wave holographical inspection, and good resolution have been achieved at about 14 mm depth.

Far-field [135, 136] and near-field [137, 138] microwave NDT approaches detect defects through the magnitude and phase variation of the reflection coefficient. From the standpoint of high resolution, signal interpretation, and insensitivity to relative position between sample and antenna, a far-field mode is preferable; but it requires large-aperture antennas to achieve good spatial resolution. In most situations, the use of large antennas is generally impractical and inconvenient. Moreover, near-field mode can

be performed indoors, eliminating influences due to weather, electromagnetic interference etc.

Near-field microwave imaging techniques with open-ended rectangular waveguide are commonly used for NDT fields. For producing image, the waveguide probe is scanned over sample under test, and the measured reflected signals are used to form a 2D intensity raster image [139]. Ghasr *et al.* [140] used near-field Ka-band and V-band open-ended rectangular waveguide for detection of corrosion precursor pitting under insulation. The difference between the phase and magnitude of reflected signals were used to produce high resolution image for pit dimension evaluation. Nasser *et al.* [141] demonstrated an open-ended rectangular waveguide sensor operating in the near-field at a frequency of 24 GHz for defect detection and classification in non-ceramic insulators. Defects were detected and classified by using a novel artificial neural network.

However, microwaves cannot efficiently penetrate through conductive materials, which mean that only surface defects can be sensed and it is difficult to detect subsurface defects. In this study, HF passive RFID-based corrosion sensing in conjunction with microwave NDT is proposed for corrosion and defects monitoring under insulation. This is because RFID-based sensing can provide long-term monitoring of localized areas, while microwave NDT can provide images of larger areas via scanning.

2.5 Chapter Summary

The challenges posed by the development of corrosion and defects under insulation are inaccessibility and lift-off effects caused by the variation of the insulation layer. Lift-off effects can cause errors in the detection and measurement of corrosion. Moreover, thick insulation layers results in a large lift-off, which leads to a reduction in sensitivity. In addition, the challenges associated with the characterization of corroded metal require an understanding of microstructural and physical changes prior to the initiation and

growth of corrosion. In most cases of corrosion, changes in the intrinsic material properties are dominant in the early stages. Physical damages, such as defects, occur when corrosion has exceeded a critical limit. Furthermore, their concealed nature results in the accumulation of such changes for long periods of time, leading to the critical limit being exceeded, and potentially catastrophic failures will become more likely.

An extensive literature survey in this chapter has been followed by a discussion of NDT&E techniques using optical, acoustic, electromagnetic, thermal and electrochemical methods for the detection of defects and corrosion. It has been shown that the majority of techniques are limited when it comes to the online in-situ monitoring of corrosion and defects under insulation, primarily due to the thick insulation layer. Solutions to overcome this problem typically involve either removing the insulation, applying much higher output power using bulky, expensive equipment, or using inspection holes in the insulation layer to send signals along the length of an insulated structure.

The HF passive RFID-based sensing identified in the literature demonstrates potential for small-size, cost-effective, battery-free and long-lifetime monitoring. Passive RFID-based sensors have been adopted to sense a wide range of diverse phenomena. Due to their battery-free operation, passive RFID-based sensors have been embedded into structures such as concrete for long-term condition monitoring. However, the sensing tags used in the majority of studies employ thin films, potentiostats or sacrificial elements attached to the tags. The degradation in performance which occurs when tags are placed onto metallic structures is another challenge not addressed by existing studies. Furthermore, long-term monitoring with RFID tags is limited by the size of the tag when it comes to monitoring larger structures with relatively thick insulation. Therefore, a microwave NDT-based imaging system is required to provide the remote sensing of large areas under thick insulation.

To address these challenges under insulation, HF passive RFID tags in conjunction with a microwave NDT-based imaging system are proposed in this study. This system aims to address the following issues:

- To obtain the grade and progression of corrosion over different exposure times in mild steel correlated with surface roughness, conductivity, permeability and permittivity.
- For the HF passive RFID system, the lift-off effect between the reader and tags needs to be addressed by applying multivariate statistical analysis methods to obtain a custom feature for the evaluation of corrosion and to reduce lift-off effects.
- The system must be cost-effective, and use off-the-shelf components. To minimise costs further, the tag is to be unmodified. The sensing mechanism is based on the interaction between the tag coil and corrosion.
- A suitability study is conducted for the monitoring of large area under thick insulation in conjunction with the microwave NDT system. Methods of statistical analysis in conjunction with a linear sweep frequency are applied to extract features to reduce lift-off effects and improve the resolution of microwave imaging.

The next chapter introduces the research methodology used in this study. It includes a research diagram, discussion of the theoretical background of HF passive RFID systems and microwave NDT-based imaging. An explanation of feature extraction using the principles of interpretation and characterisation algorithms is also provided.

Chapter 3. Methodology

Based on the challenges identified in literature review, this chapter outlines the methodology used for passive high frequency RFID-based sensing in conjunction with the microwave NDT system. An investigation is proposed to address the challenges of detection under insulation. As can be seen in Figure 3.1, this includes the HF RFID-based taking into account theoretical concerns in monitoring under insulation over a localised area to overcome inaccessible, a microwave NDT-based imaging system to overcome thick insulation over a large area, and the characterisation of corrosion through feature extraction.

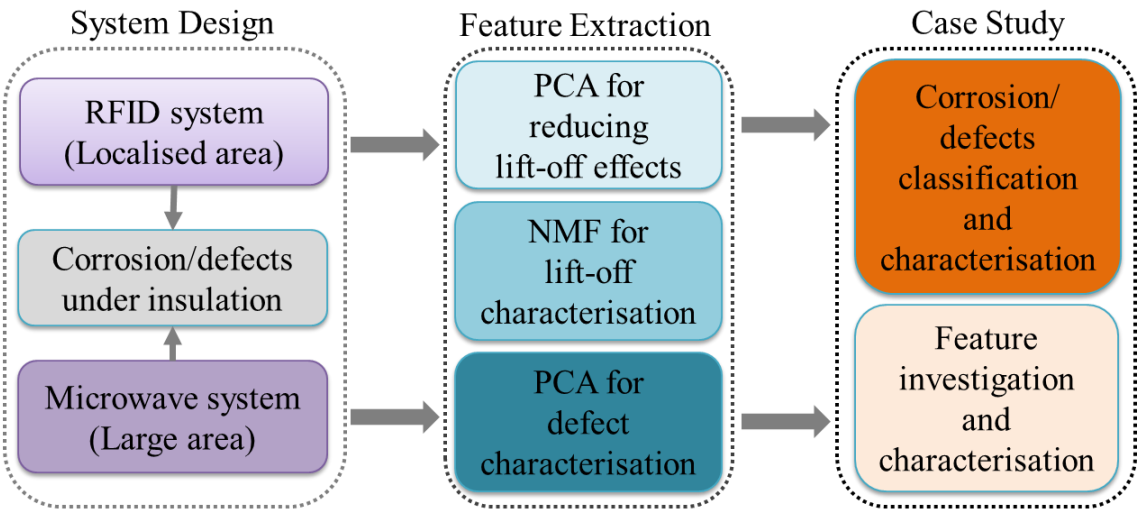

Figure 3.1 Research diagram for RFID sensing and microwave NDT.

The behaviour of the RFID-based sensing system near metals is discussed in Section 3.1. The theoretical background of the RFID sensing system is also introduced, covering electromagnetic wave interaction and physics of the mechanism as well as inductive coupling. Section 3.2 describes the operational principles of microwave NDT-based imaging with a scanning system. The relevant processing algorithms based on measured data are presented in Section 3.3, including PCA and NMF. A chapter summary is then provided in Section 3.4.

3.1 Theoretical Background of HF Passive RFID

3.1.1 Fundamental Operating Principles

The LF/HF passive transponders (tags) operate passively with inductive coupling. To operate the microchip of the tags, passive tags need to obtain all of the energy required from the RFID reader, as shown in Figure 3.2. Therefore, the reader coil will generate an electromagnetic field and penetrate the tag's coil. This is because the distance between the reader and tag is much smaller than the wavelength of the operational frequency (a wavelength of 13.56 MHz it is about 22.1 m; for 125 kHz it is about 2400 m). An alternating magnetic field can be used to simplify the electromagnetic field.

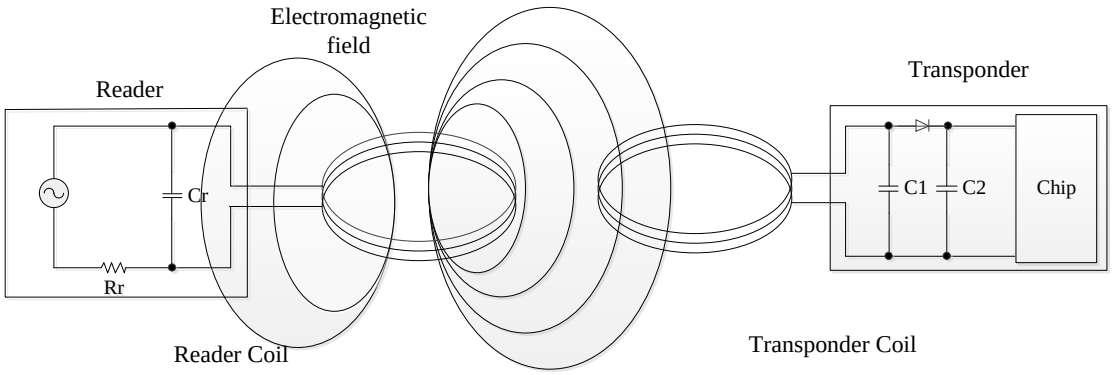

Figure 3.2 Principal of the near-field inductive coupling between the coils of reader and tag [134].

The coil of tag is penetrated by the emitted magnetic field, which is situated away from the reader's coil by a certain distance. The inductance of the tag's coil generates a voltage *U*i. After being rectified, the microchip is powered by this voltage. A capacitor *C*r is connected in parallel with the reader's coil, and the capacitance selected for this capacitor is used to form a resonant frequency with the inductance of the reader's coil. The resonant frequency corresponds to the operational frequency of RFID system. Required field strengths are generated by the reader's coil, which is used to power the remote operation of the tags.

When the operational frequency *f* increases, less inductance of the tag's coil is required. Therefore, the winding number *n* is decreased (at around 100 – 1000 windings for 125 kHz, but only 3 – 10 windings for 13.56 MHz). Since the induced voltage of the tag is proportional to the operational frequency *f*, the reduction of the winding number at higher frequency range leads to higher efficiency in power transfer. This is one reason for the use of high frequencies in this research.

In general, sum of current strengths along a coil is equal to the integral of magnetic field strengths [142]:

$$\sum I = \oint \vec{H} \cdot \overrightarrow{ds} \tag{3.1}$$

The field strength *H* for RFID coils can then be calculated using this formula.

The field strength *H* of distance *r* can be found as follows:

$$H = \frac{1}{2\pi r} \tag{3.2}$$

HF RFID systems employ coils to induce an alternating magnetic field, in order to form inductive coupling. The field strength of a coil along *x*-axis can be determined by using the following equation [143]:

$$H = \frac{I \cdot N \cdot R^2}{2\sqrt{(R^2 + x^2)^3}} \tag{3.3}$$

where *x* is the distance from the coil centre, *R* is the circle radius, *N* is the winding number, and $x < \lambda/2\pi$ and $d \ll R$ are boundary condition when applying this equation.

The following equation can be used to find the field strength at a distance *x* for a rectangular coil with overall dimensions of $a \times b$:

$$H = \frac{N \cdot I \cdot ab}{4\pi\sqrt{\left(\frac{a}{2}\right)^2 + \left(\frac{b}{2}\right)^2 + x^2}} \cdot \left(\frac{1}{\left(\frac{a}{2}\right)^2 + x^2} + \frac{1}{\left(\frac{b}{2}\right)^2 + x^2} \right) \tag{3.4}$$

The coil will generate a magnetic flux Φ around itself. Normally, there are *N* windings at the same area *A* with the same flowing current *I*. The total flux ψ is the sum of each conduction loop with the same proportion Φ:

$$\Psi = \sum_N \Phi_N = N \cdot \Phi = N \cdot \mu \cdot H \cdot A \tag{3.5}$$

Inductance *L* is the ratio of the interlinked flux ψ to current *I*, which can be determined by:

$$L = \frac{\Psi}{I} = \frac{N \cdot \Phi}{I} = \frac{\mathrm{N \cdot \mu \cdot H \cdot A}}{I} \tag{3.6}$$

The characteristic variables of coils include inductance. This coil's inductance is totally dependent on the properties of the material and the geometry of the coil.

Eq. 3.6 can be simplified when the coil diameter *D* is much bigger than the wire diameter *d* (*D*/*d* > 10000):

$$L = N^2 \mu_0 R \cdot \ln\left(\frac{2R}{d}\right) \tag{3.7}$$

where *N* is the winding number, $\mu_0 = 4\pi \times 10^{-7} \mathrm{V \cdot s/(A \cdot}m)$ is the permeability of free space, *R* is the coil radius, and *d* is the diameter of the wire.

Mutual inductance is employed to describe the coupling of RFID systems via a magnetic field. It has the same dimensions and units as inductance. The mutual inductance *M* can be determined using the following equation:

$$M = \frac{\mu_0 \cdot N_1 \cdot R_1^2 \cdot N_2 \cdot R_2^2 \cdot \pi}{2\sqrt{\left(R_1^2 + x^2\right)^3}} \tag{3.8}$$

where μ_0 is the permeability of free space, N_1 is the winding number of the reader's coil, N_2 is winding number of the tag's coil, R_1 is the radius of the reader's coil, R_2 is the radius of the tag's coil, and x is the distance between the coils of tag and reader.

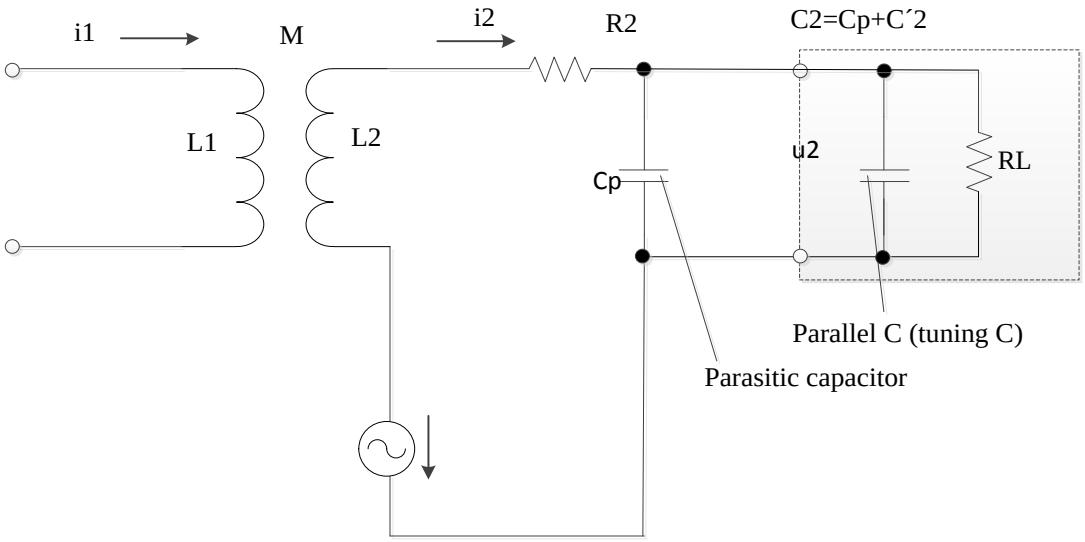

Figure 3.3 Equivalent circuit for inductive coupling of RFID coils [103].

With a passive RFID tag, the coil of tag serves as the power supply to provide energy to the microchip. For the purpose of significantly improving the efficiency of the RFID system, a capacitor is used to form a resonant frequency which corresponds to the operational frequency. This resonant frequency can be obtained using the Thomson equation:

$$f = \frac{1}{2\pi\sqrt{LC}} \tag{3.9}$$

A diagram of the equivalent circuit for coupled RFID coils is shown in Figure 3.3. In this magnetically coupled RFID coils, the coil of the reader is represented by L_1. The natural resistance of the tag is represented by R_2, and L_2 is the coil of tag, and R_L is the load resistor which represents the current consumption of the microchip. The resonant frequency is formed by connecting the tag coil L_2 in parallel with an additional capacitor C_2 that corresponds to the operational frequency of the RFID system.

The voltage u_2 can be found as follows:

$$u_2 = \frac{\omega \cdot k \cdot \sqrt{L_1 L_2} \cdot i_1}{\sqrt{(\frac{\omega L_2}{R_L} + \omega R_2 C_2)^2 + (1 - \omega^2 L_2 C_2 + \frac{R_2}{R_L})^2}} \tag{3.10}$$

where $C_2 = C_2^{'} + C_p$, $C_2^{'}$ is a parallel capacitor and C_p is the parasitic capacitance.

3.1.2 Theoretical Background of HF RFID-based Sensing

Figure 3.4 (a) and (b) illustrates the operational principle of RFID-based sensing, including sensing and the transmission of measured data. Mutual inductance coupling between the reader and tag is used to provide energy and measure complex impedance data from the RFID tag. A commercial RFID reader is used to acquire measurement data from the RFID tag.

A model of the mutual inductance coupling circuit can be used to describe the interaction between RFID tag and reader. It includes Z_R and Z_T, where Z_R is the intrinsic impedance of the reader and Z_T is the intrinsic impedance of the tag. M is the mutual inductance and Z_M is the measured impedance across the coil of the reader. Z_M can be calculated as follows [144]:

$$Z_M = Z_R + \frac{\omega^2 M^2}{Z_T} \tag{3.11}$$

where ω is the radian of operational frequency. The importance of controlling M for accurately measuring responses of the RFID tag is illustrated by Eq. 3.11 because Z_M is proportional to the square of M. This is one main reason why the lift-off effect needs to be discussed in the following section.

As can be seen from Figure 3.4 (b), the equivalent circuit of the tag is made up of the inductance L_a, the capacitance C_a, and the resistance R_a of the tag's coil. The sensing

region (corrosion area) consists of a capacitance C_s and a resistance R_s. The microchip involves a capacitance C_c and a resistance R_c.

Corrosion in steel is a general term for a series of iron oxides (haematite α-Fe_2O_3, magnetite Fe_3O_4 and maghaemite γ-Fe_2O_3), hydroxides (ferrous hydroxide $Fe(OH)_2$ and ferric hydroxide $Fe(OH)_3$, goethite α-FeOOH), and chloride (ferrous chloride $FeCl_2$ and ferric chloride $FeCl_3$). These iron oxides and hydroxides exhibit different electromagnetic properties. For example, haematite is a semiconducting mineral [145] and goethite has lower conductivity than haematite [146]. However, the conductivity of magnetite is significantly higher ($\times 10^6$) than that of haematite, due to exchange of electrons between Fe^{2+} and Fe^{3+} ions [147].

Furthermore, with different exposure periods, the thickness of the corrosion layer will be different. Therefore, the capacitance C_s and resistance R_s are changed with different corrosion samples with the RFID tag attached. This results in changing the measured impedance of tag Z_T. As mentioned in the previous section, HF RFID-based sensing is proposed to form a novel method for corrosion sensing under insulation. The operation principles of this RFID-based sensing system are described as following:

1. The RFID tag is placed on the surface of a metal and the reader placed at a certain height above the tag.

2. The impedance of the tag's coil will change when the tag begins to transmit its modulated response signal. There will be inductive coupling between the metal and the coil of the tag. The inductive coupling between the tag and metal is greater than that between the reader's coil and the metal.

3. The resulting eddy currents will cause inductive loading effects on the coil of the tag. This will then distort the tag's response signal.

4. At the reader side, the distorted signal received will be analysed to extract the characteristic of the metal under test.

5. At the end, the extracted characteristics of the metal condition will be compared with reference signals.

The impedance spectrum of $Z_M(f)$ is obtained by connecting the RFID reader to a vector network analyser. A vector network analyser developed by Agilent (Agilent ENA E5071B) is used to operate a linear sweep frequency over the range of interest, which is in general centred at 13.56 MHz with a scanning range of 10 MHz ~ 20 MHz.

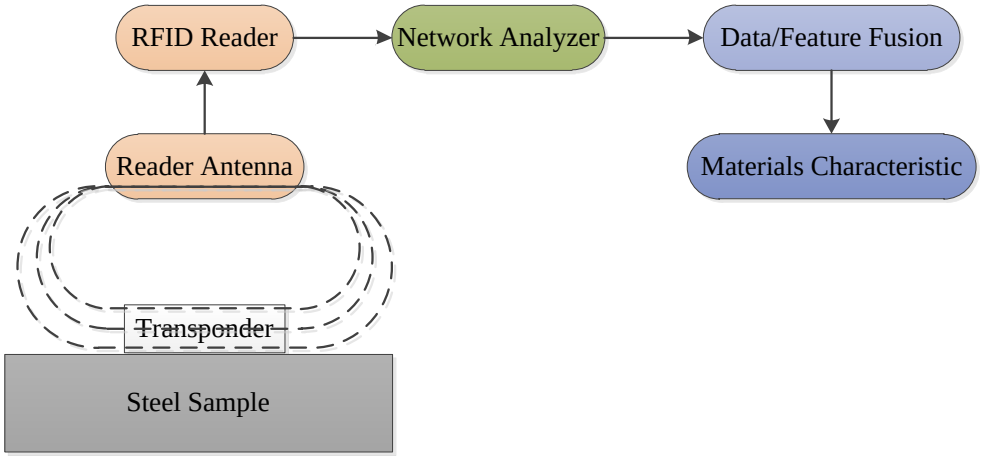

(a) System schematic of the measurement of complex impedance from the coil of the reader.

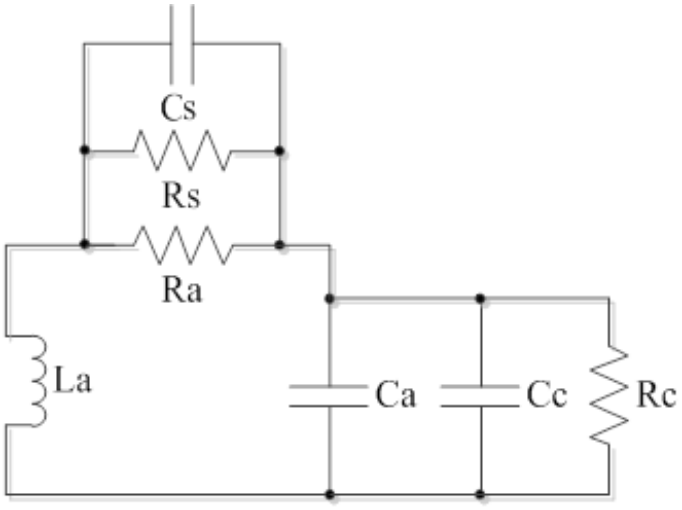

(b) Tag equivalent circuit.

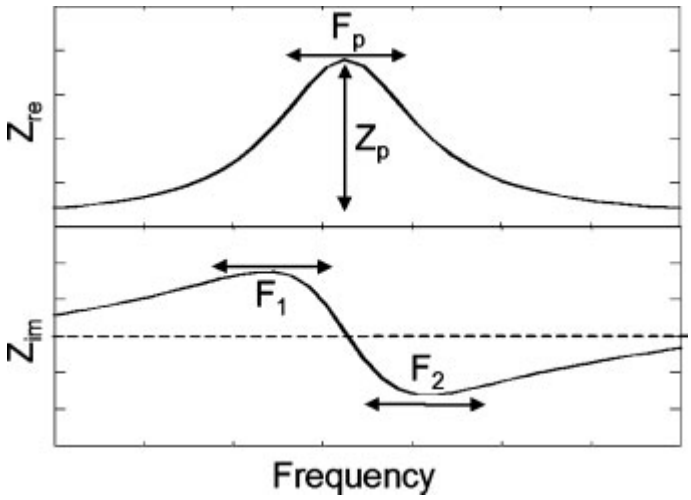

(c) Measured real part of the impedance spectrum (top) and imaginary part of the impedance spectrum (bottom).

Figure 3.4 Operational principle of HF passive RFID-based sensing.

To achieve accurate measurements with the RFID sensor, real $Z_{re}(f)$ and imaginary $Z_{im}(f)$ parts of the measured impedance spectrum $Z_M(f)$ are obtained. This measured impedance spectrum can be used to calculate several spectral parameters. An illustration in Figure 3.4 (c) represents the measured $Z_{re}(f)$ and $Z_{im}(f)$. These spectral parameters include the position of resonant frequency F_p of $Z_{re}(f)$ and its peak value Z_p, and positions of resonant F_1 and anti-resonant F_2 frequencies of $Z_{im}(f)$ [114, 115, 148]. Other parameters can be determined too, such as the peak values Z_1 in F_1 and Z_2 in F_2.

These parameters are used for further investigation: peak-to-peak amplitude V_{pp}, the peak value of Z_p, the peak-to-peak magnitude of imaginary $Z_{pp} = Z_1 - Z_2$. By measuring these parameters simultaneously from the RFID tag, corrosion progression over different exposure periods can be investigated and understood.

The fundamental operating principle of RFID has been described in section 3.1.1. It relies on magnetic flux between the coils of the reader and the tag. In free space, the magnetic flux caused by the reader penetrates the tag's coil. When the tag is placed on metal, the metal in the vicinity of the tag will generate an eddy current and a magnetic field induced by this eddy current reduces the original magnetic field required for

energy and data transmission. This reduction decreases the amount of power absorbed by the tag and hence the reading distance is reduced. Therefore, the lift-off tolerance of RFID sensing is limited. Moreover, corrosion sensing is reliant on the interaction of these eddy currents.

As corrosion developing on the metal, the thickness of the corrosion layer increases. It results in decrease in electrical conductivity and magnetic permeability, which will increase the penetrating magnetic flux towards its value in free space. On the hardware side, four commercially available tags were selected as the corrosion sensors in this research. The tags are of a variety of sizes and shapes to cover different surfaces and applications. The reader unit is built with a 100 mm by 80 mm coil. Tests have shown that the reader is capable of energising and reading a tag from a distance of up to 25 mm, which is not sufficient for thick insulation. Meanwhile, the monitoring area with the RFID-based sensing is limited to the size of the tag which is not enough for structural monitoring. Therefore, microwave NDT is proposed to overcome the problems of large area monitoring and big lift-off issues.

3.2 Theoretical Background of Microwave NDT

The problems of the transmission and reflection of microwaves from a multilayer dielectric medium have been investigated by many researchers [149]. The following equations, are inspired by the model presented by Sayar, Seo and Ogawa [150]. A waveguide probe with a dominant mode excitation (TE_{10}) is used to illuminate the structure with electromagnetic waves at microwave frequencies. The waveguide aperture lies in the x-y plane.

Figure 3.5 illustrates a layered sample consisting of an insulation layer and backed with a steel plate. This plane electromagnetic wave is linearly polarized. The near-field of an open-ended waveguide is used to irradiate an incident signal. This incident signal is

then penetrating the insulation layer and reflected by the conducting plate (steel layer). The ratio of these two signals gives the effective reflection coefficient of the sample under test. This layered sample consists with a homogeneous dielectric layer of relative permittivity ε_r and thickness d_1, and a backed conducting substrate. This insulated material is irradiated by microwave signals. The d_2 is the thickness of a certain defect which presents between the insulation layer and metal substrate.

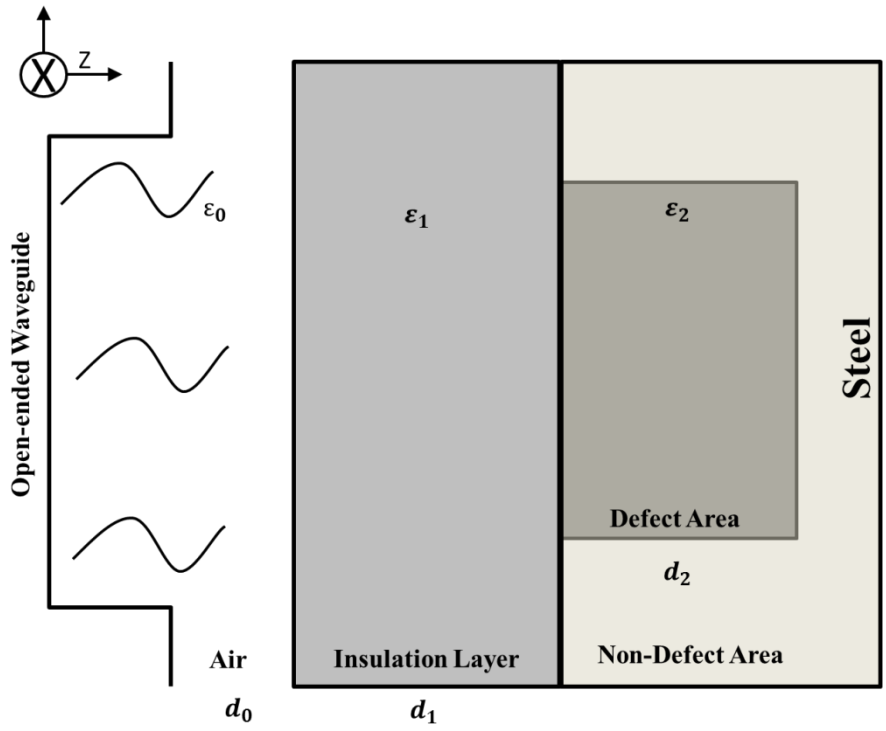

Figure 3.5 Electromagnetic wave reflection and transmission for insulated metal.

The magnitude and phase differences between reflection coefficients of non-insulated and insulated samples are related to the thickness of the insulation layer and its permittivity ε. The lift-off d_0 here is the distance between waveguide and sample. There should be a small air gap (non-contact) between the probe and the sample surface in order to give a smooth, simple movement of the waveguide. The propagation constant represents the change in the electromagnetic wave as it propagates in a given direction.

The propagation constant is a complex quantity which can be written as: $\gamma = \alpha + i\beta$, where α is the real part, which is called the attenuation constant. Another symbol β is

actually the imaginary part, which represents the phase constant. Because the samples used in the following chapters have no defects in the insulation layer, whose thickness is almost the same in each sample, therefore the attenuation is approximately the same for each sample and can be considered as a constant. During defect detection, when there is a defect on the steel, the attenuation and reflection signal significantly differs between the defect area and non-defect area. The characteristics of this difference in recorded reflected signals are utilized for the detection and sizing of defects in the specimen.

The calculation of the reflection coefficient for such multiple media involves the derivation of the forward and backward travelling electric and magnetic field components in each layer, based on a known incident field and the application of appropriate boundary conditions at each interface. The broad and narrow transverse dimensions of the waveguide are represented by a and b. Hence, with the TE_{10} mode, the excitation aperture field distribution is given by:

$$E_y(x,y,0) = \begin{cases} \sqrt{\frac{2}{ab}} cos\left(\frac{\pi x}{a}\right), & (x,y) \in aperture \\ 0, & (x,y) \notin aperture \end{cases} \tag{3.12}$$

Complete set solutions for the field components for near-field open-ended waveguide NDT have been constructed by Bakhtiari et al [151]. The variational expression for the admittance of the waveguide can be written as:

$$y_s = \frac{j}{(2\pi)^2\sqrt{1-(\frac{\lambda_0}{2a})^2}} \int_{R=0}^{\infty}\int_{\theta=0}^{2\pi} \mathcal{J}\left\{(K^2 - R^2cos^2\theta)\left(2C_\phi + \frac{j\mathcal{J}}{X_z}\right)\right\} R\, d\theta\, dR \tag{3.13}$$

$$\mathcal{J} = \sqrt{\frac{2A}{B}} \frac{4\pi\, sin(\frac{X_y B}{2})\, cos(\frac{X_x A}{2})}{X_y[\pi^2 - (X_x A)^2]} \tag{3.14}$$

$$C_\phi = -\frac{\mathcal{J} e^{jX_z D}}{2X_z\, sin(X_z D)} \tag{3.15}$$

$$A = k_0 a \tag{3.16}$$

$$B = k_0 b \tag{3.17}$$

$$D_{\text{non-defect}} = k_0(d_0 + d_1) \; or \; D_{\text{defect}} = k_0(d_0 + d_1 + d_2) \tag{3.18}$$

$$K = \frac{k_1}{k_0}, X_x = R\cos\theta, X_y = R\sin\theta, X_z = \sqrt{K^2 - R^2} \tag{3.19}$$

where R and θ are the new variables of integration in polar coordinates. The complex reflection coefficient, Γ is related to the complex admittance y_s by:

$$\Gamma = \frac{1-y_s}{1+y_s} \tag{3.20}$$

From the above equations, the reflection coefficient is different when there is a defect on the steel sample. Both amplitude and phase of reflection coefficient can be used for defect detection. Macroscopically, when there is a defect under these insulated metal samples, they exhibit surface discontinuities. Due to the differences in the nature of the physical properties, these discontinuities are reflected in microwave changes in attenuation and absorption in the metal. Therefore, defect information such as size and location can be deduced from the reflection signals received from the C-scan.

From the standpoint of efficient wave propagation, signal interpretation, and insensitivity to relative position between sample under test and antenna, a far-field mode is preferable; but it requires large-aperture antennas to achieve good spatial resolution. In most situations, the use of large antennas is generally impractical and inconvenient. To avoid affecting spatial resolution, small-aperture open-ended waveguides are used in the near-field mode.

For higher resolution and wider viewing angle of the microwave images, acquiring enough scattering information from sample at different viewing and illumination angles

is necessary. There are many methods proposed to increase the scattering information: frequency diversity technique [152], multiplexing technique [153] etc. In this thesis, the simultaneous multi-source illumination arrangement is exploited with the use of a linear frequency swept technique to enlarge the illuminated area over the scattering sample surface. The scattering information is then recorded by open-ended waveguide.

These reflected signals are measured and then used to calculate the reflection coefficient using Agilent VNA in conjunction with a linear sweep frequency. These complex reflection coefficients are complex numbers whose phase and magnitude refer to frequency spectrum variations. This measured data will provide information about the location and dimensions of the defect [154]. This is a very sensitive interaction and is a function of defect dimensions and placement within the waveguide aperture.

3.3 Interpretation and Characterisation Algorithms

Further processing of measured data from the proposed systems is required, in order to gain characterisation information about detected corrosion and defects. Moreover, the lift-off effect introduced by insulation layers can be reduced. In the following sections, the algorithms for principal component analysis (PCA) and nonnegative matrix factorization (NMF) are presented.

3.3.1 PCA for RFID Sensing Characterisation

PCA is a modern method of data analysis which transforms waveform data into uncorrelated eigenvector components corresponding to maximum variability while eliminating collinearity within the data [155]. As a result, the dimensionality of the data is lowered. The use of PCA reduces the number of variables considerably, while still retaining much of the information in the original dataset. The biggest variation in waveforms is accounted for by the first principal component (PC1). Subsequent

components correspond to the remaining variability. Therefore, it is appropriate to extract the most dominant changes within the data using PCA and then to determine to which features these changes correspond. Hence, PCA is employed to extract a feature to reduce the lift-off effect. In Chapter 5, the PCA is applied to reduce the lift-off influences on measured real and imaginary parts of impedance values I. These principal components can be obtained by the following procedure:

1. Subtract the mean from the measured data matrix I.

2. Calculate the covariance matrix C of I.

3. Calculate the eigenvectors W and eigenvalues of the covariance matrix.

4. Generate PCA component space by multiplying W by the mean subtracted I:

$$\mathbf{PC} = \mathbf{W} \times \mathrm{I}^{T} \tag{3.21}$$

5. The measurement dataset is projected onto a subspace of lower dimensionality to eliminate the collinearity. Principal components (PCs) in terms of weighted sums of original variables.

6. These extracted dominant features PCs present the maximum amount of variations in dataset by linear transforms and project the dataset into orthonormal subspace.

PC1 and second principal component (PC2) are represented as linear combinations of optimally-weighted observed variables. They are orthogonal along the direction and optimal in the sense that components represent in terms of the maximal amount of variations in the measured data.

3.3.2 NMF and PCA for Microwave NDT Characterisation

A raster-like relative motion of a waveguide probe with respect to the sample gives a dataset that can be visualized as an image. Figure 3.6 can be considered as the tensor representation of mixing spatial-frequency spectrum observation $\mathbf{Y}$, which is the combination of non-defect and defect spatial-frequency spectrum sources respectively.

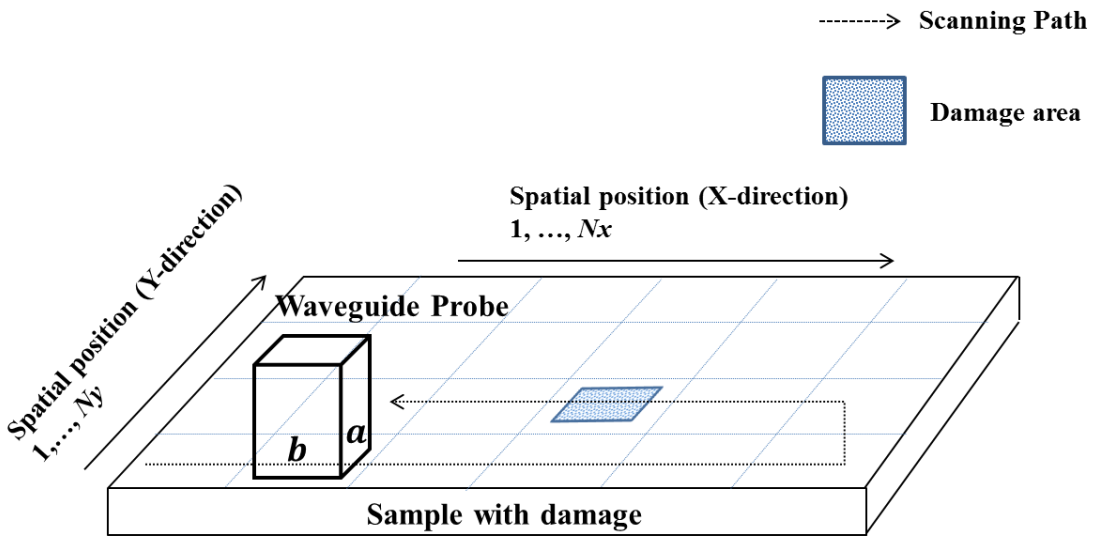

Figure 3.6 C-scan progress for microwave NDT.

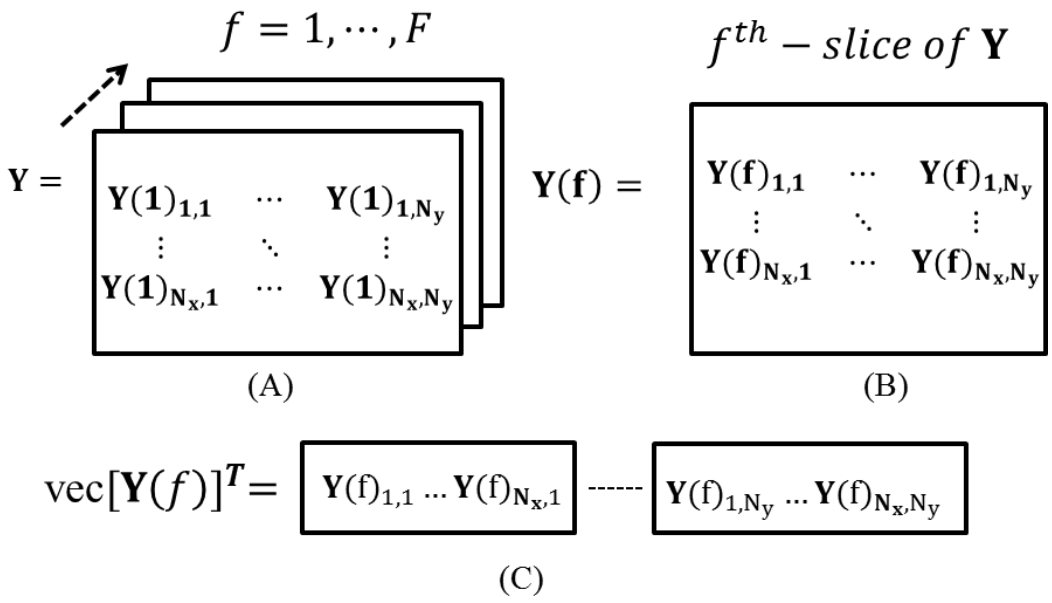

Figure 3.7 (a) Tensor representation of the image sequences $\mathbf{Y}$, (b) f^{th} frame of $\mathbf{Y}$, (c) visual explanation of $\mathrm{vec}(\mathbf{Y}(f))^T$.

In $\mathbf{Y}$, the frequencies are given by $f = 1, 2, \ldots, F$ and total frequency units are represented by *F*. The observed tensor can be expanded in a matrix format as $\mathbf{Y}' = [\text{vec}(\mathbf{Y}(1)), \text{vec}(\mathbf{Y}(2)), \ldots, \text{vec}(\mathbf{Y}(F))]^{\text{T}}$ where $\mathbf{Y}(f)$ denotes the spatial-frequency spectrum matrix with dimension N_x by N_y of the f$^{\text{th}}$ slice of $\mathbf{Y}$. A visual representation of this tensor flattening process is given in Figure 3.7.

Both PCA and NMF algorithms are used for classification with microwave NDT. The PCA is using singular value decomposition (SVD) in its calculation. PCA emphasises on the orthogonality of decomposition and NMF emphasises pattern analysis and separation. The pattern analysis and separation here refers to the decomposition of dataset where share similar characteristics within the NMF space and can be characterized as similar part of a large whole, it is an exclusive union set of the several other parts.

During this study, the NMF is used to represent the defect or non-defect spatial-frequency spectrum component which is obtained from microwave NDT. Under certain conditions (in the form of non-negative values), NMF decomposition is unique and constraints in the form of orthogonality are unnecessary (as required by PCA). In this study, the NMF can be adopted due to all elements in microwave NDT are nonnegative values. Both decomposition methods have advantages and disadvantages, and they have been widely used in feature extraction [93], pattern recognition [156] and data mining [157]. In this thesis, based on different purposes, the lift-off effect with line scanning is analysed using the NMF algorithm for defect pattern analysis and separation. The characterisation of the orthogonality of C-scan dataset from thick insulated specimens uses PCA.

3.3.2.1 Feature extraction using NMF

In order to extract defect and non-defect spatial-frequency characteristics from a given mixing power spatial-frequency observation $|\mathbf{Y}'|^{.2}$, solutions which use matrix factorization algorithms have recently gained in popularity and are commonly adopted for extracting the latent structure of measured data in a wide range of fields. There are various forms of matrix factorization in singular value decomposition [158] and non-negative matrix factorization [159].

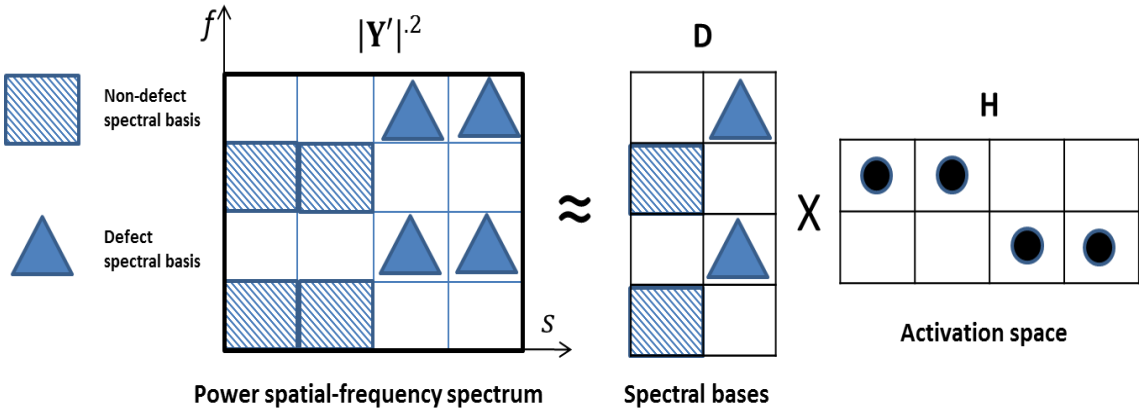

Figure 3.8 Visual explanation of the factorization process.

Paatero and Tapper [160] initially proposed NMF. To solve the optimization problem of NMF, Lee and Seung [159] developed the multiplicative update (MU) algorithm based on Kullback-Liebler divergence and the least square distance. Other families of parameterized cost functions have also been presented such as Beta divergence [161]. Given the mixing power spectrogram of $|\mathbf{Y}'|^{.2}$, two non-negative matrices are produced by factorizing the matrix with NMF where all elements must be equal to or greater than zero as in:

$$|\mathbf{Y}'|^{.2} = \sum_{i=1}^{N_s} |\mathbf{X}'|_i^{.2} \approx \sum_{i=1}^{N_s} \mathbf{D}_i \mathbf{H}_i \tag{3.22}$$

where $\mathbf{D}_i \in \Re_+^{K\times\ell}$ and $\mathbf{H}_i \in \Re_+^{\ell\times L}$ denote the spectrum and the spatial basis for $|\mathbf{X}'|_i^2$, respectively. *K* is the total number of rows and *L* is the total number of columns in matrix $\mathbf{Y}$, respectively. The visual explanation of the factorization is shown in Figure 3.8.

The matrix D can be compressed and reduced to its integral components, such that it contains a set of basis and H is an activation code matrix where its elements describe the amplitude of each basis at each space point. In NMF, the separation of defect and non-defect regions is directly considered because the characteristic signals from the two regions are totally different. In addition, the defect region displays a strong separation property. This means that NMF is suitable for extracting these characteristics, and has been proven to lead to better results. For the NMF algorithm, the definition of the observation matrix $|\mathbf{Y}'|^2$ has a unique decomposition, in that ambiguity is reduced to a permutation and scaling of columns in D and rows in H.

This uniqueness means that the sizing of and distinguishing between different types of defects can be improved by introducing sparsity constraints, and the basis D and H can be updated through a Euclidean distance cost function as $\min_{\mathbf{D},\mathbf{H}} \left\| |\mathbf{Y}'|^2 - \mathbf{DH} \right\|^2$ and other different cost functions or prior knowledge (where this can be obtained using simulations of different types of defects). The spectral basis for both defect and non-defect areas are obtained globally through the whole X-band frequency range in order to eliminate the interpolation issue of conventional spectral estimation methods such as manually selecting specific frequencies to analyse the defect.

3.3.2.2 Feature extraction using PCA

In this thesis, both magnitude $\mathbf{Y}'_M = |\mathbf{Y}'|$ and phase $\mathrm{Y_P}' = \mathrm{atan}\left(\frac{\mathrm{Im}(\mathrm{Y}')}{\mathrm{Re}(\mathrm{Y}')}\right)$ information about $\mathbf{Y}'$ are used to process and analyse in order to generate images for defect. As the linear sweep frequency technique is used during the testing, multiple operational frequencies have been applied. In order to enhance the resolution of defect imaging, principal component analysis is used. For these PCA results, the whole X-band frequency range (8.2 GHz to 12.4 GHz) is used to extract information about defects under thick insulation.

PCA is extensively used in feature extraction to reduce the dimensionality of the original data by a linear transformation. Moreover, PCA extracts dominant features from a set of multivariate data. The dominant features retain most of the information, both in the sense of the maximum variance of the features and in the sense of minimum reconstruction error. PCA is used to extract defect information from data on the rough insulation layer and the attenuation of insulation layer. The signal obtained contains three uncorrelated source signals: one comes from the surface of the insulation layer, one from the insulation layer and the third from the metal surface. Because the metal completely reflects the microwave signals, the other two signals are weaker than the third one. However, the received signal may be covered by the other two even with a relative small defect. PCA is used here to extract the defect signals from received signals.

By using PCA, $\mathbf{Y}'_P$ can be processed using the same way, $\mathbf{Y}'_M$ can be transformed into uncorrelated sources by means of a whitening matrix based on the eigenvalue decomposition (EVD) of the covariance matrix $E\left\{\mathbf{Y}'_M \mathbf{Y}'^{\mathbf{T}}_M\right\} = \mathbf{EDE^T}$, where $\mathbf{E}$ is eigenvectors obtained from the orthogonal matrix and $\mathbf{D} = \mathrm{diag}\left(\lambda_1, \ldots, \lambda_N\right)$ is the

eigenvalues for $\lambda_1 \geq \ldots \geq \lambda_N$. After using PCA to obtain uncorrelated sources, it is also possible to reduce the transformed output dimensionality, for example by choosing $N_s \leq N$, where there exists N_s number of uncorrelated sources with the maximally informative subspace of the input data $\mathbf{Y}'_M$. In this thesis, both raw data and PCA results are plotted.

3.4 Chapter Summary

In this chapter, research methodology with outlined research diagram is proposed, which includes: development of HF RFID-based sensing in conjunction with microwave NDT. Theoretical concerns and feature extraction for different levels of the investigation of data gained from HF RFID and microwave systems are discussed according to the challenges of the detection of corrosion and defects under insulation. The theoretical background as well as the operation of the proposed systems and processing is explained.

Based on the challenges summarised in Chapter 2, RFID-based sensing and microwave NDT are proposed to be investigated. Through the following experimental studies, the relationship between extracted features and corrosion and defects under insulation can be established. As the complexity of insulation increases, statistical analysis is selected for feature extraction. The relevant processing algorithms for analysis are explained, which includes PCA and NMF. Primary measurement results with the proposed systems are generated for different grades and progression of corrosion over different exposure times in the following chapter.

Chapter 4. Corrosion Characterisation with HF RFID sensing and Near-field Microwave NDT

In the previous chapter the theory behind HF RFID-based corrosion sensing and microwave NDT have been outlined. This section presents the results of several experimental studies investigating the detection capabilities of the RFID-based sensing system. High frequency passive RFID tags are attractive in diverse applications where good sensor performance is needed and volume is restricted. The first case study demonstrates the ability of HF RFID-based sensing systems to differentiate not just between corroded and non-corroded steel but also between four different grades of corrosion that are of importance to the paint coating industry.

The second case study is of the progression of corrosion detection using a set of naturally corroded S275 mild steel plates. S275 means that the minimum yield strength of this steel grade is about 275 N/mm². It is suitable for numerous general engineering and structural applications. The capabilities of RFID-based sensing in conjunction with microwave NDT to differentiate among corrosion with different exposure times have been investigated. In order to investigate the corrosion progression over different exposure times on mild steel, several experiments were carried out to determine the stage of corrosion reached under laboratory conditions at room temperature. The differences between these corrosion stages, with exposure times ranging from non-corrosion to 10 months, have been examined with the proposed methods and the results compared with those of standard laser profilometry and PEC methods.

4.1 Corrosion Grade Study

The first experimental study involving the first set of corrosion grade samples was an attempt to provide a proof of this concept. To explore the detection capabilities of the HF RFID-based sensing system, carefully designed samples were prepared by

International Paint®. These samples represent realistic surface conditions and corrosion levels to test whether or not the RFID sensor can differentiate between them. All of the samples used in this study are made from structural S275 steel, which is a low-carbon mild steel.

4.1.1 Samples Setup

The samples are grouped into four sets as shown in Table 4.1. The first set, called the corrosion grade samples, are designed to test the capability of the HF RFID-based sensing to reliably differentiate between non-corroded and corroded steel. Furthermore, these samples allow the system's ability to differentiate between four qualitative corrosion grade conditions, which are of importance to International Paint® and the protective coatings industry as a whole, to be tested.

Table 4.1 List of the samples along with average thickness and surface roughness.

Specimens	Preparation grade	Average thickness of plate (mm)	Average surface roughness (μm)
UC1	A / blasted (Sa2.5)	4.077	18.3
UC2	B / SP11	3.898	16.1
UC3	C / ST2	4.142	29.1
UC4	D / unprepared	4.429	56.7

Four 300 mm × 100 mm steel plates were prepared. Three (samples UC2 to UC4) of these plates were placed inside an environmental test chamber for 1 month to accelerate the build-up of corrosion. All of the samples were then surface treated. From Table 4.1, the UC1 plate was blasted. An abrasive agent was primarily used to make sure that

corrosion and contaminants were free from the surface prior to painting. Therefore, the UC1 plate had no corrosion, and the UC2 plate had been power-tooled until metal revealed. Hence, some corrosion still remained on the surface.

As can be seen from Table 4.1, the power-tooled UC2 is the thinnest plate in these four samples. And the power tooling also resulted in a smoother surface, as shown by the measured average surface roughness from laser profilometry. Next, the UC3 plate had been scraped away the loose surface corrosion. No significant visible pitting had been left in the rust layer. Finally, no surface preparation was applied to the UC4 sample which resulted in a significant rough surface with flaking rust and pitting. Photographs of these four samples are shown in Figure 4.1.

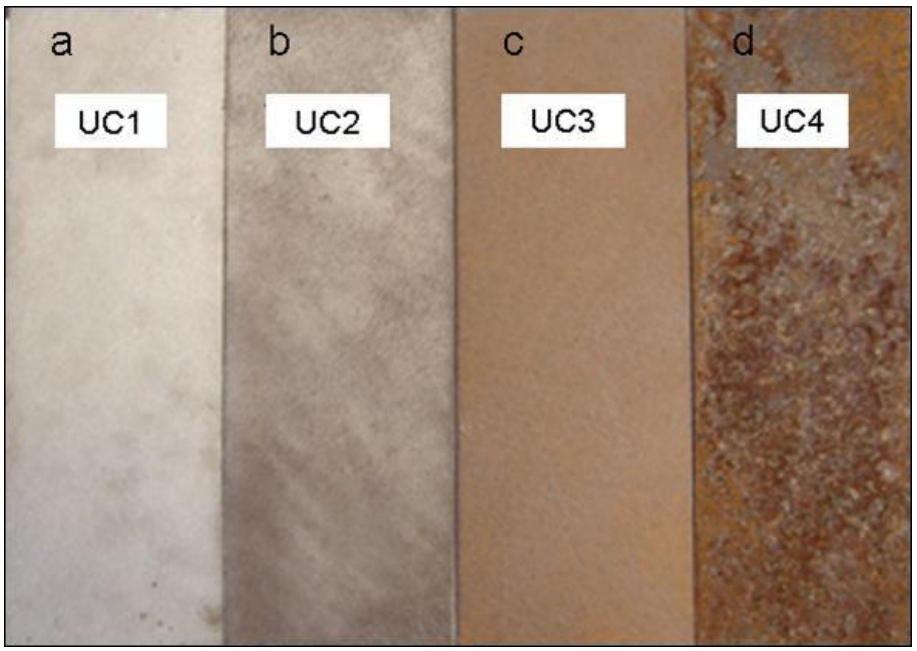

Figure 4.1 Photographs of four corrosion grade samples.

4.1.2 HF RFID-based Sensing System

The procedure for the determination of the physical characteristics of these corrosion samples is as follows. A HF passive RFID tag acts as an exciting coil that contains a current and induces an electromagnetic field. The resultant distribution of electromagnetic field is modified by this generated magnetic field in conjunction with

the surrounding material, which is obtained by a reader coil connected with a vector network analyser (VNA). For better comparison, the distance between the tag and reader is fixed.

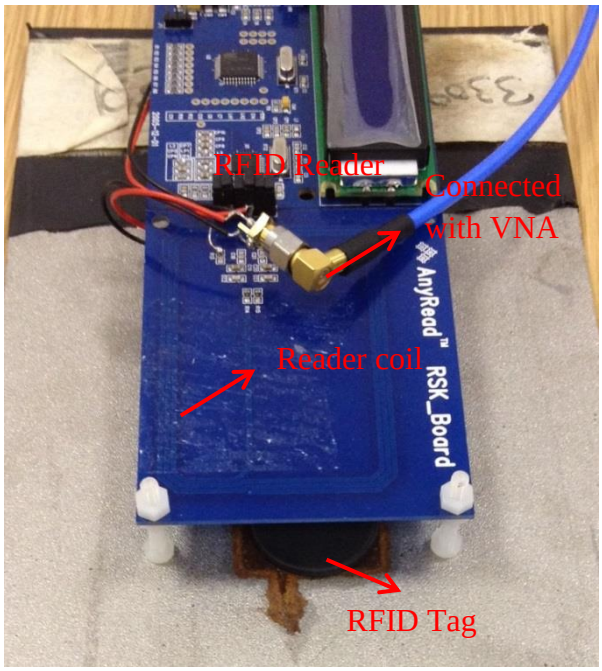

Figure 4.2 Photograph of a sample under testing with the Agilent E5071B VNA.

The reader coil is a flat spiral coil of a 100 mm diameter loop, 0.71 mm diameter copper wire with 13.56 MHz operational frequency. It consists of 3 turns of copper wires. Figure 4.2 shows a photograph of a corrosion sample under testing with the Agilent E5071B. RFID tags here are passive (Texas Instruments 13.56 MHz tags, as shown in Figure 4.3).

Figure 4.3 RFID transponders used for sensing.

The complete measuring system, as shown in Figure 4.2, mainly comprises a tag, a coaxial cable, a reader coil and the VNA. With the Agilent E5071B, the frequency characteristics of complex impedance parameters can be directly determined. As the HF RFID operational frequency is 13.56 MHz, the linear swept frequency range is set from 10 MHz to 20 MHz with the linear sweep frequency resolution at about 49 kHz. In order to compare these impedance features at different corrosion stages, samples are placed under the tag whose position is above the centre of the corrosion area.

The measurement procedure can be described as follows. The VNA generate electromagnetic waves and transmit to the coil through coaxial cables. When these waves arrive at the tag, it will generate an eddy current with the tag's coil; the VNA will measure the reflected signals which contain information on the electromagnetic properties of the environment in contact with the tag. The measurement results represent the tag and sample which are treated as a transmission line with an impedance mismatch. The measurement data are then extracted from the VNA and processed by custom built Matlab program developed for corrosion measurement purposes. This Matlab program allows the computation of the real and imaginary parts of the complex impedance as a function of frequency.

Four different types of transponders are used for corrosion testing, three of which conform are to ISO 14443 and one to ISO 15693. Both standards operate at the 13.56 MHz frequency. The major difference between these two types is that ISO 15693 requires much less power than ISO 14443 to charge its chip. As can be seen from Figure 4.3, tags 1, 2 and 3 are ISO 14443 and tag 4 is ISO 15693. Another difference is the size of the tags, as shown in Table 4.2 which shows their dimensions. These tags are chosen for this experiment because of their different sizes.

Table 4.2 Dimensions of the tags.

Tag No.	Thickness (mm)	Diameter/ length (mm)	Width (mm)
Tag 1	3	30.03	
Tag 2	3	50.09	
Tag 3	0.95	85.50	53.88
Tag 4	0.88	85.52	53.88

The experimental setup is shown in Figure 4.4. Two each of card-type and coil-type tags were placed at the centres of steel plates with the reader coil mechanically fixed using nylon bolts 20 mm directly above the tag. The tag-reader separation distance and alignment were carefully controlled in order to prevent any lift-off effects, as discussed previously. Five measurements per sample were taken.

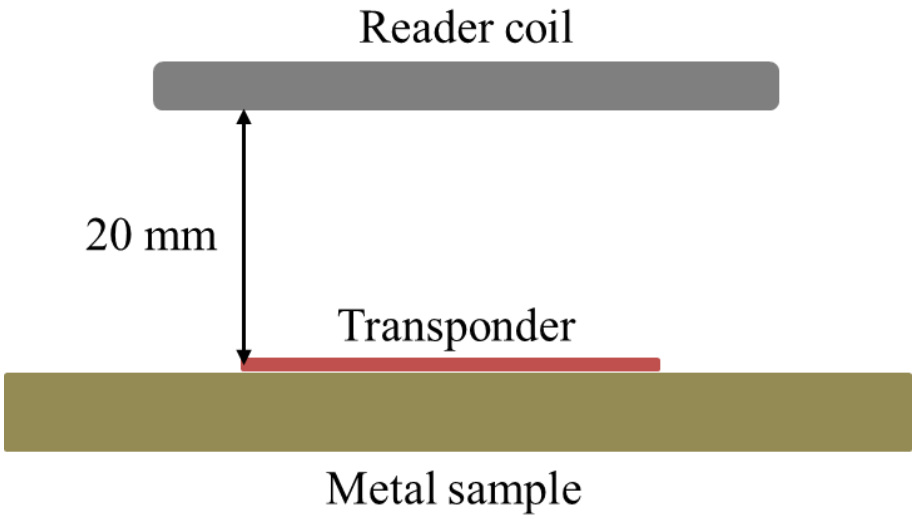

Figure 4.4 Experimental setup for four corrosion samples.

4.1.3 Results and Discussion

The average peak-to-peak amplitudes for each sample with four tags are plotted in

Figure 4.5. The first thing to note is that all of the samples are distinguishable with very small deviations from the mean of peak-to-peak amplitude. The trends seen in the results are in accordance with increasing corrosion grades from UC1 to UC4.

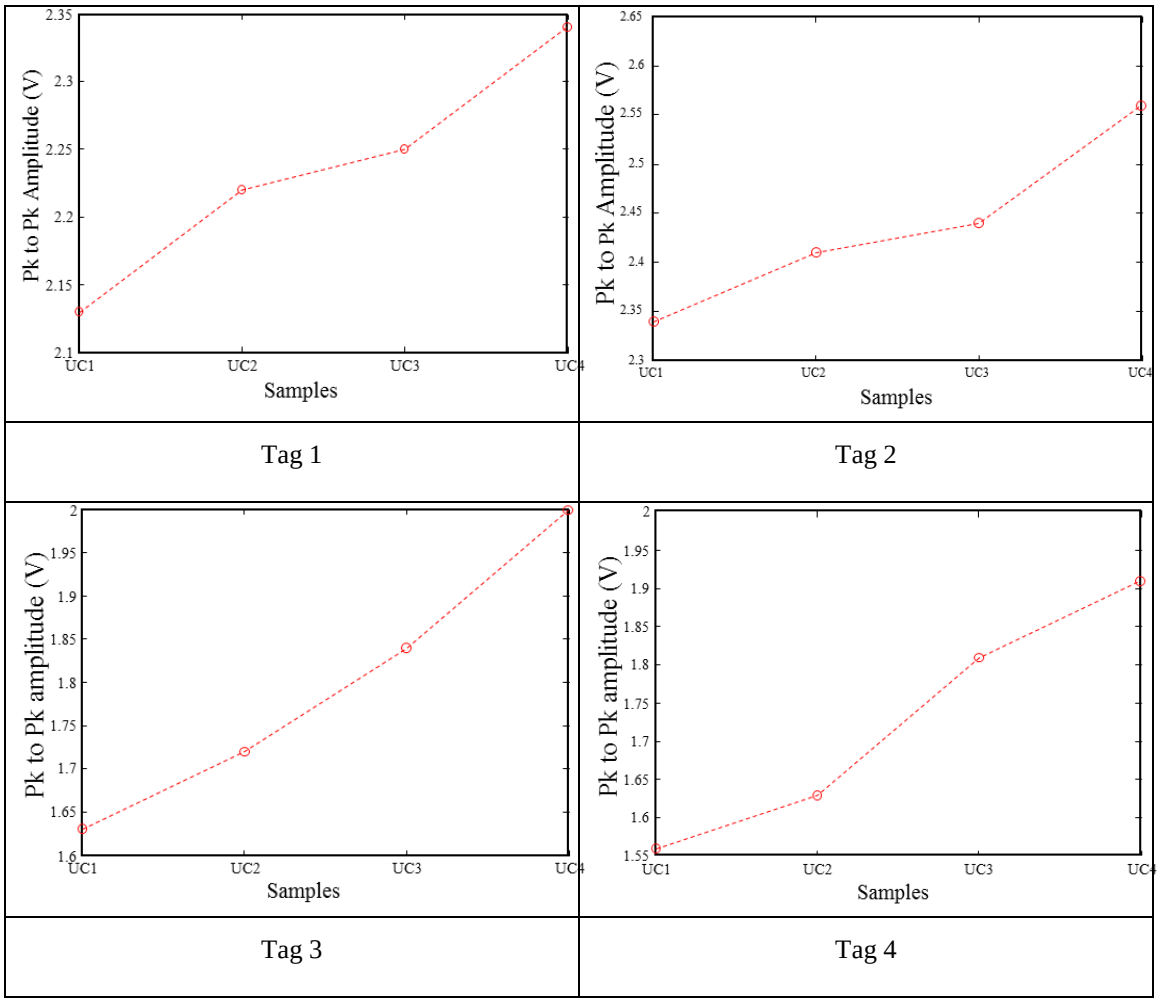

Figure 4.5 Average peak-to-peak amplitude for each grade sample with different tags.

Corrosion in samples UC2, UC3 and UC4 reduce the conductivity σ and magnetic permeability μ detected by the tags. With decreasing σ and μ, the tag's resonant frequency moves towards the resonant frequency of free space, resulting in the tag absorbing more power from the reader and hence an increase in amplitude. Increasing corrosion grade is expected to have an effect similar to decreasing conductivity, since a rough surface increases the path length of the eddy current. This can also explain why, with different tags, sample UC4 has the largest measured peak-to-peak amplitude. The main difference between these tags is the size of the coil, where a large coil diameter

will result in averaging of the rough surface and corrosion of the samples. Therefore, the peak-to-peak amplitude of smaller tags is higher than those of card-type tags.

4.2 Steel Corrosion Progression Study

The second set of samples, the corrosion progression samples, has been created to investigate the capabilities of the proposed systems to differentiate between different exposure times. These samples are created by exposing steel plates to outdoor conditions for different lengths of time, as shown in Figure 4.6. The result is natural corrosion, for giving a more realistic experimental scenario.

Figure 4.6 Sample preparation in outdoor environment.

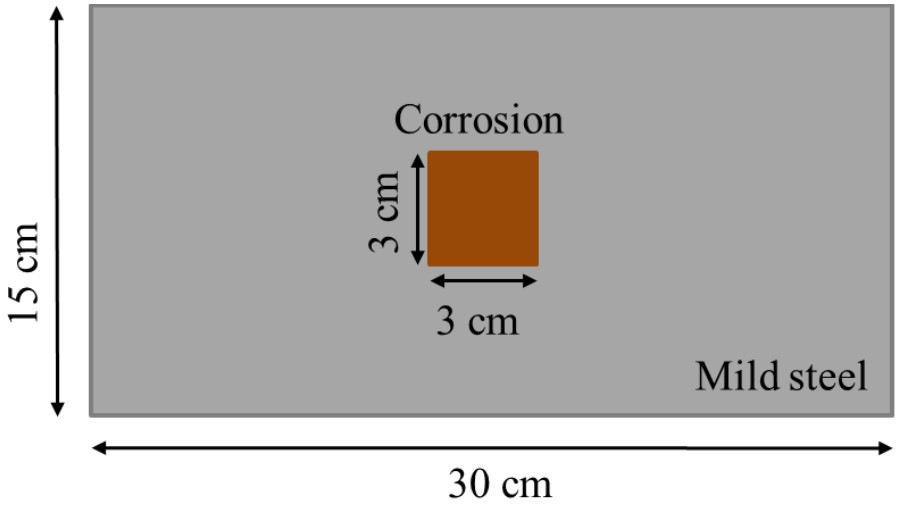

Figure 4.7 Dimension of samples and corrosion area.

Figure 4.8 Images of corrosion samples after exposure periods of (a) 1 month; (b) 3 months; (c) 6 months; (d) 10 months.

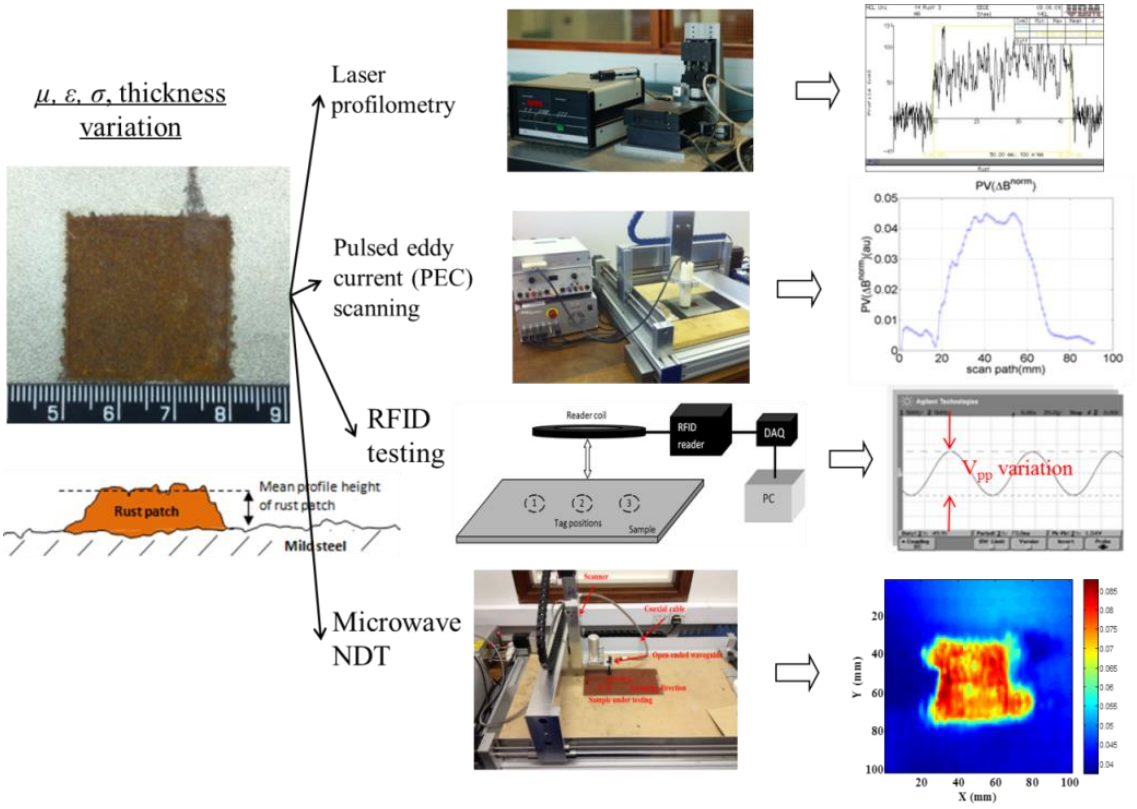

Figure 4.9 Four experimental systems used to denote corrosion ‘stage’.

In this study, the capabilities of RFID-based sensing and microwave NDT were examined to differentiate between the 4 naturally corroded samples. As illustrated in Figures 4.7 and 4.8, these samples were created by exposing a small 30 mm × 30 mm section of the plates to the atmosphere for 1, 3, 6 and 10 months. The differences between the stages of corrosion should be evaluated in order to understand the progression of corrosion, corrosion prevention, condition-based maintenance and life-time extension. Corrosion in these samples has taken place over a few months of

exposure as an indicator. In a scientific investigation, this should be explored in detail along with other standard methods. Therefore, to identify the differences between corrosion stages, four experiment systems have been adopted to evaluate corrosion 'stage', as shown in Figure 4.9.

Four different measurements link physical property variations in steel samples to evaluate present corrosion in the material:

- Laser profilometry – corrosion causes a change in the components of steel material to iron oxides leading to an increase or decrease in thickness of the sample for different exposure times.

- Pulsed eddy current – as corrosion induced iron oxides consists of both reversible and irreversible changes, the oxidation-mechanical effect leads to a decrease in conductivity and permeability of the material which indicates the corrosion progression of the steel sample.

- HF RFID sensing – corrosion in the area leading to variations in the physical properties of corrosion over time which denote the stages of corrosion.

- Microwave NDT – permittivity and geometrical discontinuities cause concentrations of microwave signals around them which can be measured using a waveguide.

The measurement of corrosion generated by these four phenomena can provide a detailed investigation for corrosion and defect characterisation.

4.2.1 Evaluation of Corrosion Progression using Laser Profilometry

S275 steel samples with uniform corrosion produced by atmospheric exposure were provided by International Paint®. Details of these samples used in experimental work

are shown in Figure 4.8. This set of samples provides corrosion occurring after different exposure times, which are known as corrosion stages. To evaluate the variance in the corrosion layer with different exposure time, these samples were then measured during this experiment.

Thickness of these corrosion samples is about 3 mm, with sample a exposed for 1 month, sample b for 3 months, sample c for 6 months and sample d for 10 months. Figure 4.8 shows photographs of typically corroded steel samples, showing that there is a slight increase in the thickness of the corroded area. As mentioned in the previous section, there are decreases in permittivity, permeability and electrical conductivity due to corrosion. Therefore, conductivity, permittivity, permeability, and thickness variations have to be taken into account in denoting the stages of corrosion.

As shown in Figure 4.10, the line scans with laser profilometer for different corrosion stages results in variations in corrosion layer thickness. The surface measurements of corrosion samples were scanned with a laser profilometer. It is developed by the German UBM. The lateral resolution of this machine is approximately 1 μm, which is depended on the size of the focused laser beam, and the resolution of Z-axis is about 0.01 μm. A length of 50 mm line was scanned for each sample. This standard method is used for the purpose of characterising the microstructure of the four samples employed in this study. The software provided by UBM was used to calculate several parameters.

As shown in Figure 4.10, a model of different corrosion stages resulting thickness variations in the corrosion layer is provided, and the thickness of corrosion layer d can be calculated by:

$$d = d_1 + d_2 \tag{4.1}$$

where d_1 is the height of corrosion and d_2 is the depth of corrosion.

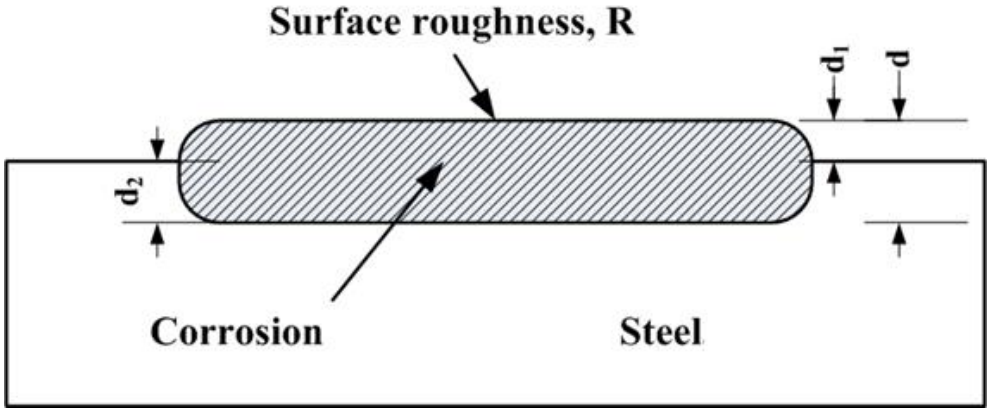

(a)

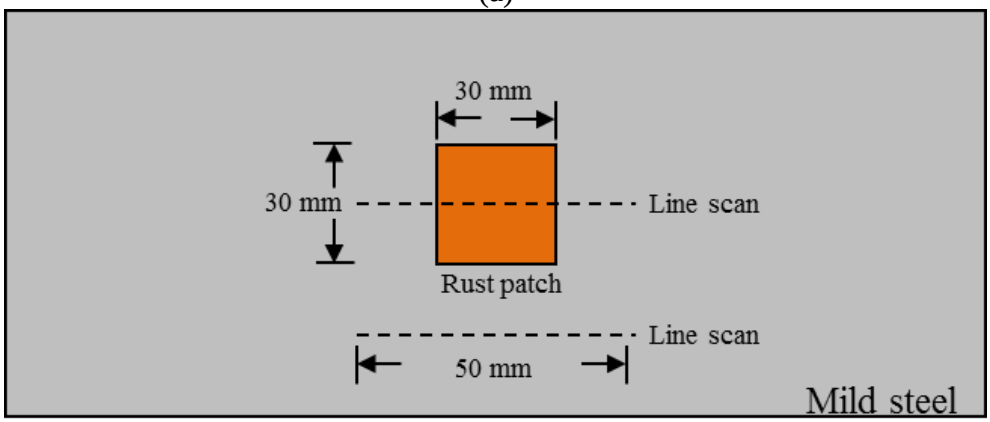

(b)

Figure 4.10 (a) Model of steel with corrosion layer; (b) line scanning position for corrosion measurement.

It is possible to conduct non-contact and non-destructive measurements of corrosion areas with the laser profilometry. The corrosion layer thickness of the different corrosion samples a, b, c and d is tested using the laser profilometer. The scanning length is 50 mm, which is larger than the corrosion area. Hence, the average height is employed to denote the variance of the corrosion layer thickness for each ‘stage’. The measurement results are shown in Figure 4.11.

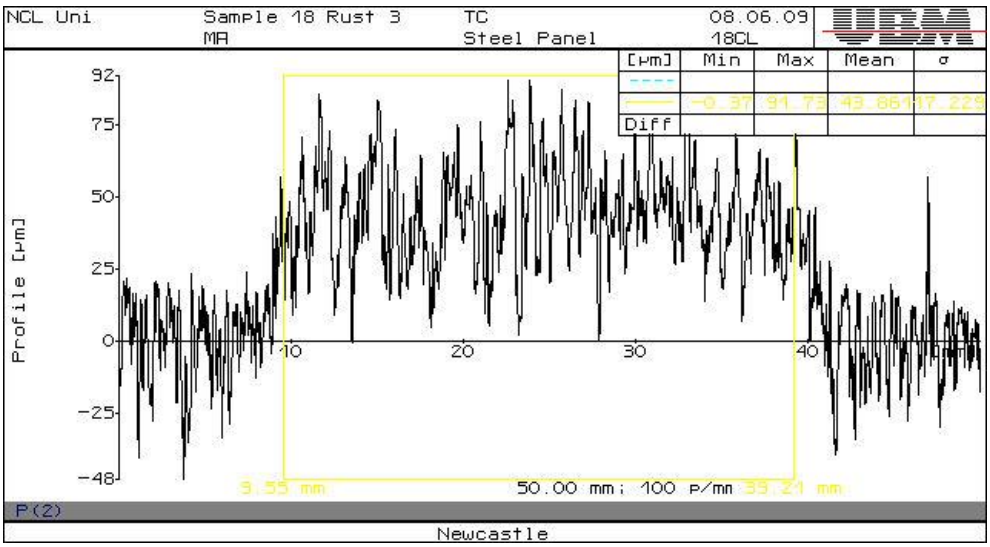

(a) 1 month

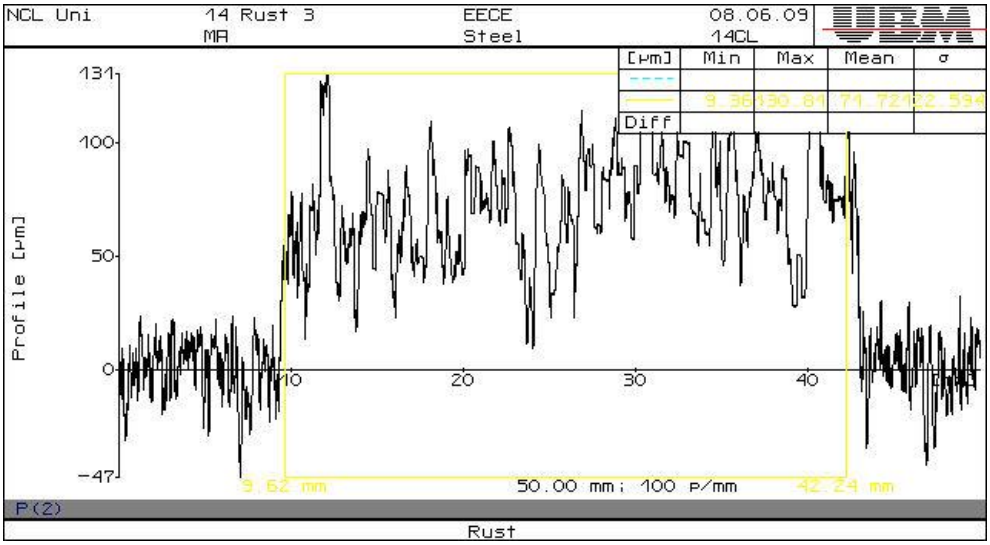

(b) 3 months

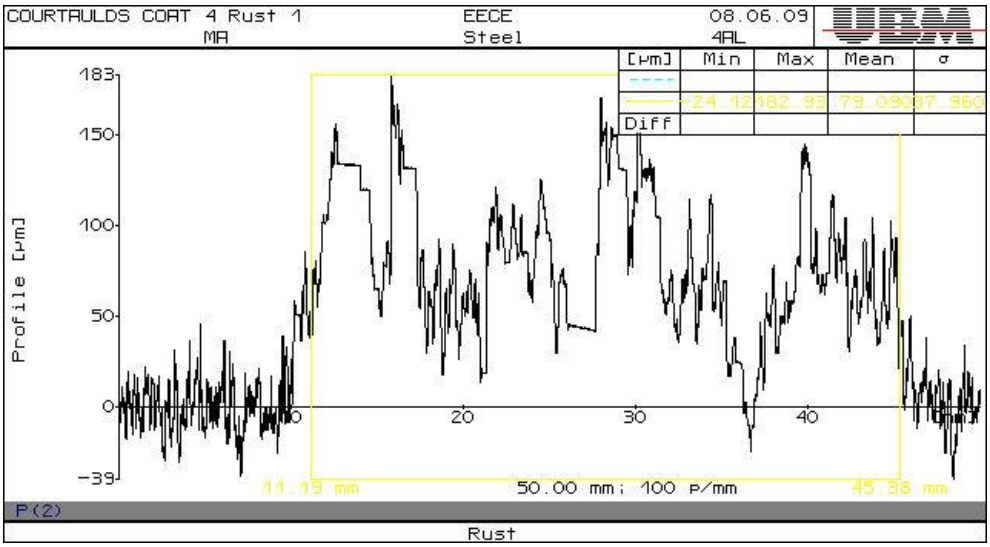

(c) 6 months

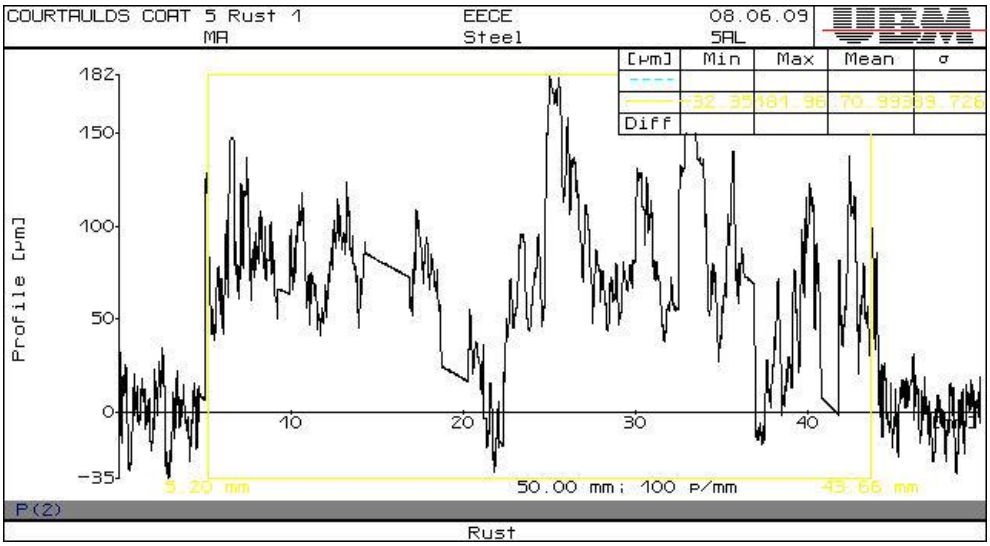

(d) 10 months

Figure 4.11 Surface profile of corrosion samples with different exposure times.

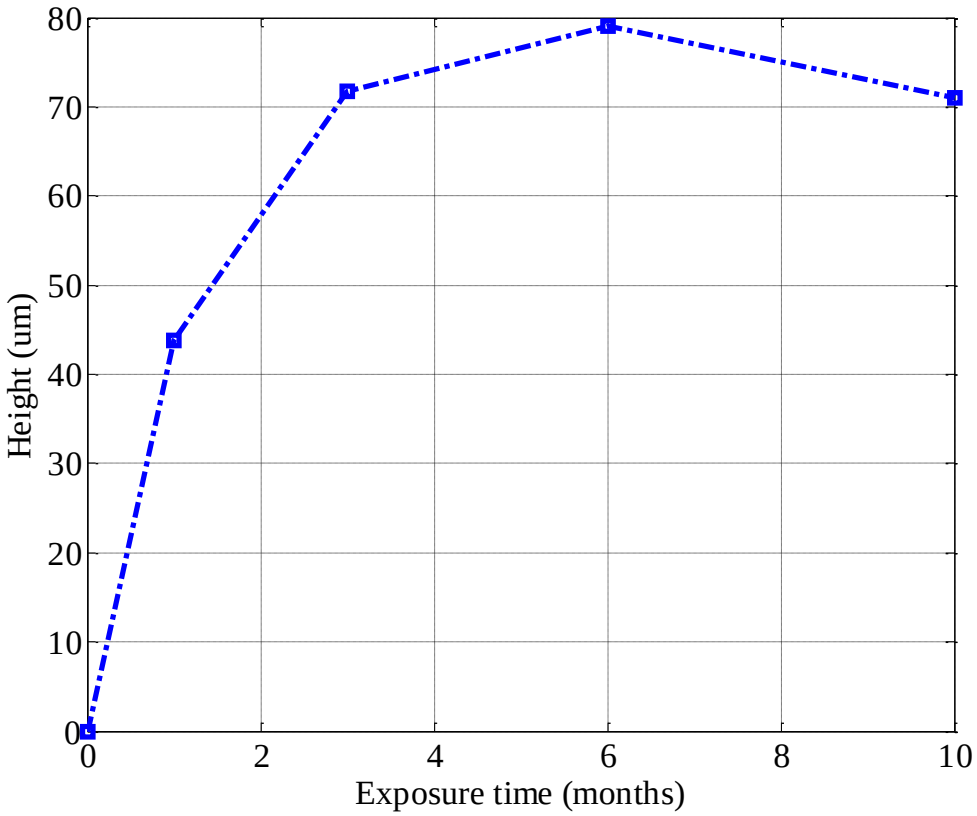

Figure 4.12 Measured corrosion height against exposure times using laser profilometry.

As shown in Figure 4.12, the average heights of corrosion for 1, 3, 6 and 10 months are 43.86 µm, 71.72 µm, 79.09 µm and 70.99 µm respectively. From 1 month to 6 months,

the height has a positive relationship with exposure time. However, the corrosion height after 10 months shows a decrease than compared to 6 months. This is due to the nature of corrosion [42].

As shown in Figure 4.13, after 6 months exposure corrosion is spreading rather than increasing in height. In addition, the rust layer of corrosion begins to loosen and flake off. It results in the height of the 10 months corrosion sample are lower than those of 3 and 6 months. Moreover, the corrosion layer begins to lose mass after 6 months.

Figure 4.13 Photographs of corrosion with exposure times of 1, 3, 6 and 10 months.

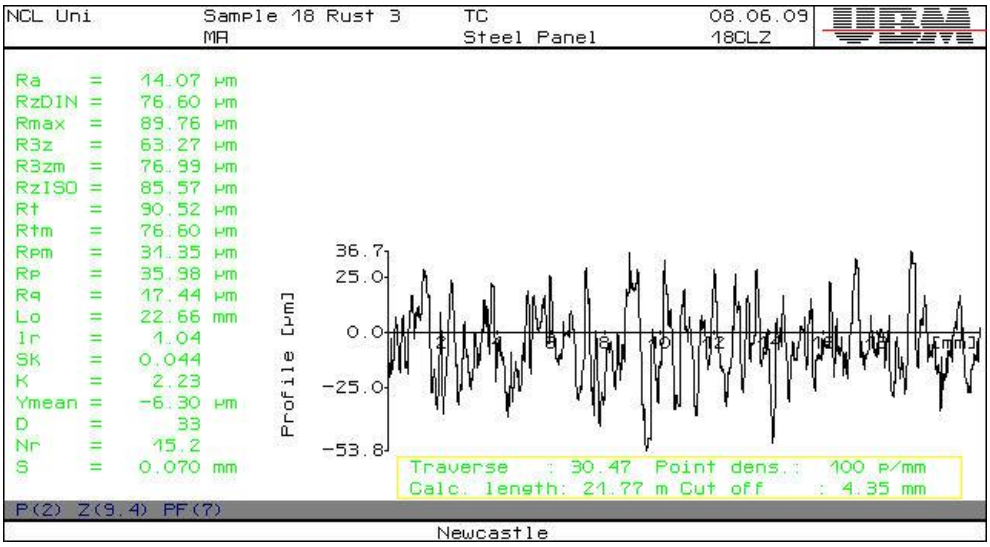

(a) 1 month

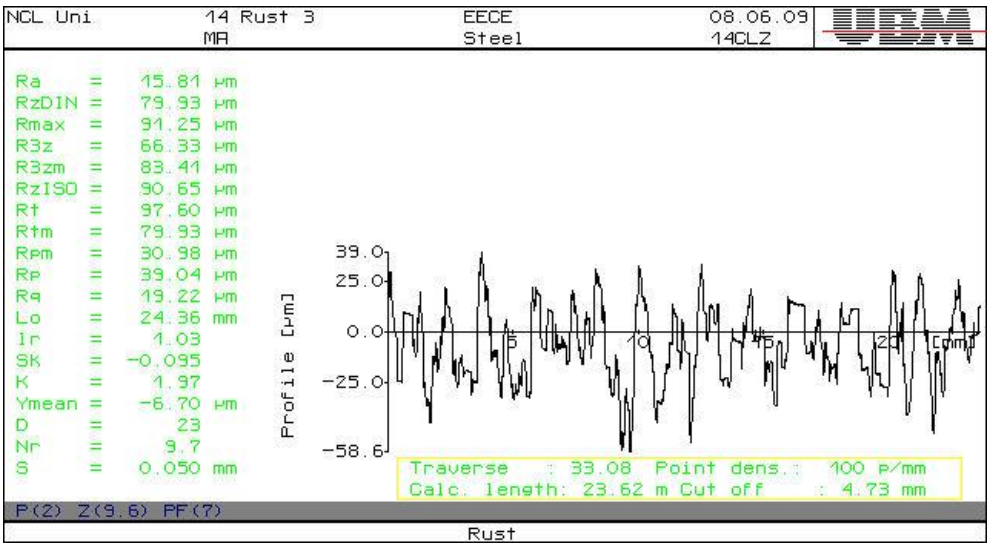

(b) 3 months

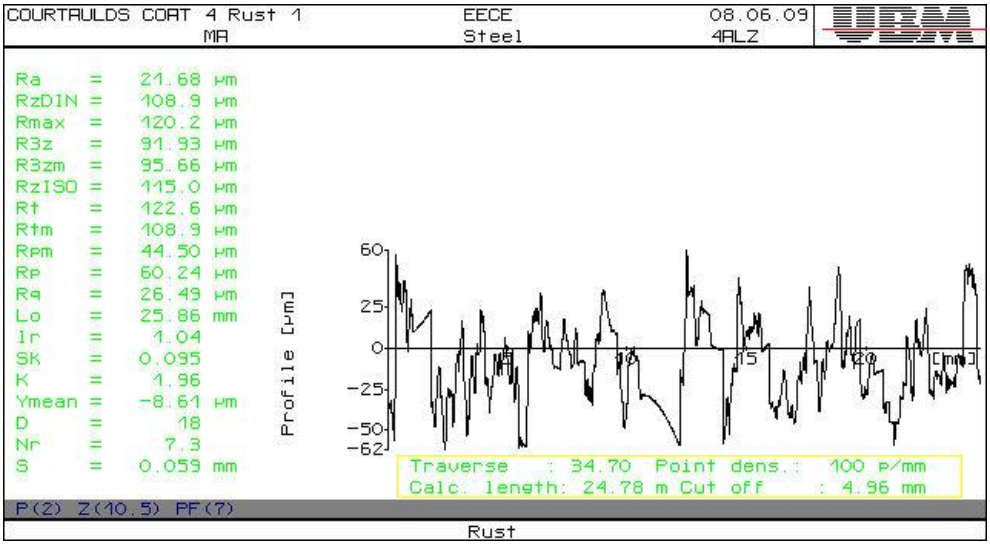

(c) 6 months

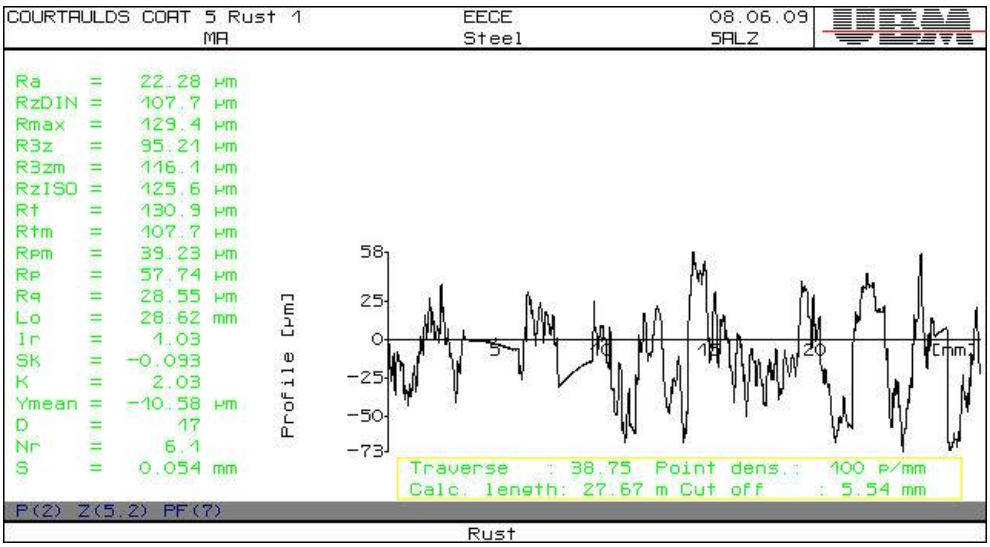

(d) 10 months

Figure 4.14 Surface profile of corrosion layers with different exposure times.

Figure 4.14 shows the surface profiles of corrosion on these samples. A roughness value can be calculated either on a profile or on a surface. Many different profile parameters can be used. Roughness average R_a and root mean square roughness R_q are more commonly used among these profile parameters and are calculated using equations 4.2 and 4.3:

$$R_a = \frac{1}{n}\sum_{i=1}^{n}|y_i| \tag{4.2}$$

$$R_q = \sqrt{\frac{1}{n}\sum_{i=1}^{n}y_i^2} \tag{4.3}$$

where y_i is the vertical distance from the mean line. For better comparison, values of R_a and R_q are also calculated for un-corroded steel plate. Figure 4.15 shows the surface profile of a non-corrosion area on a steel sample.

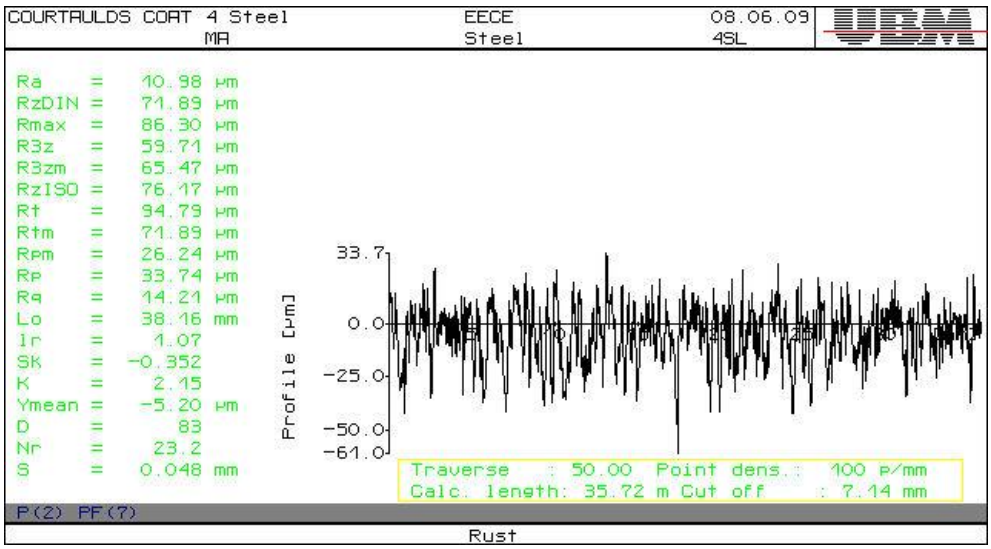

Figure 4.15 The surface profile of a non-corrosion area on the steel sample.

Figure 4.16 shows the variation in roughness average R_a and root mean square roughness R_q with exposure time. As exposure time increases from 0 to 10 months, the

thickness of the corrosion layer increases monotonously. The 0 month sample is of non-corroded steel; however, after 6 months, the thickness of the corrosion layer becomes stable.

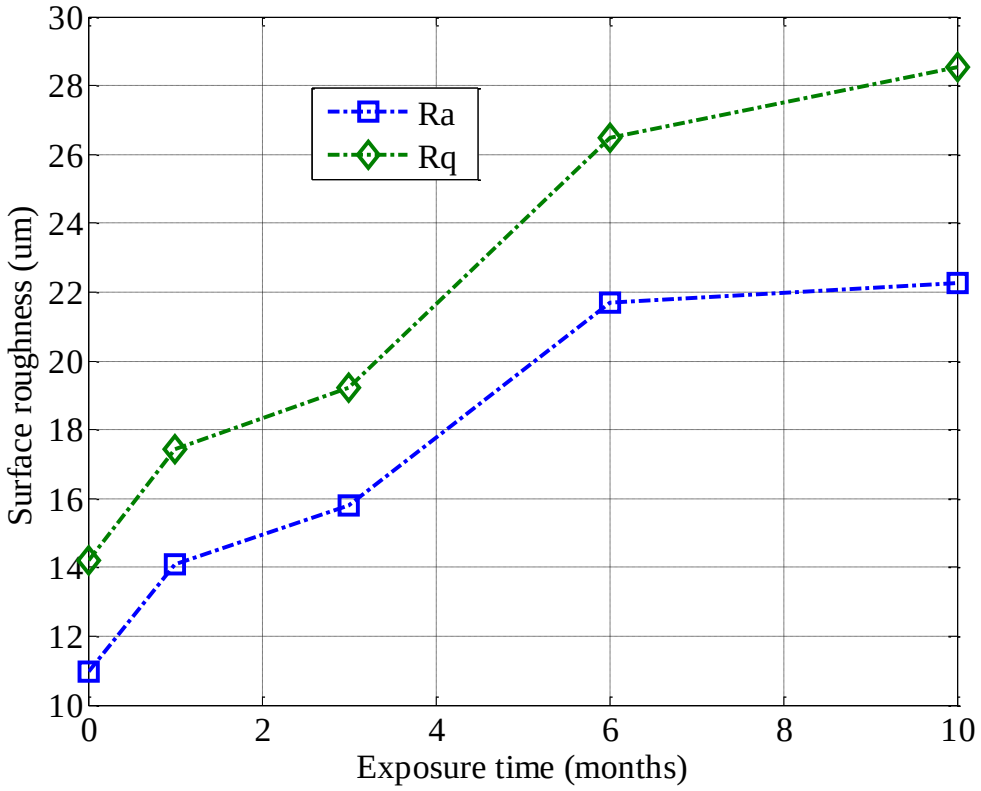

Figure 4.16 Variation in roughness average R_a and root mean square roughness R_q with exposure time.

In this subsection, steel samples with naturally uniform corrosion have been measured using a laser profilometer. The results of the measurements of corrosion stages show that as exposure time extends from 1 month to 6 months, the thickness of the corrosion layer increases. From 6 to 10 months, the thickness of the corrosion layer increases more slowly, and then even decreases due to the loss of metal.

However, this work has some limitations, due to the fact that the laser cannot penetrate into the corrosion layer. Therefore variation in corrosion depth with exposure time is not evaluated in detail. In the following section, variations in the conductivity and permeability of the corrosion layer are investigated using a pulsed eddy current (PEC).

4.2.2 Evaluation of Corrosion Progression using PEC

Progression of corrosion over different exposure times is complex. Conductivity and permeability in the corrosion region are lower than in pure metal without corrosion [162]. In this subsection, variations in conductivity and permeability in the actual corrosion layer are investigated using PEC responses as illustrated in Figure 4.17.

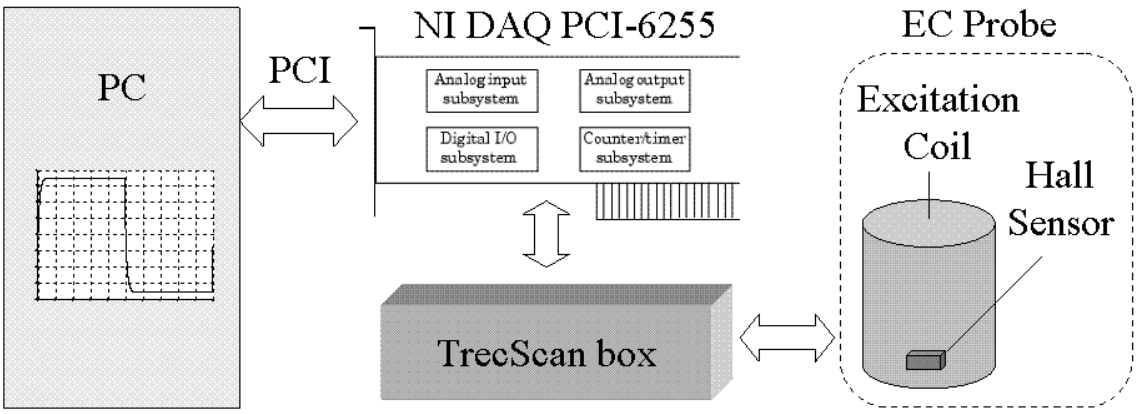

Figure 4.17 Pulsed eddy current acquisition scheme.

The proportions of the constituents of corrosion change over time, and this has a slight effect on composition [163]. The volume of corroded metal will decrease because iron oxides and hydroxides have a much less density than pure metal.

B_{REF} is obtained from non-corroded area and is the reference signal; B is the overall signal from the corroded region. Quantified differential signal (ΔB) is used to increase signal resolution as shown in the following equation:

$$\Delta B = B - B_{REF} \tag{4.4}$$

Due to the effect of magnetisation, variation in the maximal value of the magnetic field can be significant when measuring ferrous materials. Furthermore, the permeability is proportionally scaled to the magnitude of the PEC signal because of the ferromagnetic properties of the metal. Therefore, the maximal value of ΔB is used to characterise the variation in permeability, which is named *Max(ΔB)* in this study.

The differential normalised signal ΔB^{norm} is derived by normalising the total signal B and reference signal B_{REF} to their maximal value respectively as shown in the following equation:

$$\Delta B^{norm} = B/max(B) - B_{REF}/max(B_{REF}) \quad (4.5)$$

where $B/max(B)$ represents the normalised total signal and $B_{REF}/max(B_{REF})$ represents the normalised reference signal. $PV(\Delta B^{norm})$ is the peak value of the differential normalised signal.

Based on previous research in feature extraction and characterisation studies [42], it has demonstrated that $Max(\Delta B)$ can be used to characterise variance in permeability, the variance in conductivity can be characterised by $PV(\Delta B^{norm})$, and the sensitivity of both features exhibits high. In this subsection they are adopted to characterise corrosion layer, and monitor variations in the permeability and conductivity of the corrosion layer over different exposure times in particular.

Therefore, a PEC system was used to take measurements of four corrosion samples. 1 mm was the length of scan step and 30 mm × 30 mm was the size of the corrosion region on all of the localised corroded steel samples. 16 measurements were implemented under the same excitation for each corrosion region over different exposure times. The measured value is the average of these measurement results. Fitted line and measured values of $PV(\Delta B^{norm})$ for the steel corrosion samples are shown in Figure 4.18. The measured values of different corrosion stages are indicated by the red circles.

The blue solid line is fitted to the measured data for the different stages of corrosion in accordance with the following power function:

$$C = At^n \quad (4.6)$$

where C represents the PEC feature over exposure time t in months, A represents the PEC feature for the first month, and n represents a constant.

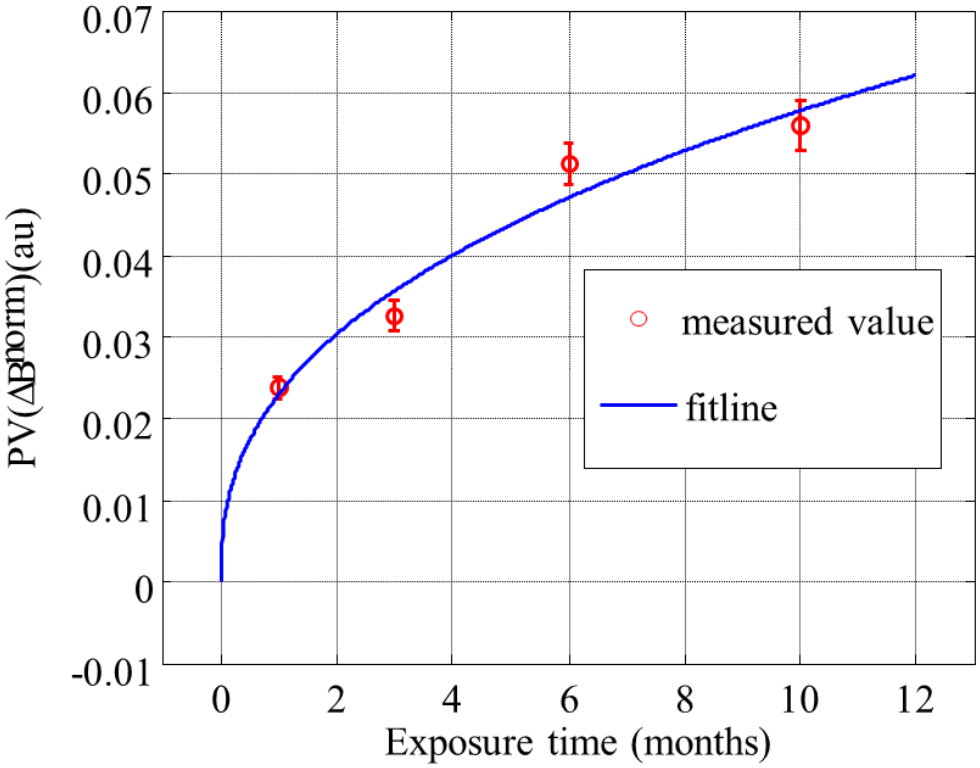

Figure 4.18 The fitted line and measured values of $PV(\Delta B^{norm})$ for different stages of corrosion.

As previous studies have mentioned, the power function is widely adopted to monitor the long-term corrosion [164-166]. As shown in Figure 4.18, it is concluded that the early stages (less than 1 year) of corrosion can also use the power function to monitor. The values of A and n for the fitted line are listed in Table 4.3. If the unit of t is changed from months to years, the power function then becomes:

$$C = A(12t_y)^n = 12^n A t_y^n = B t_y^n \tag{4.7}$$

where C represents the PEC feature after t, t_y represents the exposure time in years, and n is constant. $B = 12^n A$ represents the PEC feature of the first year. As shown in Table 4.3, the value of B is also listed. The exposure time of corrosion can be predicted

from the PEC features by using Equations 4.6 and 4.7. The value of $PV(\Delta B^{norm})$ for corrosion after 12 months exposure is predicted to be 0.0621.

Table 4.3 Fitted values of *A*, *n* and *B*.

Sample	Feature	*A*	*n*	*B*
Corrosion progression over different exposure time	$PV(\Delta B^{norm})$	0.0230	0.3989	0.0621
	Max(ΔB)	-0.2879	0.4695	-0.9209

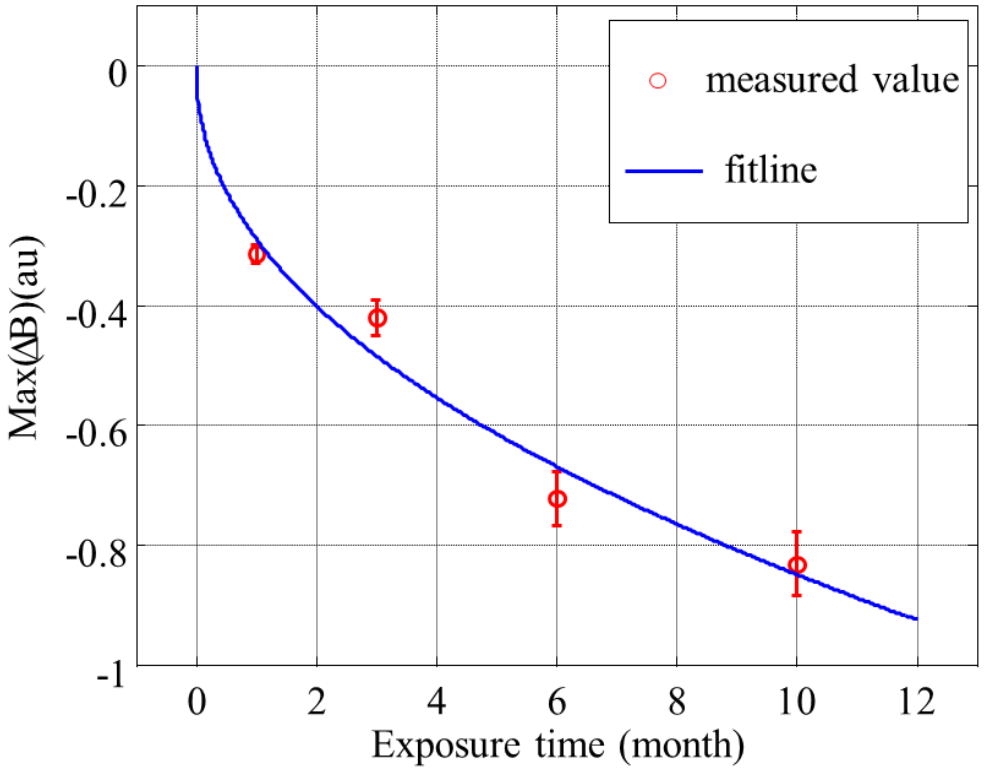

Figure 4.19 The fitted line and measured values of *Max(ΔB)* for different corrosion stages.

The fitted line and measured values of *Max(ΔB)* for steel corrosion samples are shown in Figure 4.19. The measured values for different corrosion stages are represented by the red circles, and the blue solid line is fitted to the data for these corrosion stages employing the power function. These fitted values of *A*, *n* and *B* for *Max(ΔB)* are provided in Table 4.3. Except for the fact that the fitted values of *A* and *B* are now

negative, the fitting line for *Max(ΔB)* data can also use the power function.

As illustrated in Figures 4.18 and 4.19, the measured values for the different corrosion stages are different. In Figure 4.18, there is a good agreement: $PV(\Delta B^{norm})$ is monotonically increasing over different exposure time *t*. Increasing $PV(\Delta B^{norm})$ means that the conductivity of the measured region is decreasing with corrosion progression [167]. In Figure 4.19, good agreement is also found: *Max(ΔB)* is decreasing over different exposure time *t*. Decreasing *Max(ΔB)* means that the permeability of the measured region decreases with corrosion progression. Over time, increasing thickness of corrosion region leads to the contribution of the PEC responses increasing; it will result in decreasing the permeability and conductivity of the corrosion region.

From these investigations, the progression of corrosion over time can be characterised in terms of thickness, conductivity and permeability. Taken together these results provide important insight into variations in the properties of the corrosion layer over time. These results indicate that there is an association between the properties of corrosion and exposure time, and the next section, therefore moves on to HF RFID-based sensing for monitoring corrosion over time.

4.2.3 Evaluation of Corrosion Progression using HF RFID

In this section, HF RFID-based sensing technique is developed. Several features are selected to investigate variations in the physical properties of corrosion over time, which allows the measurement of corrosion progression. These independent features are extracted from the real part and imaginary parts of measured complex impedance of a HF passive RFID-based sensor. The detection of corrosion under insulation is affected by the lift-off effect which is introduced by insulation layers. The reduction of lift-off effects will be studied in Chapter 5. A vector network analyser (VNA) is employed to obtain the complex impedance data. A wireless HF RFID sensing system for the

evaluation of corrosion is then developed for the monitoring of corrosion under insulation.

As mentioned in Chapter 3, the two parameters Z_p and Z_{pp} are chosen for further study. By simultaneously measuring these two parameters of the complex impedance from the RFID tag, the patterns of corrosion progression at different exposure times have been investigated.

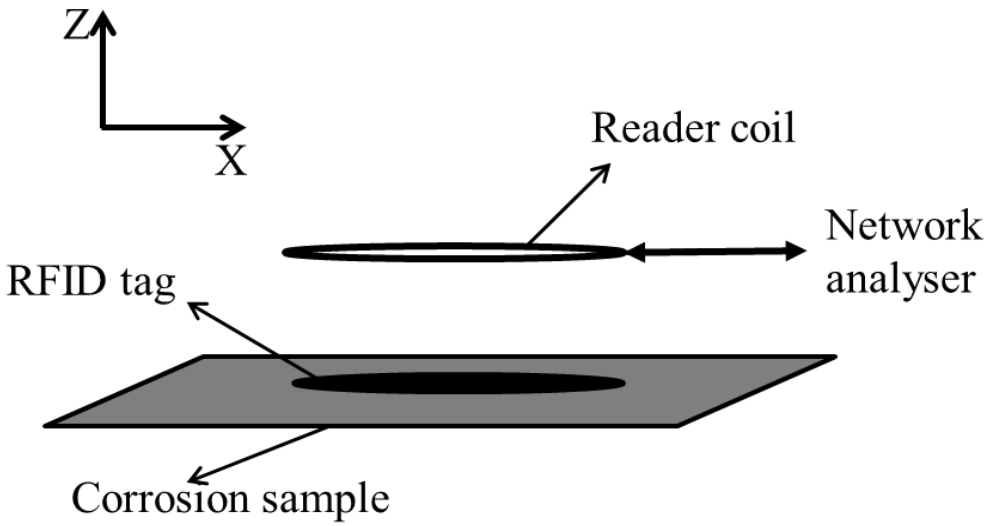

Figure 4.20 Schematic for the evaluation of the corrosion detection ability of the RFID system.

For reducing lift-off effects, a test system was assembled as shown in Figure 4.20. The distance between the RFID tag and reader coil is set at the same height to avoid the effects of lift-off. Corrosion samples with different exposure times from zero to 10 months are studied, and the reader coil is placed 10 mm above the tag. The RFID tag is placed on the centre of the sample, which is the area of corrosion.

The measurement procedure can be described as follows. VNA generates electromagnetic waves and transmit them to the reader coil through a coaxial cable. When these waves arrive at the tag, it will generate an eddy current with the tag's coil. Then, the VNA will measure the reflected signals which contain information about the electromagnetic properties of the environment in contact with the tag. The tag and

samples are treated as a transmission line with an impedance mismatch. The measurement data are then extracted from the VNA and processed by a custom-built Matlab program developed for corrosion measurement purposes. This Matlab program allows the computation of the real and imaginary parts of the complex impedance data as a function of frequency.

For better comparison, the distance between the tag and reader's coil is fixed at a height of around 10 mm. The overall relationships between the complex impedance, frequency and exposure time for all specimens are illustrated in Figure 4.21. It can be seen that the frequency-dependent complex impedance corresponds to different exposure times. Because the effects of capacitance and inductance vary with the frequency of the current passing through the wires, this makes the impedance vary with frequency.

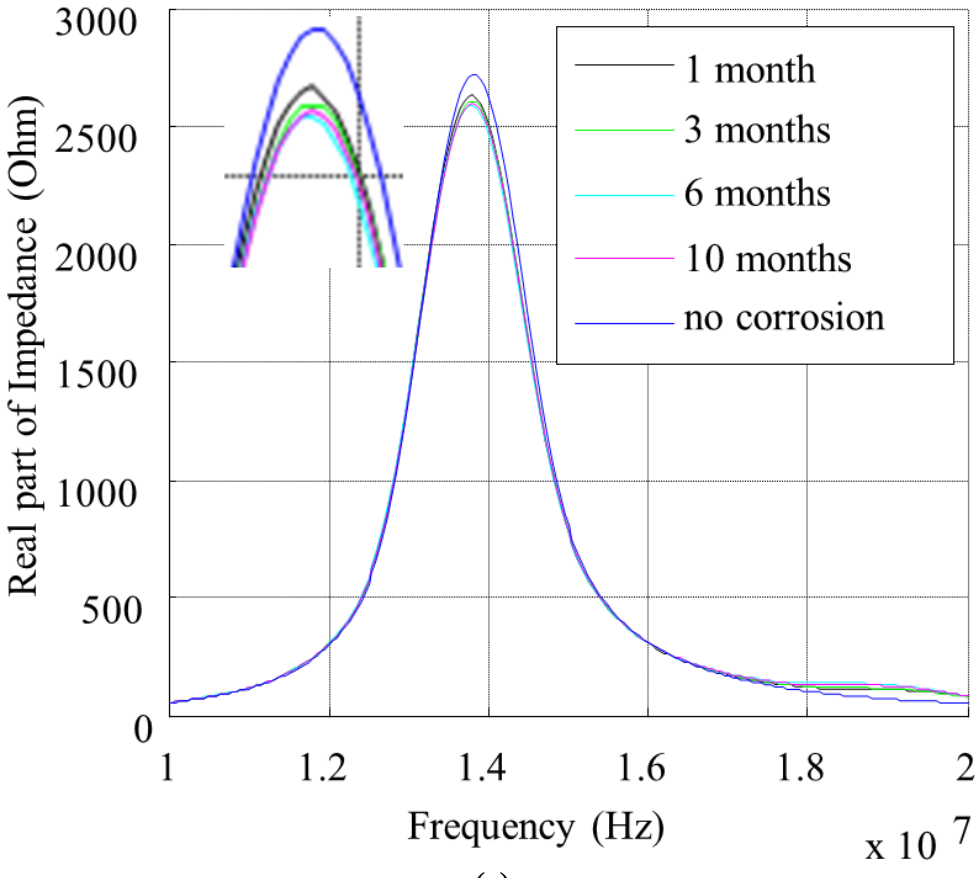

(a)

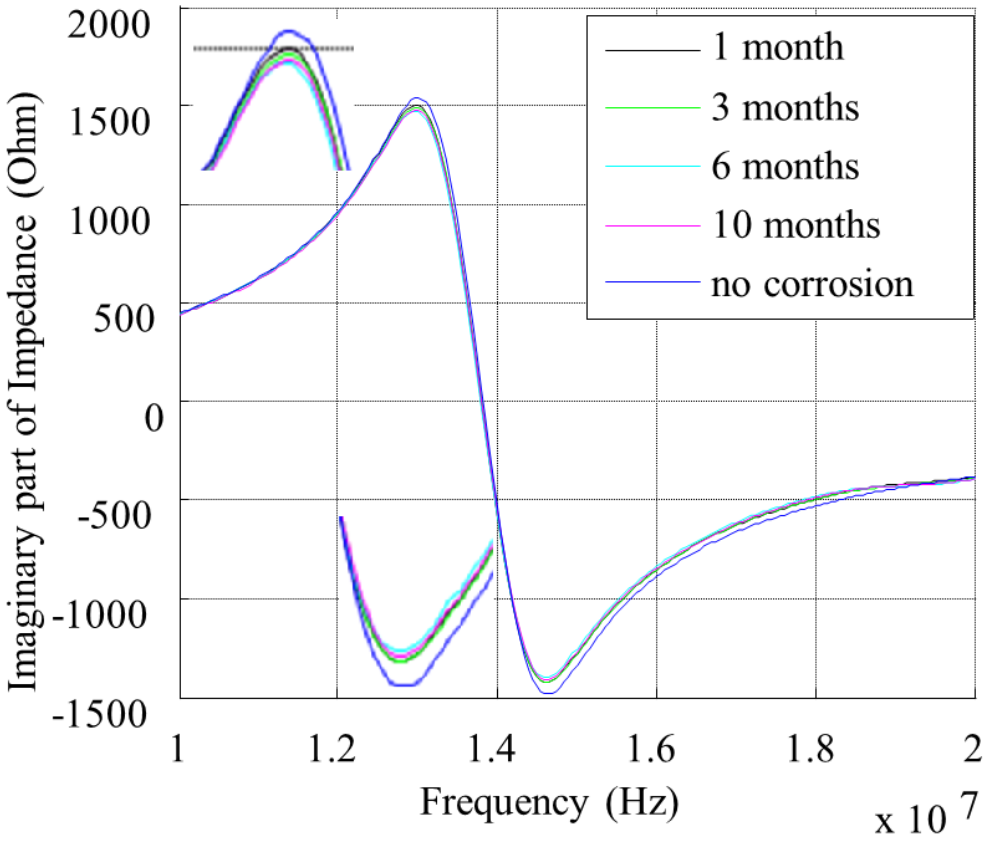

(b)

Figure 4.21 Real (a) and imaginary (b) parts of variations in complex impedance with frequency and exposure time.

Figure 4.21 shows that there is a trend of decreasing impedance with longer exposure time. As described in Chapter 3, RFID relies on magnetic fluxes between the coils of the reader and tag. In free space, these magnetic fluxes induced by the reader penetrate the tag's coil. When placed on metal, an eddy current is induced on the metal in the vicinity of the tag and a demagnetising field caused by this eddy current reduces the original magnetic field necessary for the transmission of energy and data. This reduction decreases the amount of power absorbed by the tag, and hence the reading distance is reduced. Therefore, the lift-off tolerance of RFID sensing is limited. Moreover, corrosion sensing relies on these eddy currents.

As corrosion develops on the metal, the increase in thickness and decreases in magnetic permeability and electrical conductivity will lead to increasing the penetrating magnetic flux towards the free space value. Therefore, with longer exposure times, the resonant

frequency moves towards the 13.56 MHz operational frequency. Exposure time seems to be a major factor in determining the complex impedance of these four steel corrosion specimens. The results indicate that variations in the physical properties of the corrosion layer over different exposure times can be detected by this proposed HF RFID-based sensing system. The dynamic multivariable responses Z_p and Z_{pp} for corrosion progression over time are plotted in Figures 4.22 and 4.23.

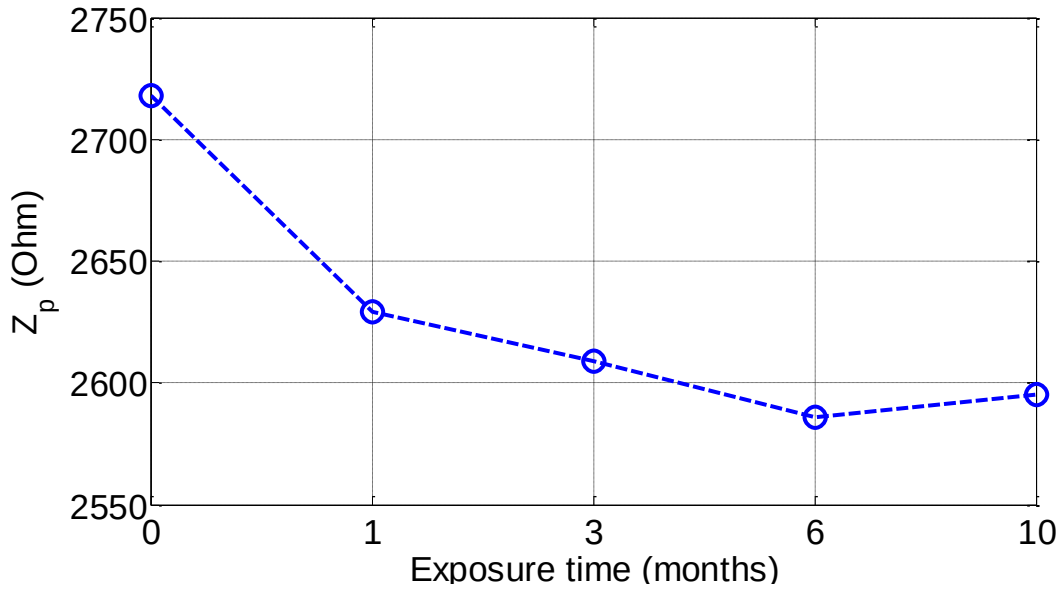

Figure 4.22 Corrosion progression over time monitored with the RFID tag.

The magnitude of resonant impedance Z_p decreases with exposure time and the same is true for Z_{pp}. The responses Z_p and Z_{pp} for different corrosion stages are generated against exposure time in Figures 4.22 and 4.23. The magnitude Z_p shows the biggest variation between non-corrosion and after corrosion 1 month. From 1 to 6 months, the magnitude of Z_p decreases monotonically from non-corrosion to 6-month corrosion. For the 10 months sample, the impedance is slightly smaller than that of 6 months. The peak-to-peak magnitude of the imaginary part Z_{pp} changes rapidly from non-corrosion to 6-month corrosion. Together these results provide the important insight that corrosion progression is not linear with respect to exposure time.

As both the real and imaginary parts of impedance change monotonically over the entire

range, there is a tendency for impedance to show its greatest change in the region of 1-6 months exposure. However, these parameters for the 10 months sample do not change monotonically, as expected. This is due to the nature of each corrosion stage. As can be seen in Figure 4.13, the corrosion area begins to spread out after 6 months exposure. In addition, the rust of corrosion layer becomes loose and easy to flake off. After 6 months, the loss of mass begins to occur, which results in the thickness of the metal decreasing. So both the real and imaginary parts of impedance responses after 10 months exposure are not monotonically changing.

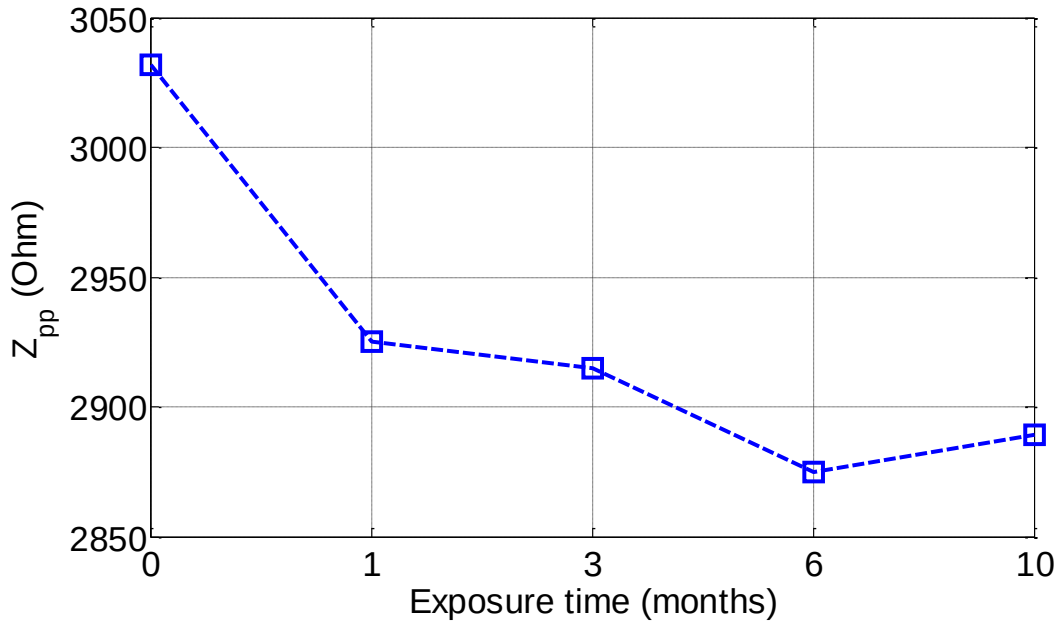

Figure 4.23 Corrosion progression monitoring with the RFID tag: peak-to-peak magnitudes of the imaginary part Z_{pp}.

These results from HF RFID-based sensing are in line with those of the previously mentioned NDE methods such as the pulsed eddy current and laser profilometry, as shown in Table 4.4. The correlation coefficient of surface roughness and impedance from the HF RFID results is 81.67% ± 2.1%. Moreover, the correlation coefficient of conductivity and impedance from RFID-based sensing is 94.70% ± 1.5%, while the correlation coefficient of permeability and impedance from RFID-based sensing is 90.39% ± 1.6%. These results suggest that HF RFID-based sensing is more sensitive to

variations in conductivity and permeability than to the thickness of the corrosion layer. In the following section, the variation of permittivity over corrosion progression is evaluated with microwave NDT.

Table 4.4 Measured values for various corrosion specimens.

Exposure time / Parameters	0 month	1 month	3 months	6 months	10 months
Surface Roughness (μm)	14.21	17.44	19.22	26.49	28.55
Conductivity $PV(\Delta B^{norm})$ (a.u.)	0	0.025	0.034	0.052	0.056
Permeability $Max(\Delta B)$ (a.u.)	0	-0.325	-0.422	-0.713	-0.85

4.2.4 Evaluation of Corrosion Progression using Near-field Microwave NDT

The ability of HF RFID-based sensing to evaluate corrosion has now been demonstrated. In this section, the permittivity of the corrosion layer over time is investigated using microwave NDT. The experimental setup is shown in Figure 4.24. An open-ended rectangular waveguide is mounted with an X-Y scanner. The probe is a standard WR-42 waveguide with the aperture dimensions of 10.668 mm × 4.318 mm. The sample under test is placed under the waveguide at a certain distance. This lift-off is set at 1.5 mm.

A vector network analyser (Agilent PNA E8363B) is employed here to provide the microwave signal source and to obtain frequency spectrum information from the reflected signal. The waveguide is connected to the vector network analyser through a coaxial cable. A control PC is used to control and acquire the measurement data from the vector network analyser through an IEEE-488 general purpose interface bus (GPIB).

The X-Y scanner is controlled by a controller connected to the parallel port of the control PC. A Matlab program is designed and used to control the vector network

analyser and X-Y scanner.

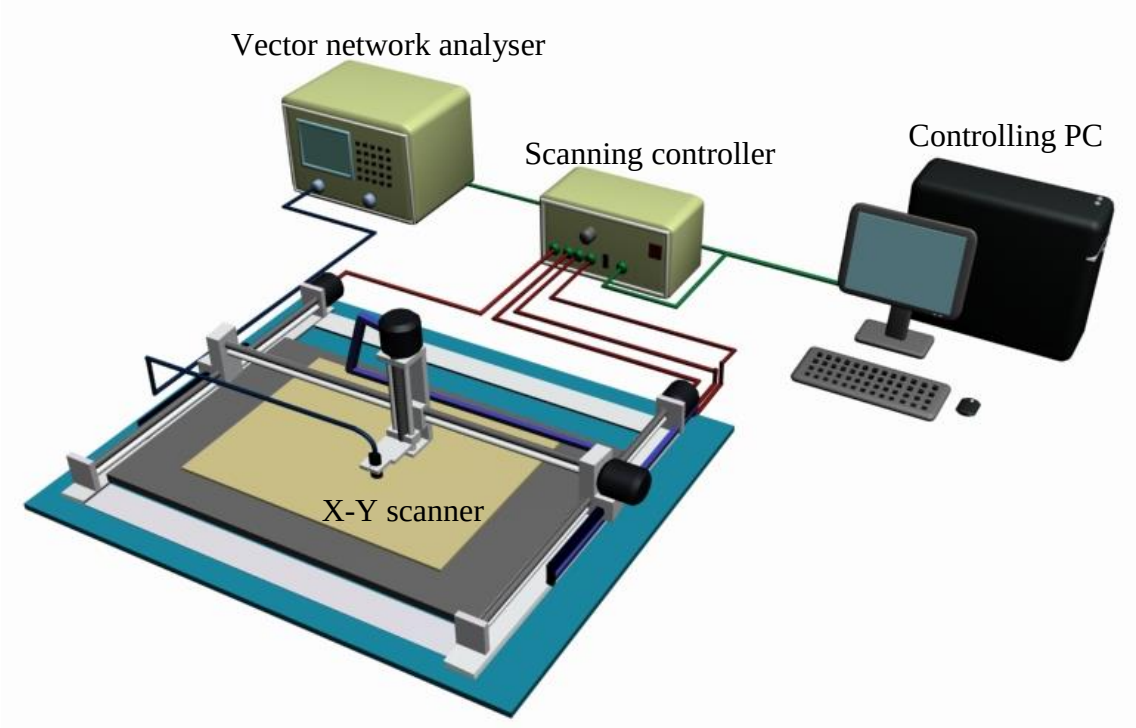

Figure 4.24 Experiment setup of open-ended waveguide-based microwave NDT.

During measurement, the frequency range is set from 18 GHz to 26.5 GHz. A linear sweep is applied over this frequency range with a frequency resolution of about 0.04 GHz with 201 linear swept points. The reflected frequency spectrum is obtained by using the linear sweep frequency technology with the vector network analyser.

To reduce the influence of long leads, Agilent E-Cal unit is used before measurement to calibrate the waveguide system. The standards of accurate factory calibrations are transferred from E-Cal modules to the network analyser. A precision calibration technique is used by Agilent to characterise these standards which have similar accuracy to TRL (Thru, Reflect, Line) calibration. The TRL is preferred by the NIST (National Institute of Standards and Technology). E-Cal uses the data from each calibration module's unique calibration to calculate the error terms for the network analyser.

Each stage of corrosion represents the progress of the chemical reaction according to

which a metal deteriorates in a specific environment over time. Its characteristics include the properties of the corrosion layer and variations in its thickness. The use of microwave NDT utilizing an open-ended rectangular waveguide has been adopted to measure minute thickness variations in laminate structures, it has presented a great potential, especially backing with a conducting plate [168].

Corrosion in steel is a general term for the production of a series of iron oxides (haematite α-Fe_2O_3, magnetite Fe_3O_4 and maghemite γ-Fe_2O_3), and hydroxides (ferrous hydroxide $Fe(OH)_2$, ferric hydroxide $Fe(OH)_3$, goethite α-FeOOH). These iron oxides and iron hydroxides have different permittivity properties. The relative permittivity of material can be defined as:

$$\varepsilon_r(\omega) = \varepsilon_r^{'}(\omega) - j\varepsilon_r^{''}(\omega) \tag{4.8}$$

where $\varepsilon_r^{'}(\omega)$ represents the stored energy within the material, and $\varepsilon_r^{''}(\omega)$ describes the loss of energy in the material. For example, values of measured average permittivity for various types and levels of corrosion are given by Qaddoumi [168, 169].

Table 4.5 Measured average values of permittivity for various types of corrosion.

Specimen	$\varepsilon_r^{'}(\omega)$	$\varepsilon_r^{''}(\omega)$
Black rust	12.58	2.36
Hydrated black rust	11.28	2.05
Red rust	8.42	1.03
Salt rust	5.33	0.53
Fe_2O_3 powder	3.22	0.04

As can be seen in Table 4.5, the average measured values of permittivity for various types of corrosion have been determined. With further reaction between iron and oxygen, there is an increase in the permittivity of the corrosion layer. For different corrosion stages, the constituents of the corrosion layer vary over time. Slight variations in the dielectric properties of the materials of the corrosion layer can easily be detected using microwave NDT employing a group of optimal parameters which includes the minimum lift-off and a higher operational frequency.

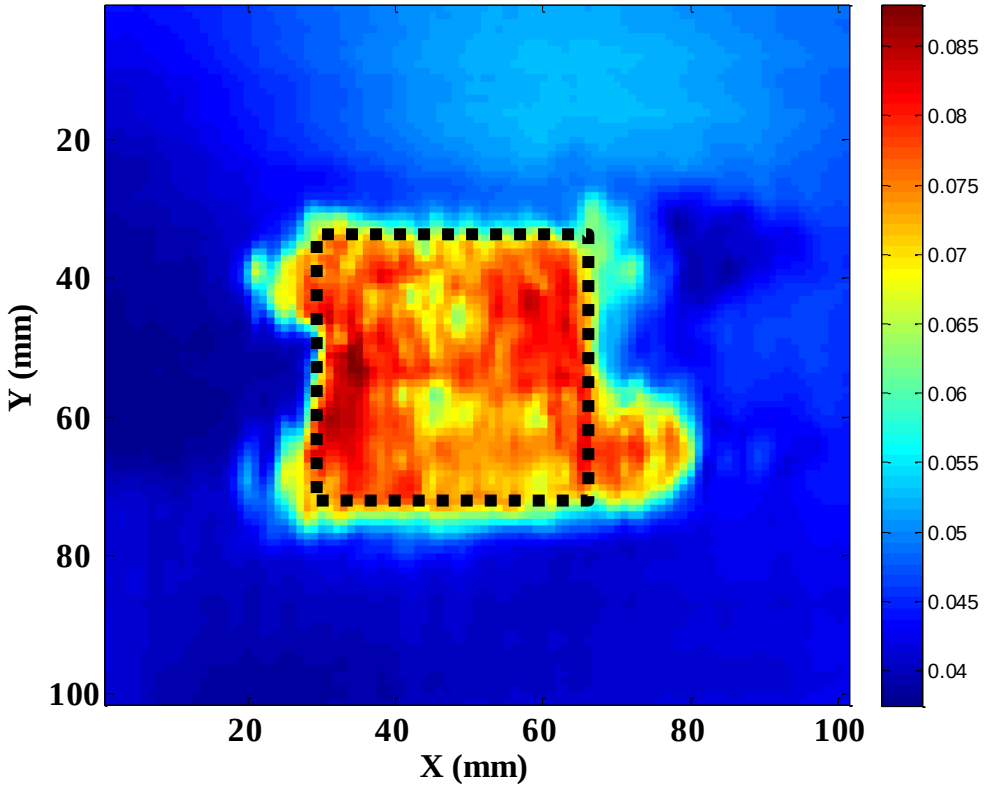

Figure 4.25 Image of steel specimen using microwave NDT after 10 months of corrosion.

Figure 4.25 shows experimentally obtained images of the steel specimen after 10 months corrosion using the magnitude of the reflection coefficient. The intensity (as shown in the colour bar) in the image is proportional to the measured magnitude as a function of scanning position. The corroded area is visible in the centre of the image (as highlighted by dot line). In order to better identify the progression of corrosion over time, the average of intensity of the corrosion area is used as the measured value. The

variations in permittivity can be characterised. In this section, these measured values are used for characterising steel corrosion, in particular to evaluate corrosion over exposure time.

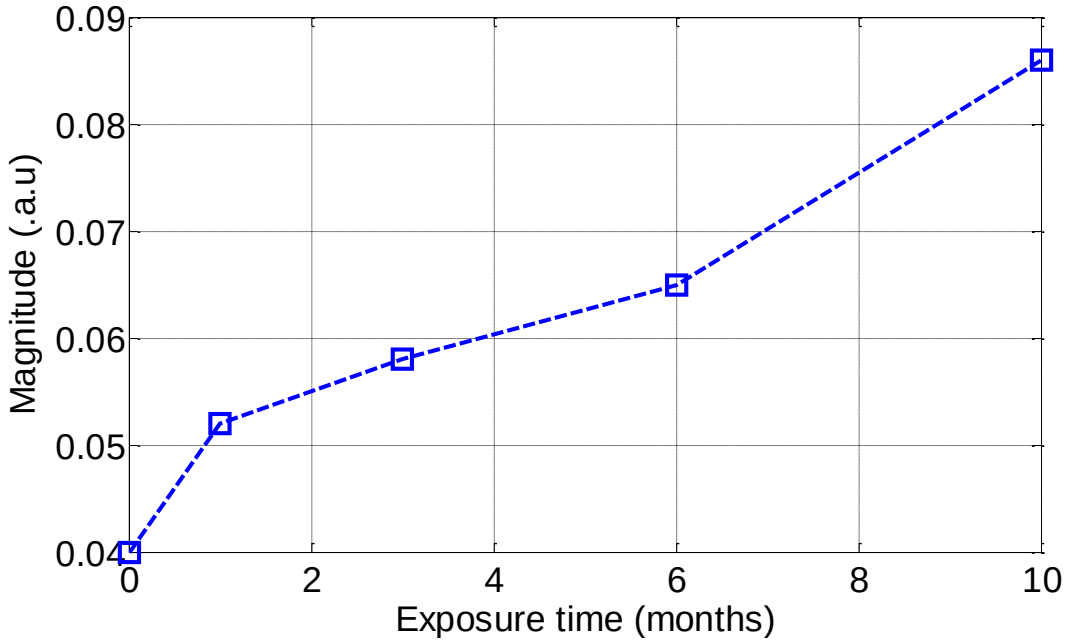

Figure 4.26 The measured values of magnitude for different corrosion stages.

As illustrated in Figure 4.26, the measured values for different corrosion stages increase monotonically with time. There is a good agreement with the results for the permittivity of the corrosion layer: magnitude shows a monotonic relationship with exposure time *t*. The increase in intensity of magnitude means that the average dielectric property of permittivity of the detected area increases. The correlation coefficient of magnitude and permittivity is 92.56% ± 2%. In summary, these results suggest that there is an association between permittivity and corrosion progression over time.

4.3 Chapter Summary

In this chapter, an approach adopting commercially available passive 13.56 MHz RFID tags for corrosion detection and corrosion stage classification has been investigated. The HF RFID can be used with peak-to-peak amplitude for general corrosion grade detection in mild steel. Several types of tags have been employed during case studies.

The amplitude responses are shown to be in line with corrosion grade conditions regardless of what shape of tag is used. The measurement results support the idea that HF RFID system can be used for classifying general corrosion grade.

Laser profilometry and PEC have been employed to study the corrosion progression over time to determine variations in the physical properties of the corrosion layer over time. The laser profilometry is sensitive to variations in corrosion thickness, while the PEC is sensitive to variations in conductivity and permeability of the corrosion layer. During case studies, changes in thickness, conductivity and permeability of the corrosion layer have been investigated for different stages of corrosion. Complex impedance is measured in mild steel samples by RFID-based sensing. RFID tag, reader and VNA are employed to study for corrosion progression over time. Employing the complex impedance feature, HF RFID can be used to evaluate the corrosion stages of steel samples. Moreover, the measured HF RFID results have correlation coefficients of over 90% with variations in conductivity and permeability of the corrosion layer.

Nevertheless, HF RFID is limited in terms of the sensing area and lift-off effects. Microwave NDT has been applied to determine the corrosion stage from larger areas under thick insulation. The microwave results give a correlation coefficient of 92.56% ± 2% with permittivity. From the case study, it has also been found that measurements of thickness, conductivity, permeability and permittivity can be adopted to identify the stages of corrosion over different exposure times.

Corrosion progression characterisation based on robust feature optimisation has been presented, and these results show that:

- The thickness, permeability and conductivity of the corrosion layer for the early corrosion stage ($t < 1$ year) are different. These features can be used to separate corrosion stages.

- Measurement of complex impedance by HF RFID based sensing can be used to detect corrosion at different stages.

- The reflection coefficient of the microwave signal can be used to detect the corrosion progression.

- Based on the variations found in thickness, conductivity, permeability and permittivity of the corrosion layer over time, the stage of steel corrosion can be identified.

One limitation of this study is that variations in lift-off are controlled. The following chapter presents further investigation to reduce the lift-off effects using RFID-based sensing and microwave NDT.

Chapter 5. Reductions of Lift-off Effects using PCA and NMF

In the previous chapter, the potential of an RFID and microwave system for corrosion detection has been experimentally demonstrated. However, in order to achieve this, a specific lift-off must be maintained for all measurements in real-world application. The applicability of these methods is limited since lift-off cannot always be kept constant in practical application. Changes in the RFID tag due to corrosion can be completely masked by even small changes in lift-off. Therefore, reducing the effect of lift-off is vital to the wider acceptance of the proposed systems.

In this chapter the RFID system is used with the principal component analysis to extract a custom feature which can compensate for the lift-off effect, allowing corrosion to be detected independently of reader coil position. To evaluate the proposed technique, different values of lift-off at different stages of corrosion are investigated. Secondly, microwave NDT using NMF based on a spatial-frequency feature extraction algorithm is employed for defect detection at large values of lift-off. This algorithm has the unique property of scale-invariance, which enables the extraction of spatial-frequency features that are characterized by large dynamic ranges of energy. To evaluate the proposed technique, four types of defects at different depths from 2 mm to 8 mm in an aluminium plate and one small defect of 0.45 mm in width and at 0.43 mm depth on a steel sample are examined.

5.1 Reduction of Lift-off Effects with PCA

As mentioned in the previous chapter, different values of lift-off lead to changes in mutual inductance coupling M. As a result, the measured impedance spectra $Z_M(f)$ will change. This will cause false alarms, as this change is caused by lift-off rather than corrosion. To reduce the influence of lift-off, the proposed RFID-based corrosion sensing needs lift-off independent features in order to correctly evaluate stages of

corrosion. This investigation demonstrates how to reduce the lift-off effects with PCA.

PCA is adopted here to obtain the maximum variability within the measured data. PCA is one of multivariate data analysis tools which transforms waveform data into uncorrelated eigenvector components corresponding to maximum variability while eliminating collinearity within the data [155]. The use of PCA reduces the number of variables considerably while still retaining much of the information in the original dataset. The measured dataset is projected onto a subspace to lower its dimensionality. The explanation of the variance within the measured data can be achieved by PCA because the original variables of the data matrix are summed and weighted without significant loss of information. Thus, principal components (PCs) are generated and the original variables are weighted and summed. After PCA, the result data matrix is projecting into orthonormal sub-spaces and expressed in the PCs. Before PCA, the complex impedance data are combined into the matrix I which contains the frequency position f and impedance magnitude I vectors:

$$I = \begin{pmatrix} f_1 & I_1 \\ \vdots & \vdots \\ f_n & I_n \end{pmatrix} \tag{5.1}$$

Therefore, it is appropriate to extract the most dominant changes within the measurement data using PCA and then to determine to which features these changes correspond.

Linear combinations of orthogonal vectors are expressed by the output data matrix which is along the directions of the PCs. The biggest variation in the waveforms is accounted by the first principal component (PC1). The subsequent components correspond to the remaining variability. The second principal component (PC2) has lift-off independence, and linear combinations of these optimally-weighted summed

variables are expressed by PC1 and PC2. They are optimal in the sense that the maximal amount of variations in the data is accounted by these components. Therefore, PCA can be applied to reduce the influence of lift-off effect.

5.1.1 Feature Extraction with PCA

As previously described in Section 3.3.1, two features are obtained for the study of lift-off independence. The purpose of this study is to understand these two features from the PCA results and to apply them to reduce the lift-off effects.

Figures 5.1 and 5.2 compare the studied lift-off conditions which include 5 mm step changes in the Z-direction (at 5 mm, 10 mm, 15 mm, 20 mm and 25 mm). Steel samples with the same corrosion stage after 6 months are used for each value of lift-off. The measured parameters are amplitudes of real $Z_{re}(f)$ and imaginary $Z_{im}(f)$ parts of the complex impedance spectra $Z_M(f)$. These can be obtained by extracting the impedance of the respective frequency with the linear sweep frequency technology.

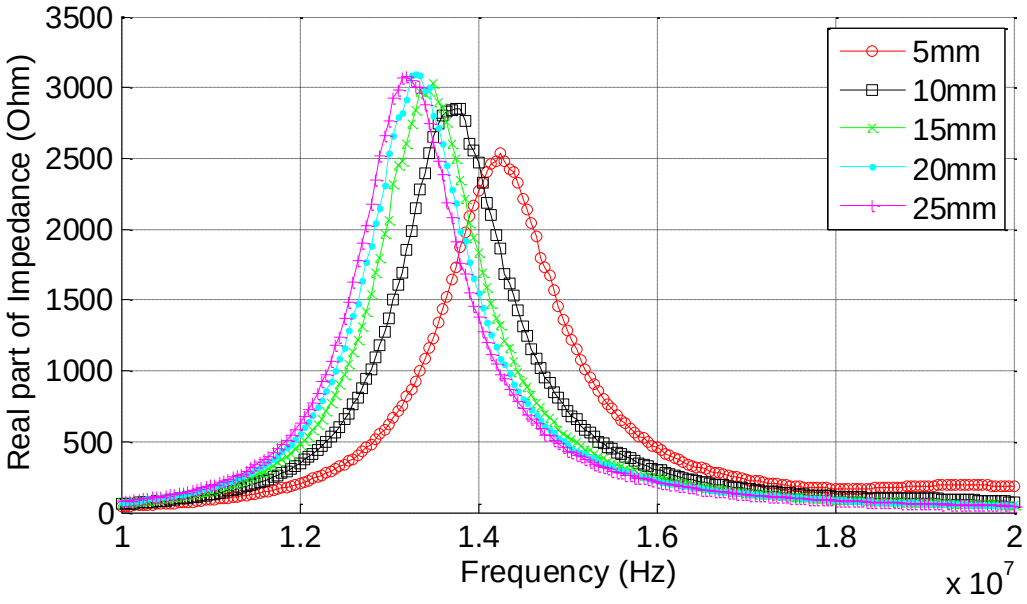

Figure 5.1 Real part of complex impedance variations against frequency at different values of lift-off.

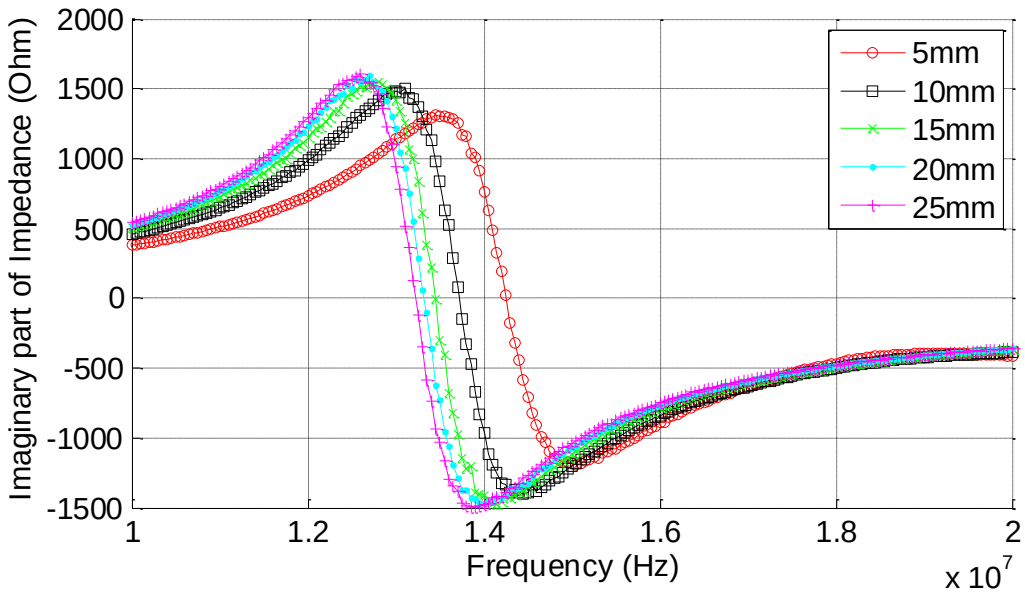

Figure 5.2 Imaginary part of complex impedance variations against frequency at different values of lift-off.

The results obtained from the preliminary analysis of the measured impedance at different values of lift-off are summarised in Figures 5.1 and 5.2. As can be seen, with different values of lift-off, the positions of both amplitude and resonant frequency are changed. It is difficult to provide an individual parameter with lift-off independence for corrosion stage evaluation.

With linear sweep frequency, the imaginary part of impedance exhibits phase shift. Therefore, only measured real part of impedance is then processed by PCA to separate corrosion information from the lift-off effect. Figure 5.3 shows the use of the projection of averaged PC1 for lift-off with the real part of the complex impedance. For better comparison, plots of PCs are averaged over all the measurements per sample. The PC1 projection decreases with increasing lift-off. Comparing these results, the projection of real part of complex impedance has a monotonic relationship with lift-off.

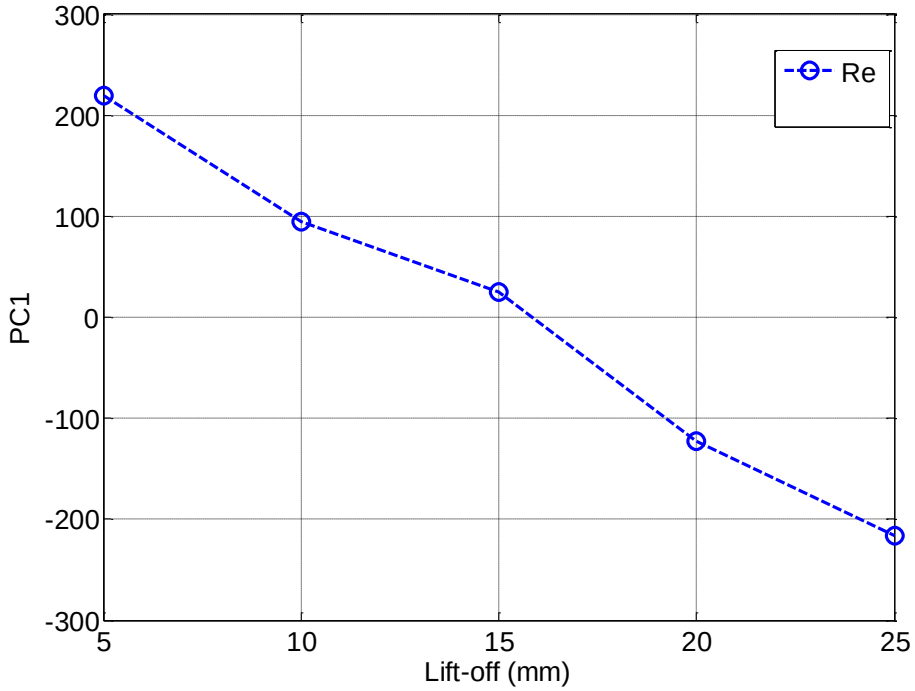

Figure 5.3 Averaged PC1 for 6 months corrosion sample at different values of lift-off.

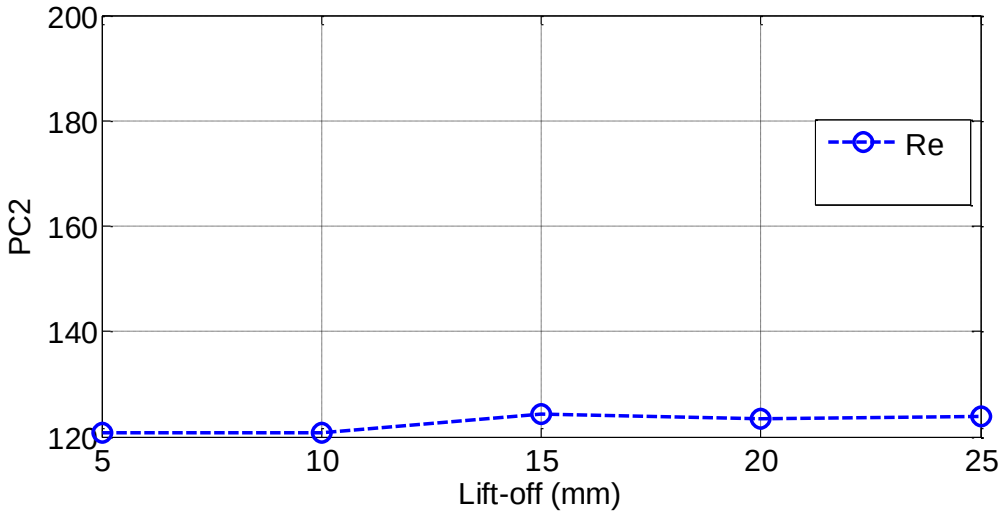

Figure 5.4 Averaged PC2 for 6 months corrosion samples at different values of lift-off.

Figure 5.4 shows the PC2 projection for corrosion detection at different values of lift-off from 5 mm to 25 mm. These projections are independent of different values of lift-off. All five measurements for the 6 months sample are approximately the same and can be clearly distinguished from lift-off effects. From these results, the real part of the impedance data is suitable for reducing the influence of lift-off.

5.1.2 Experimental Study

In this study, different lift-off conditions in the Z-direction with different corrosion stages have been investigated. Different stages of corrosion samples are measured at different values of lift-off. The results obtained from the preliminary analysis of the measured impedance at different values of lift-off are summarised with different lift-off, the positions of both amplitude and resonant frequency are changed. It is hard to determine an individual parameter with lift-off independence for the purposes of corrosion stage evaluation.

The measured real part of complex impedance data is then processed by PCA to separate corrosion stage information from the effect of lift-off. Figure 5.5 shows the use of PC2 projection for lift-off independence with the real part of the complex impedance data. The PC2 projection decreases with increases in exposure time. The corrosion stage can be distinguished at different values of lift-off.

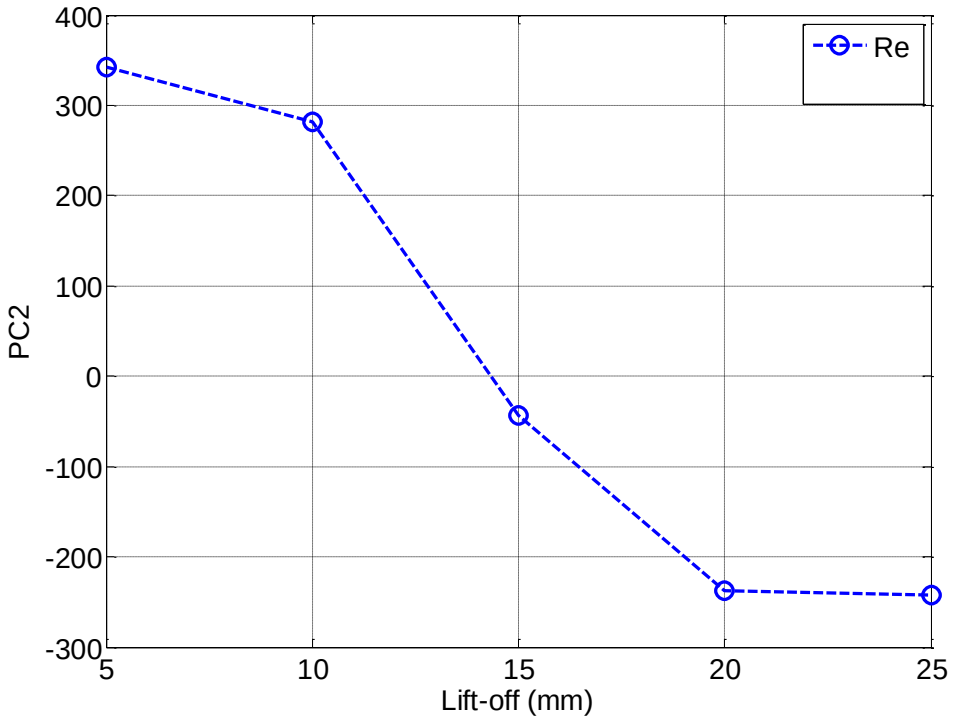

Figure 5.5 Averaged PC2 projection for corrosion samples with different exposure times.

Due to the nature of corrosion, the relationship between the variation in the physical properties of the corrosion layer and exposure time is not always monotonic. Comparing 6 months with 10 months, the results from these values of PC2 projection show that the difference between them is relatively small, which is in line with the results in the previous section. PC2 has an almost monotonic relation with corrosion stage. Furthermore, the correlation coefficient of impedance and PC2 features is over 90%. These preliminary results show that the analysis of impedance in combination with PCA is effective in differentiating corrosion stage information from lift-off effects. From 20 mm to 25 mm lift-off, there is no monotonic relationship with PC2 due to the nature of corrosion progression.

HF RFID-based corrosion sensing is limited by sensing area and the lift-off effect. Therefore, microwave NDT is required for the inspection of a large area under thick insulation. In the following section, the lift-off effect is studied using microwave NDT in experimental investigations.

5.2 Characterisations of Lift-off Effects using NMF

For inspection under thick insulation, the use of microwave NDT is proposed. Inspection with microwave NDT can either be contact, as in previously mentioned work, or non-contact. There is a small air gap of around 1mm between the surface of sample and the probe, which is termed lift-off [170-172]. In a real application, it is difficult to achieve this due to rough surface and the complex geometrical shape of the surface and probe. Moreover, many applications require non-contact inspection as this protects both the probe and the surface of the sample and allows a smooth movement of the waveguide probe over the surface of the sample. Lift-off has a strong influence on the acquisition of signals during measurement. Thus, it is necessary to investigate the influence of lift-off at larger distances beyond 1mm. This section aims to analyse the

impact of lift-off on the estimation of defect geometry and location. The lift-off effect considered here is the variation in distance between the waveguide probe and the surface of the sample.

One main advantage of microwave NDT is that the microwave can penetrate the dielectric layer suffering very little loss. This section presents an experimental study using an open-ended waveguide operating in the X-band at 8.2 GHz to 12.4 GHz for corrosion detection at different values of lift-off from 1.5 mm to 11.5 mm. The reflected signals from the sample under test are acquired by a vector network analyser (Agilent PNA E8363B). This equipment produces a frequency spectrum of the received signals which is utilized for defect detection and influence analysis of lift-off. As the frequency spectrum of the received signals differs between defect and non-defect area, the nonnegative matrix factorization (NMF) is used to extract the unique characteristics of the spectra.

The theory of an open-ended rectangular waveguide probe has been described by Huber [173]. Waveguides utilized for different frequencies are usually allowed propagating only the dominant mode. The dominant TE_{10} (transverse electrical) mode is propagating in the aperture of the rectangular waveguide.

Microwave NDT is dependent upon surface current distribution for detecting defects on metal surfaces. The waveguide generates an incident wave which will cause an induced surface current. When defect is present, it will cause a perturbation in the induced surface current density. The defect can be considered as a polarization filter which scatters maximally when the incident electric field is perpendicular to its longest dimension as the defect converts part of the incident wave into an orthogonally polarized wave.

Therefore, surface currents are disrupted and higher order modes are generated when

the probe encounters a defect [154]. During measurement, the length of the defect is parallel to the longest dimension of the waveguide, and is orthogonal to the electric field. The magnitude of the reflected signal exhibits a conspicuous shift in the location when the defect is encountered with the waveguide aperture comparing with when the non-defect is inside the aperture. The variation in the reflected signal is then monitored and analysed in the frequency spectrum.

5.2.1 Mixing Spatial-frequency Spectrum Model

The X-Y scanner moves the open-ended waveguide probe in a raster-like motion over the sample, acquiring data from the surface. This can then be visualized as an image, as shown in Figure 5.6.

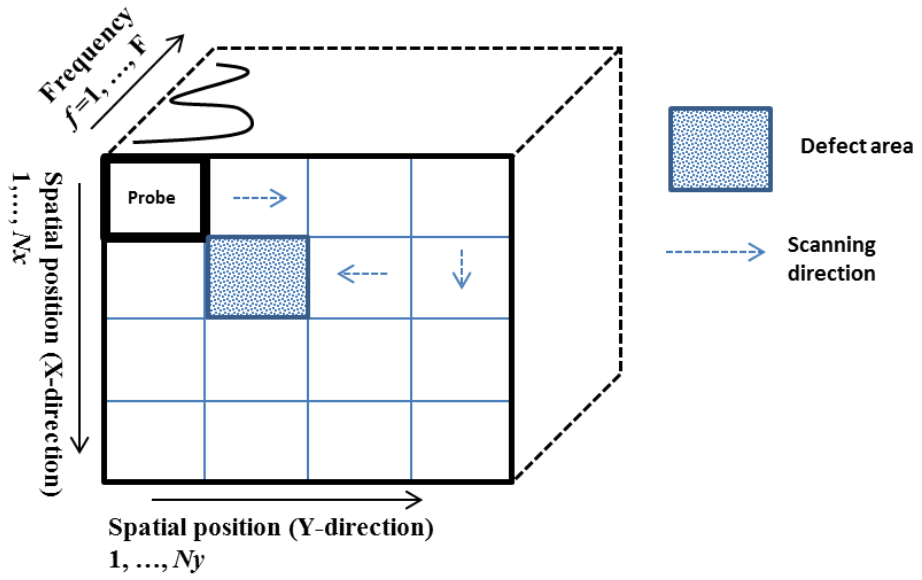

Figure 5.6 Microwave NDT&E C-scan progress.

Figure 3.7 shows that this dataset can be considered as the tensor representation of mixing spatial-frequency spectrum observation **Y** (reflected signal), which is a combination of defect and non-defect spatial-frequency spectrum sources.

In **Y** , the frequencies are given by $f = 1,2,\ldots,F$, where F represents total frequency units. The tensor observation can be expanded in matrix format as

$\mathbf{Y}' = [\text{vec}(\mathbf{Y}(1)), \text{vec}(\mathbf{Y}(2)), \ldots, \text{vec}(\mathbf{Y}(F))]^{\mathrm{T}}$, where $\mathbf{Y}(f)$ denotes the spatial-frequency spectrum matrix with dimensions $N_x \times N_y$ of the f^{th} slice of $\mathbf{Y}$, and for which a visual explanation is given as follows. Subsequently, the mixing spatial-frequency spectrum observation at each spatial-frequency point becomes:

$$Y'(f,s) = \sum_{i=1}^{N_s} X_i'(f,s) \tag{5.2}$$

where $Y'(f,s)$ is the mixing spatial-frequency spectrum components, N_s is the number of sources and $X_i'(f,s)$ denotes the defect or non-defect spatial-frequency spectrum component which can be obtained from the vector network analyser. Here, the space slots are given by $s = 1,2,\ldots,S$ and $S = N_x \times N_y$. Note that in Eq. 5.2, each component is a function of s and f. The power spatial-frequency spectrum (PSS) is defined as the squared magnitude of Eq. 5.2:

$$\left|Y'(f,s)\right|^2 =$$

$$\sum_{i,j(i\neq j)}^{N_S} \left(\left|X_i'(f,s)\right|^2 + \left|X_j'(f,s)\right|^2 + 2\left|X_i'(f,s)\right|\left|X_j'(f,s)\right| \cos\theta_{i,j}(f,s) \right) \tag{5.3}$$

where $\theta_{i,j}(f,s)$ measures the projection of $|X_i'(f,s)|$ onto $|X_j'(f,s)|$. As the non-defect spectrum does not overlap with defect spectrum, and therefore, $\theta_{i,j}(f,s) \approx 90$. The term $\left|X_i'(f,s)\right|\left|X_j'(f,s)\right| \cos\theta_{i,j}(f,s)$ can be considered as residual noise. Thus, a matrix representation of Eq. 5.3 is given by:

$$|\mathbf{Y}'|^2 \approx \sum_{i=1}^{N_s} |\mathbf{X}'|_i^2 \tag{5.4}$$

where $|\mathbf{Y}'|^2 = \left[|Y'(f,s)|^2 \right]_{s=1,2,\ldots,S}^{f=1,2,\ldots,F}$ and $|\mathbf{X}'|_i^2 = \left[|X_i'(f,s)|^2 \right]_{t_s=1,2,\ldots,S}^{f=1,2,\ldots,F}$ are two-dimensional matrices with row and column vectors representing the space slots and frequencies or frequency bins

respectively. These denote the power spatial-frequency representation of Eq. 5.2. The superscript "$\cdot$" is an element-wise operation. Eq. 5.3 is a synthesis equation since it describes how $|\mathbf{Y}'|^{\cdot 2}$ is generated as a mixing of $|\mathbf{X}'|_i^{\cdot 2}$.

5.2.2 Experimental Setup

The experimental setup is shown in Figure 5.7. An X-band open-ended rectangular waveguide is mounted on an X-Y scanner to scan the surface of the sample. The probe is a standard WR-90 waveguide with aperture dimensions of 22.86 mm × 10.16 mm ($a \times b$) and flange dimensions of 42.2 mm × 42.2 mm. The waveguide is placed over the sample at a specified lift-off. A vector network analyser (Agilent PNA E8363B) is utilized to provide the excitation signal and to obtain frequency spectrum information from the reflected signal. A PC is used to control and acquire measurement data from the vector network analyser through an IEEE-488 GPIB (General Purpose Interface Bus). The X-Y scanner controller is connected to the parallel port of the control PC. A Matlab program is utilized to control the vector network analyser and X-Y scanner. During measurement, the frequency range is set from 8.2 GHz to 12.4 GHz.

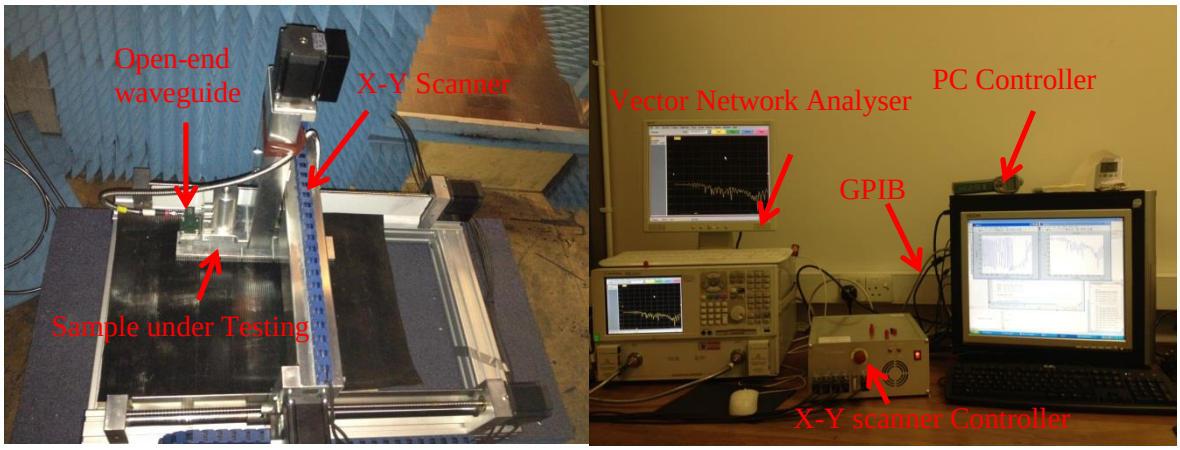

Figure 5.7 Open-ended waveguide system experimental setup.

The reflected X-band spectrum is obtained by using the linear sweep frequency technology with frequency resolution of about 0.02 GHz with 201 linear sweep points,

along with the vector network analyser which measures the reflection coefficient for each operational frequency over the entire X-band frequency range. An aluminium sample of width 50 mm, length 300 mm, and thickness 10 mm with four man-made defects of width 4 mm, length 50 mm, and at depths of 2 mm, 4 mm, 6 mm and 8 mm and a conductivity of $\sigma = 25 \times 10^6$ S/m has been tested, with values of lift-off ranging from 1.5 mm to 11.5 mm.

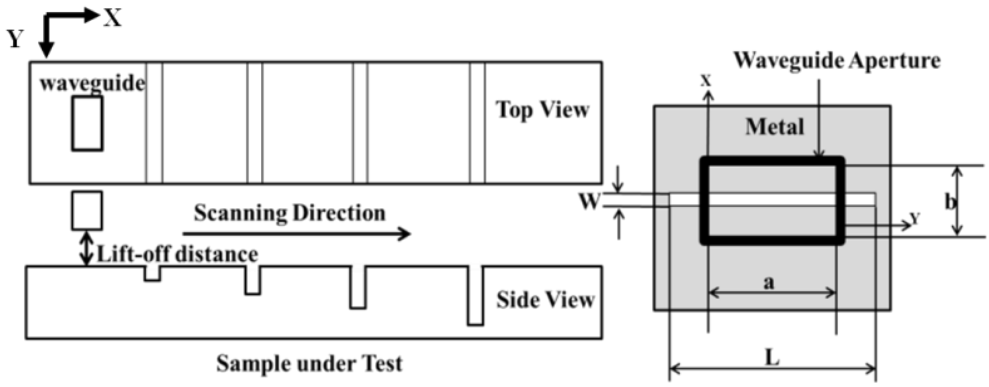

Figure 5.8 Schematic of the aluminium sample and probe scanning direction.

Figure 5.8 shows a schematic diagram of an open-ended waveguide probe scanning over the aluminium sample, where *a* is the broad dimension of the open-ended rectangular waveguide aperture, *b* is the narrow dimension of the open-ended rectangular waveguide aperture, *W* is the defect width, and *L* is the defect length.

A steel sample with a defect of 0.45 mm width and 0.43 mm in depth and conductivity $\sigma = 6.21 \times 10^6$ S/m is also tested. The measurement conditions are listed in Table 5.1.

Table 5.1 Testing setup parameters for microwave NDT.

Parameter	Condition
Operational frequency range	8.2 GHz - 12.4 GHz
Number of swept points	201

Waveguide x-y dimensions (a × b)	22.86 mm × 10.16 mm
Scanning length for aluminium sample (Lx)	260 mm
Defect length L and width W on aluminium sample	50 mm × 4 mm
Defect depths D	2 mm, 4 mm, 6 mm, 8 mm
Lift-off	1.5 mm, 3.5 mm, 5.5 mm, 7.5 mm, 9.5 mm, 11.5 mm
Scanning length for steel sample (Lx)	50 mm
Scanning step for line scan (Δx)	1 mm
Defect length L, width W and depth D on steel sample	40 mm × 0.45 mm × 0.43 mm
Scanning length for steel sample (Lx)	50 mm

5.2.3 Results and Discussion

As seen from Figure 5.9, both spatial-frequency spectra show several abnormal signs due to the differences between defect and non-defect areas. However, this figure does not provide specific information.

By applying the NMF algorithm, it is possible to find specific information. Figures 5.10 and 5.11 show examples of the factorization results of two measurement approaches: the scans of an aluminium sample at 11.5 mm and 1.5 mm lift-off. Four defects can be observed in these figures. The NMF has successfully estimated the activation locations of the defects from the mixing power spatial-frequency spectrum.

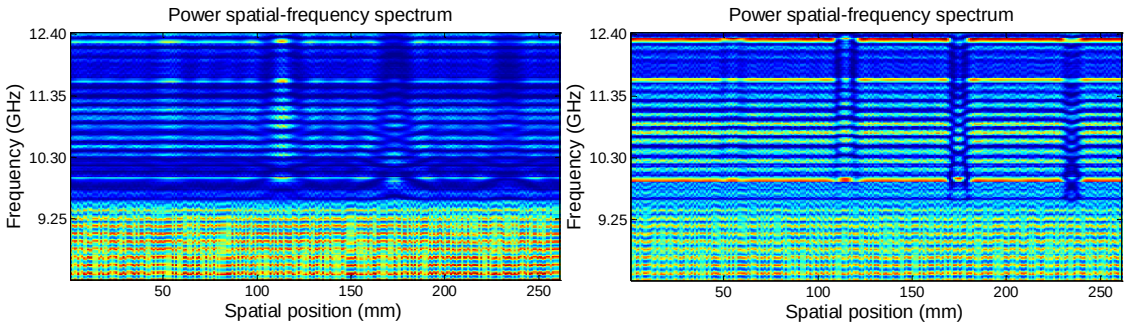

Figure 5.9 The power spatial-frequency of an aluminium sample under test at 11.5 mm lift-off (left); and at 1.5 mm lift-off (right).

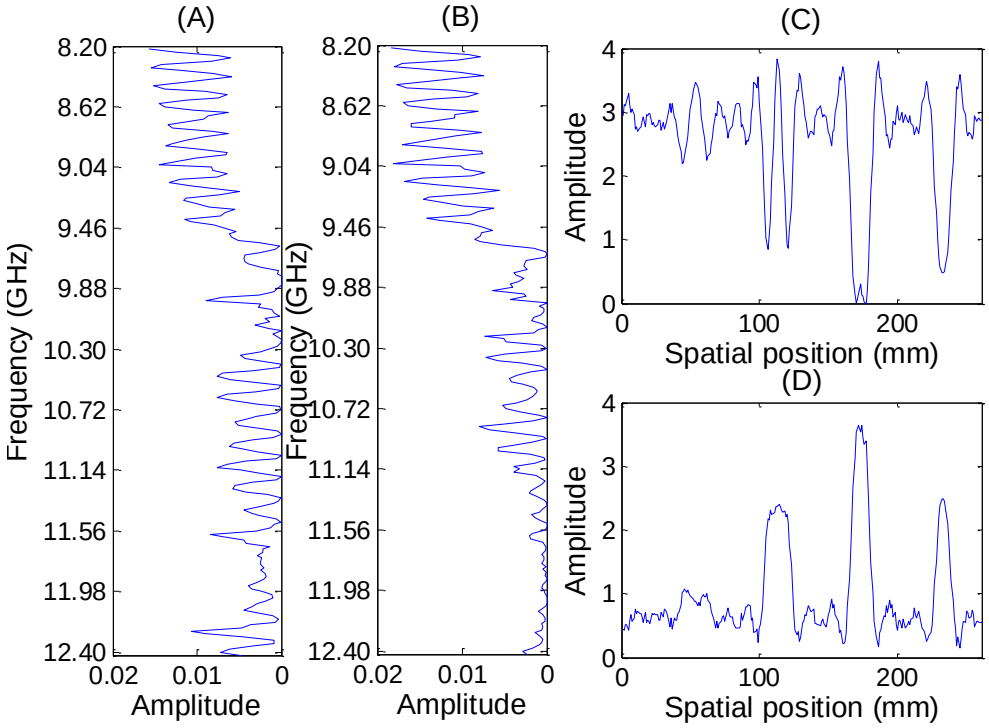

Figure 5.10 NMF estimation results of an aluminium sample at 11.5 mm lift-off: (A) the spectral basis of the non-defect area; (B) the spectral basis of the defect area; (C) the activation location of the non-defect area; (D) the activation location of the defect area.

NMF factorizes the observation matrix into the product of the basis matrix and activation matrix, where the observation matrix is obtained by scanning the whole aluminium sample which consists of both defect and non-defect areas. Figures 5.10 and 5.11 show the factorization results, which are subsequently used to characterise the spectral basis for the defect and non-defect areas, and the activation matrix is used to estimate the defect's location, width and depth. A linear frequency sweep is used to

acquire enough scattering information from sample at different viewing and illumination angles for higher resolution and wider viewing angle of the microwave images.

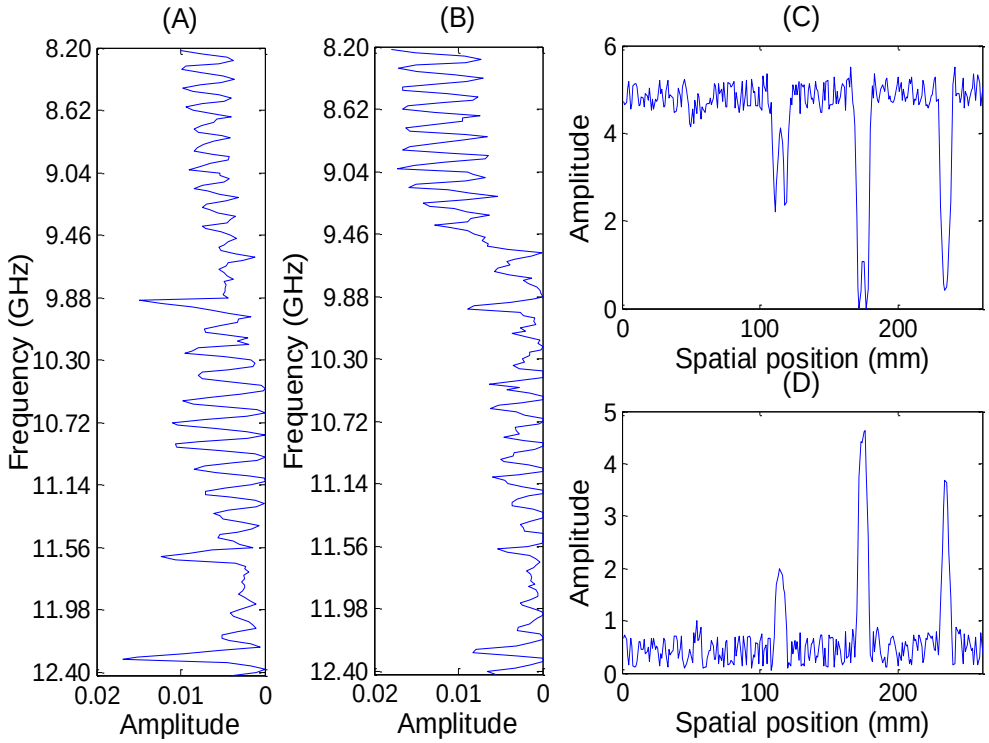

Figure 5.11 NMF estimation results for an aluminium sample at 1.5 mm lift-off: (A) the spectral basis of the non-defect area; (B) the spectral basis of the defect area; (C) the activation location of the non-defect area; (D) the activation location of the defect area.

Figures 5.10 (C) and 5.11 (C) are factorized activation matrices of the non-defect spectral basis. As can be seen from Figure 5.10 (C), when activation peaks are reduced in magnitude, the non-defect spectral basis at that spatial position, which actually refers to the defect's position, becomes inactive. This is because the characteristics of frequency spectra differ between the non-defect area and the defect area. In other words, the activation peaks should increase in magnitude at the same position in Figure 5.10 (D) for defect areas. The same phenomenon is also seen in Figure 5.11 (D) for 1.5 mm lift-off.

It is worth pointing out that the estimated activation location indicates the trend of

defect depth according to attenuation [174]. For the 2 mm to 6 mm defects, the depth information can be predicted with the proposed method. For the defect 8 mm deep, it is still detectable; however, the peak of the trend for this depth is shorter than that of the defect with 6 mm depth.

In order to validate this conclusion, CST Microwave Studio 2012 software is employed to simulate the changes in reflection coefficient from 2 mm to 12 mm deep defects on an aluminium sample. Open (add space) boundary conditions with a hexahedral mesh are used in the simulation. All initial parameter settings in the software are the same as in the real experiments with 1.5mm lift-off. Figure 5.12 shows the simulation results for the reflection amplitude with 2 mm, 4 mm, 6 mm, 8 mm, 10 mm and 12 mm deep defects respectively. These results confirm the finding that attenuation increases with defect depth rising from 2 mm to 6 mm.

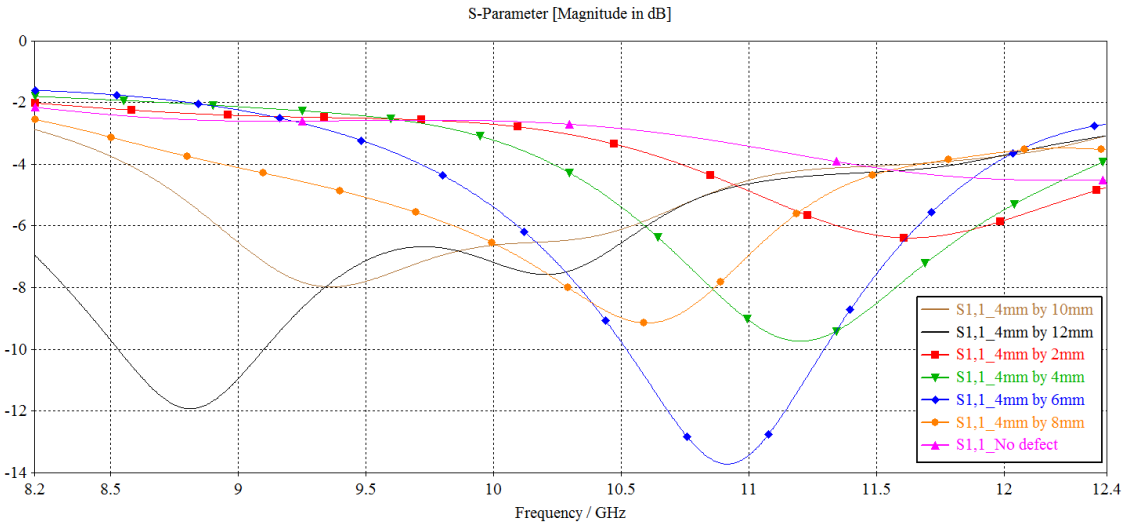

Figure 5.12 Simulated results for different defect depths with 1.5 mm lift-off.

At defect depths greater than 6mm, the outflow of the microwave signal from the waveguide to the base of the defect increases with depth. The proposed algorithm has correctly predicted the trend of the attenuation. For the 8 mm depth defect, the amplitude is not the lowest, as expected. Therefore, the tendency for the 8 mm depth defect has not been correctly predicted. When the defect is near to the waveguide

aperture, the defect causes both the electric (E) and magnetic (H) fields to bend around it. For the 8 mm depth trend, higher attenuation with multiple reflections and the intensity of the bent E-field and H-Field of 8 mm depth is less than that of the 6 mm defect. Thus, the reflected signal from 8 mm defect is also less than that of the 6 mm defect. This has been confirmed and clearly indicated by the proposed algorithm. With depth increase from 8 mm to 12 mm, reflection coefficient is decreasing due to multiple reflections.

A vector network analyser is used to measure the total electric field to detect defect from the waveguide probe, as the probe scanning over the metal. When there is no defect, the reflected frequency spectrum signal remains at a constant level. When a defect is exposed to the probe, a non-constant reflection coefficient is detected for a distance $W' = b + W$, as the red dashed line shown in Figure 5.13, where b is the narrow dimension of the waveguide aperture, and W is defect width.

During the line-scan measurement, the scanning direction of the waveguide probe is normal to the edge of the defect. Hence, the estimated width is $W = W' - b$ (which is 10.16 mm for the X-band waveguide). At 1.5 mm lift-off, the obtained distance W' is around 14.91 mm. The absolute value of the estimated width is $W = W' - b$ = 14.91 – 10.16 = 4.75 mm (compared to the actual value of 4 mm).

It can be observed from Figure 5.13 that the level of accuracy and sensitivity decreases as the estimated defect width increases with increasing lift-off. The defect is still detectable at larger lift-off, although some width information is lost. This is because the lift-off effect is more significant than changing the operational frequency, where radiation through the air-gap widens the characteristic signal.

The correlation between the errors in defect width estimation and lift-off was studied and modelled using a 4^{th} degree curve fitting function to reduce the error in defect width

estimation. These results are presented in Figure 5.14, and correlations of error are provided between these six estimated width errors and the lift-off.

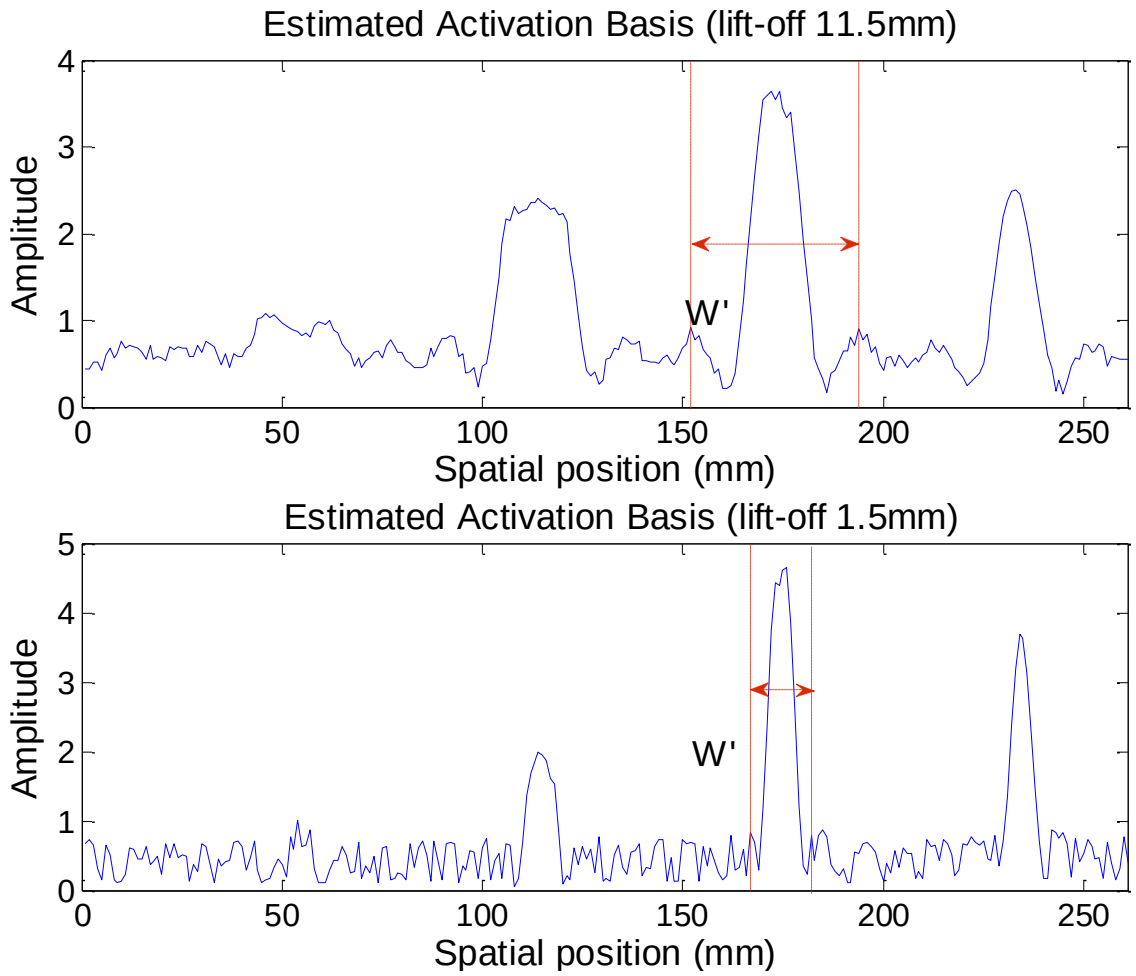

Figure 5.13 Comparison of estimated widths with different lift-off.

When the lift-off is ≤7.5 mm, the estimated error is approximately linearly correlated with lift-off. When the lift-off is >7.5 mm, the estimated error maintains a relatively constant value even when the lift-off increases. Given this relationship, the error between the estimated width and the actual width can be reduced by using $\bar{W} = W - e$, where e is an error term introduced by the lift-off, as shown by the yellow line in Figure 5.14. Thus, the error term e can be estimated. For example, the actual error is 6.75 mm when lift-off is 5.5 mm, and the estimated e = 7.6 mm using the curve fit function, and thus the difference is approximately 10%. Therefore, the lift-off is an important factor which will significantly influence the accuracy of width estimation.

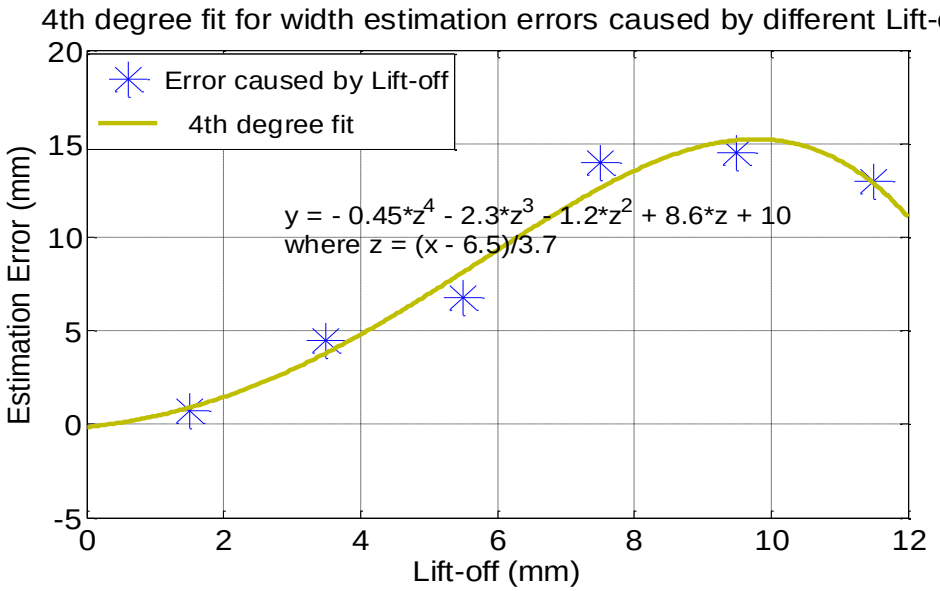

Figure 5.14 Correlation between lift-off and error of defect width estimation.

5.3 Small and Natural Defects Study

This section describes the experiment conducted on the detection of one small defect of 0.45mm in width and 0.43mm in depth, as shown in Figure 5.15.

Figure 5.15 One small defect under measurement.

Figure 5.16 presents simulation results using CST software, and the magnitude of reflected coefficients for both non-defect and defect situations. The magnitude results for non-defect and defect areas are very similar. This is because defect is too small, with dimensions of 0.45 mm in width and 0.43 mm in depth, already touching the boundary of the X-band waveguide detection range. It was decided to use the standard method where one frequency is manually selected, whose magnitude attenuation decreases the least, and this is compared with that of the proposed method. The scanned results of the

real sample are first plotted.

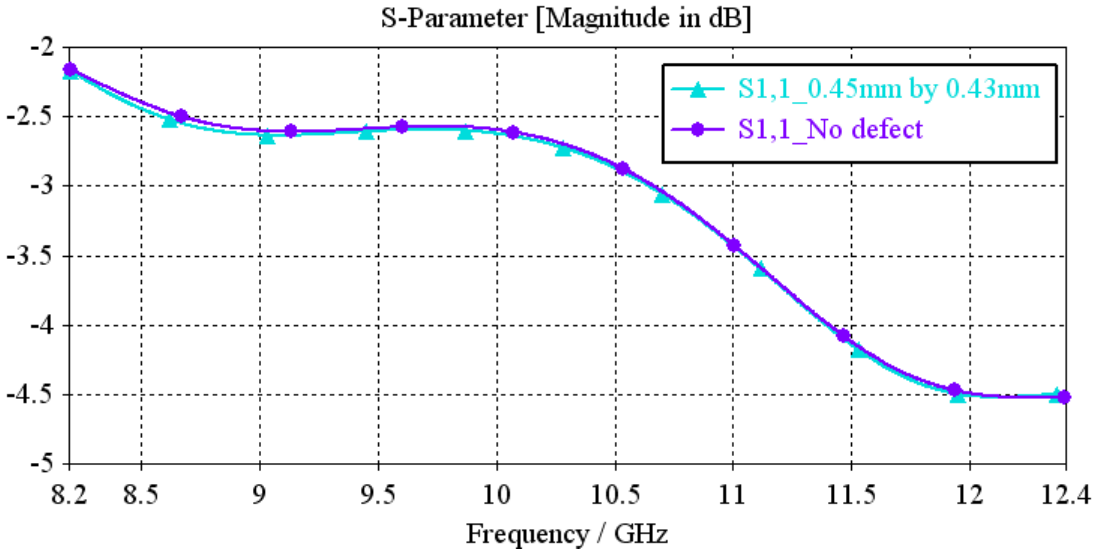

Figure 5.16 Simulated magnitude results of reflected coefficients of defect and non-defect situations across the whole frequency bands.

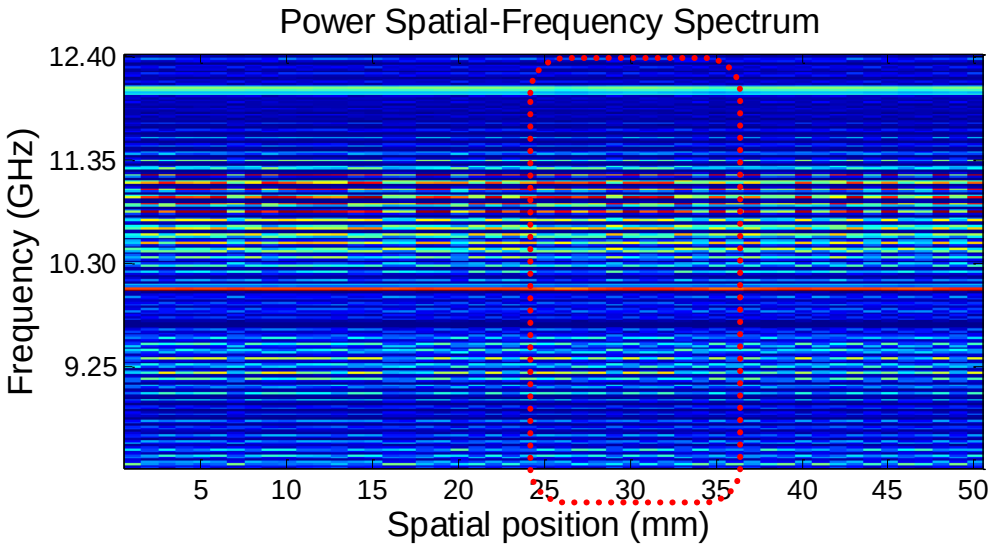

Figure 5.17 The measured power spatial-frequency of a small defect with 1.5 mm lift-off across all frequency bands.

In Figure 5.17, there is no significant difference between the defect and non-defect areas, where the former is highlighted by the red dotted line. The standard method is followed to choose 12.1 GHz [173]. Figure 5.18 shows the real experimental detection results selecting the frequency spectrum according to the above simulation results for this small defect, and along with the detection results using the proposed method.

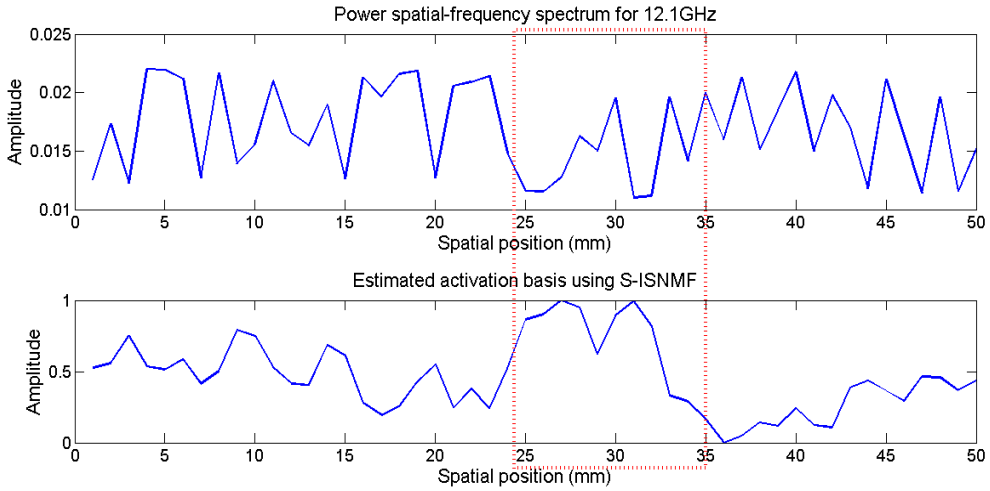

Figure 5.18 Comparison of detection results from the selected frequency method and NMF when measuring a sample with one small defect.

Figure 5.18 shows the defect detection results gained by manually selecting the original single frequency reflection signal based on the simulation results, and those using the proposed method. There is a significant difference between them. As can be seen, by manually selecting the spectrum, it is not feasible to find the abnormal pattern and hence the defect's location is not detectable. On the other hand, because of the unique property of scale-invariance whereby low energy components of the power spatial-frequency spectrum bear the same relative importance as high energy ones, the proposed algorithm is able to detect the abnormal pattern of a small defect, which is marked in red in the figure.

In addition, these results clearly show that, when the size of a defect exceeds the waveguide aperture, the reflected signal only registers very tiny variations. The noise-like feature associated with the signal may cover these tiny variations due to the attenuation of the long coaxial cable and the internal noise of the PNA.

As the defect begins to appear within the waveguide aperture, the amplitude experiences a rapid change in magnitude in the reflection coefficient. The same phenomenon occurs when the defect leaves the waveguide aperture. The resolution of the waveguide system

can be derived as $\rho \approx \frac{\lambda}{D_{x,y}} L$ [175], where $D_{x,y}$ denotes the length of the aperture in the corresponding direction, λ is the wavelength, and L is the distance between the object and aperture (lift-off).

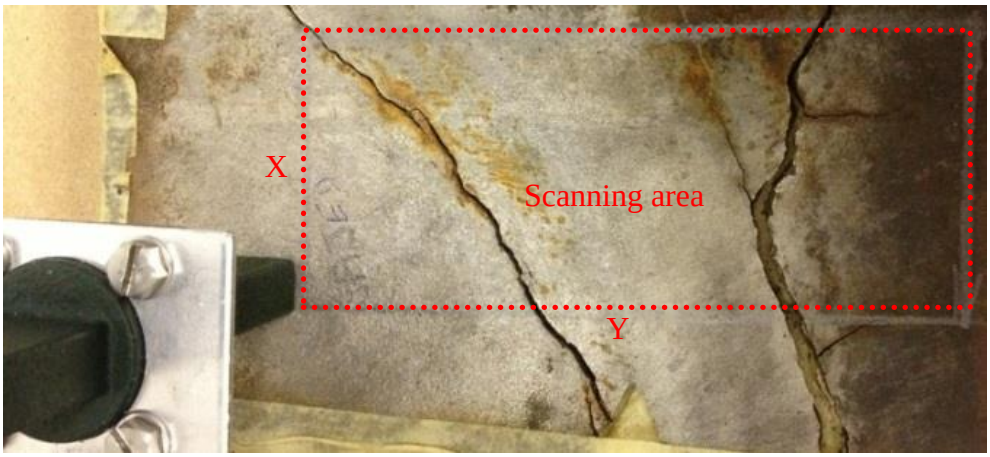

Figure 5.19 Schematic of non-flat steel sample with two natural defects.

For the X-band, 1.58 mm is the minimum size of the defect which can be detected by using this waveguide with 12.4 GHz at 1.5 mm lift-off. As can be seen in Figure 5.19, one steel non-flat sample with two deep defects from corrosion is used to test the proposed method.

As shown in Figure 5.20 (D), the areas shown in dark colour of the two deep cracks have been clearly detected. The area shown in red around two defects is still a defect because it corresponds to natural defects; in addition, there is corrosion, small defects, and roughness introduced by the non-flat surface.

Because this sample is non-flat, it is not feasible to carry out the simulation described above; therefore, four frequency spectrums are manually chosen, using the maximal frequency minus the minimum frequency and dividing by four to choose (12.4 - 8.2)/4 = 1.05 GHz as the specific frequencies for comparison. These are 9 GHz, 10.1 GHz, 11.2 GHz and 12.2 GHz, which already cover the low, middle and high frequency band.

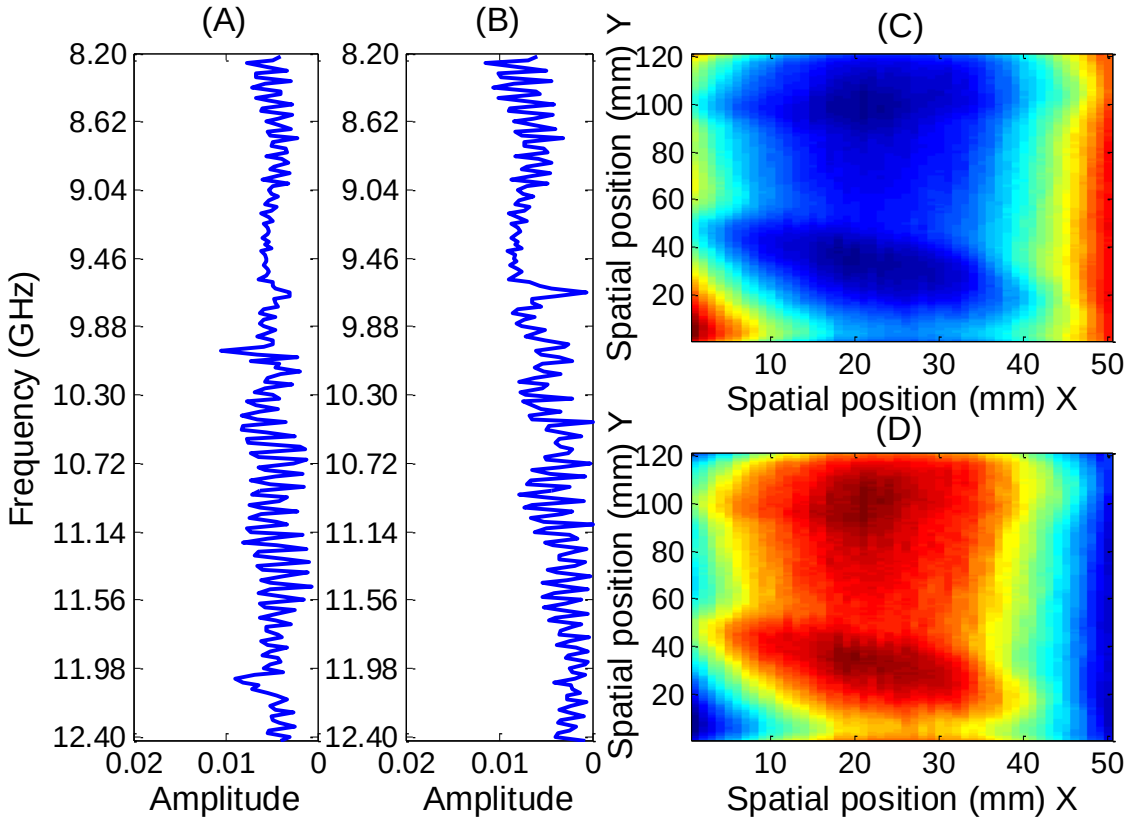

Figure 5.20 Measurement results for natural defects: (A) the spectral basis of the non-defect area; (B) the spectral basis of the defect area; (C) activation basis corresponding to the non-defect area; (D) activation basis corresponding to the defect area.

The results are shown in Figure 5.21. For the manual selection results, it is difficult to choose one result which can fully determine the crack position. In addition, corrosion as well as small defect areas is undetected. However, by using the proposed method, both deeper defects and normal defects are detected.

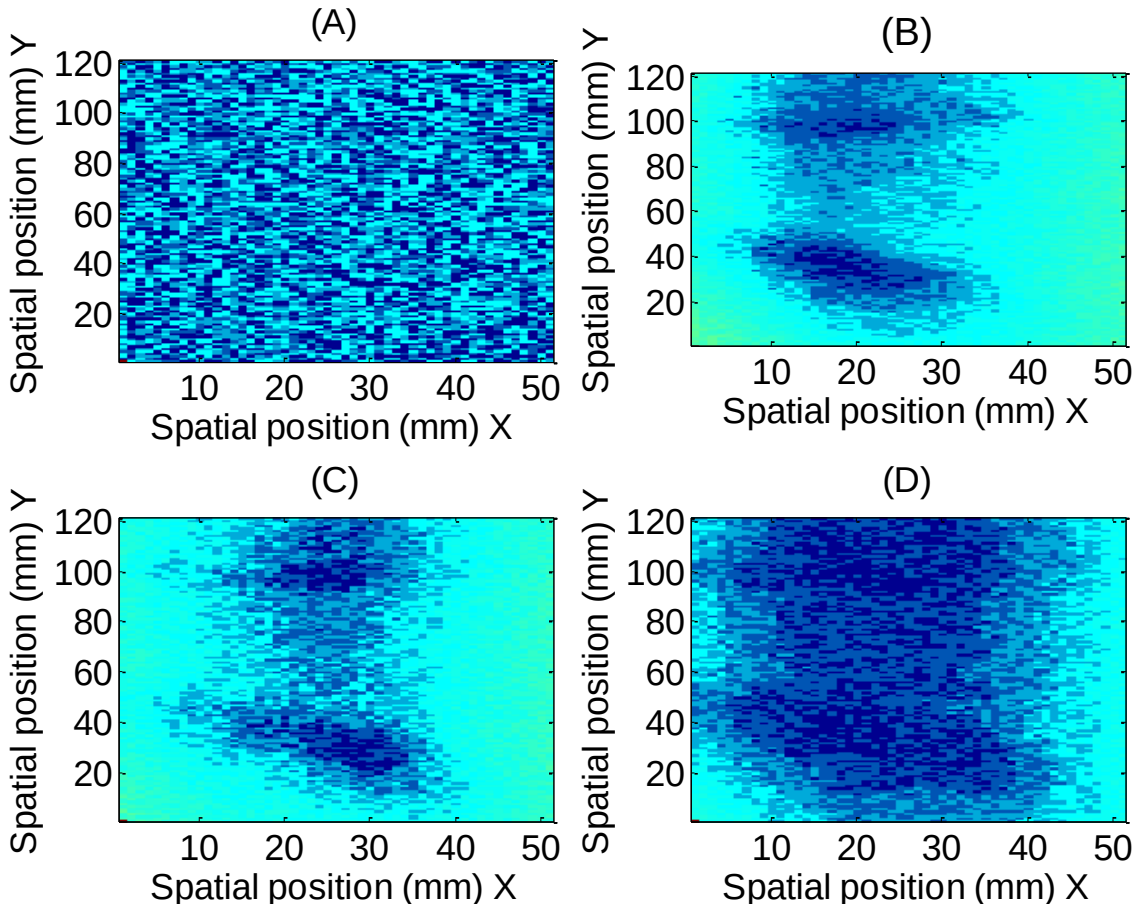

Figure 5.21 Measurement results using the selected frequency point for natural defects: (A) power spatial-frequency spectrum of 9 GHz; (B) power spatial-frequency spectrum of 10.1 GHz; (C) power spatial-frequency spectrum of 11.2 GHz; (D) power spatial-frequency spectrum of 12.2 GHz.

5.4 Chapter Summary

In this chapter, a conventional HF (13.56 MHz) passive RFID-based sensing system in combination with PCA for lift-off independent corrosion detection is demonstrated. Complex impedance is used for the evaluation of the corrosion stage in mild steel samples at different values of lift-off. Principal component analysis has been applied to obtain corrosion stage information from lift-off effects. This study has also found that PC1 is more sensitive to variations in lift-off. Corrosion characterisation based on PC2 to reduce lift-off effects is also studied.

Microwave NDT in combination with NMF is presented for evaluating lift-off effects.

The proposed system utilizes an X-band open-ended waveguide and a vector network analyser. In addition, an efficient spatial-frequency feature extraction algorithm for defect detection and analysis has been developed using the NMF method. This method has the potential to detect and analyse the characteristics of the defects at different values of lift-off. In order to comprehensively evaluate the proposed method, factors that influence defect detection such as depth and lift-off have been studied. Results have indicated that the effect of lift-off can be reduced using the proposed method. The accuracy of defects size estimation can be improved for a larger range of values of lift-off. By using a fitted curve function, the error in the estimation of defect widths caused by large lift-off can be reduced.

These results can be used in further work for reconstruction of unknown defects. NMF requires non-negative values for decomposition. For further investigation, the phase information is employed. Phase information contains negative values, therefore, PCA is used for further investigation. Moreover, in order to increase the range of applicability of the proposed approach, further investigation is carried out in the next chapter for defect detection into insulated metal samples.

Chapter 6. Microwave NDT for Evaluation of Defects under Thick Insulation

The previous chapter has studied the effect of lift-off. However, the maximum lift-off is limited to around 25 mm. In this chapter, a more realistic experimental study is conducted. Three steel sections with defects on the metal plate were insulated. This study demonstrates the ability of microwave NDT to evaluate the shapes and sizes of defects under thick insulation. Specially fabricated thick fire-protect insulated steel panels with embedded defects are inspected using an X-band (8.2 GHz to 12.4 GHz) open-ended rectangular waveguide. The fundamental concept behind the use of this probe is presented along with several experimental results to validate the method for defect detection under up to 40 mm insulation.

Reflected signals are related to magnitude and phase of the reflection coefficients which are used to create images of insulated samples under test. These images indicate the ability of microwaves to identify and size defects under a thick insulation layer. The linear sweep technique is used to obtain multiple frequency spectrum variances. Principle component analysis algorithms have been employed to enhance the resolution of the proposed method. A series of performance comparisons with PCA algorithms is also provided to extract features for reducing the influences of the thick insulation layer. To evaluate the proposed technique, steel samples with known defects under insulation are tested. The results indicate that the capability of defect detection can be enhanced in combination with a suitable signal processing method.

6.1 Samples and Experimental Setup

The experimental setup is shown in Figure 6.1. An X-band (from 8.2 GHz to 12.4 GHz) open-ended rectangular waveguide is mounted with an X-Y scanner. This probe is a standard WR-90 waveguide with aperture dimensions of 22.86 mm × 10.16 mm and the flange dimensions are 42.2 mm × 42.2 mm. The sample is placed under the waveguide

with a specific lift-off.

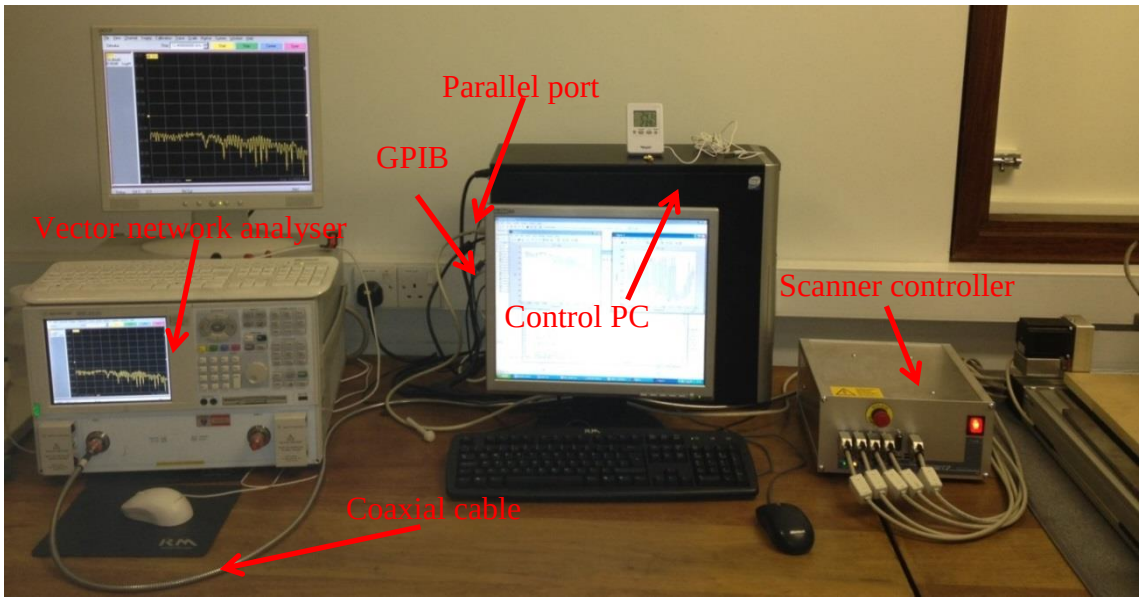

(a) Control and signal processing platform

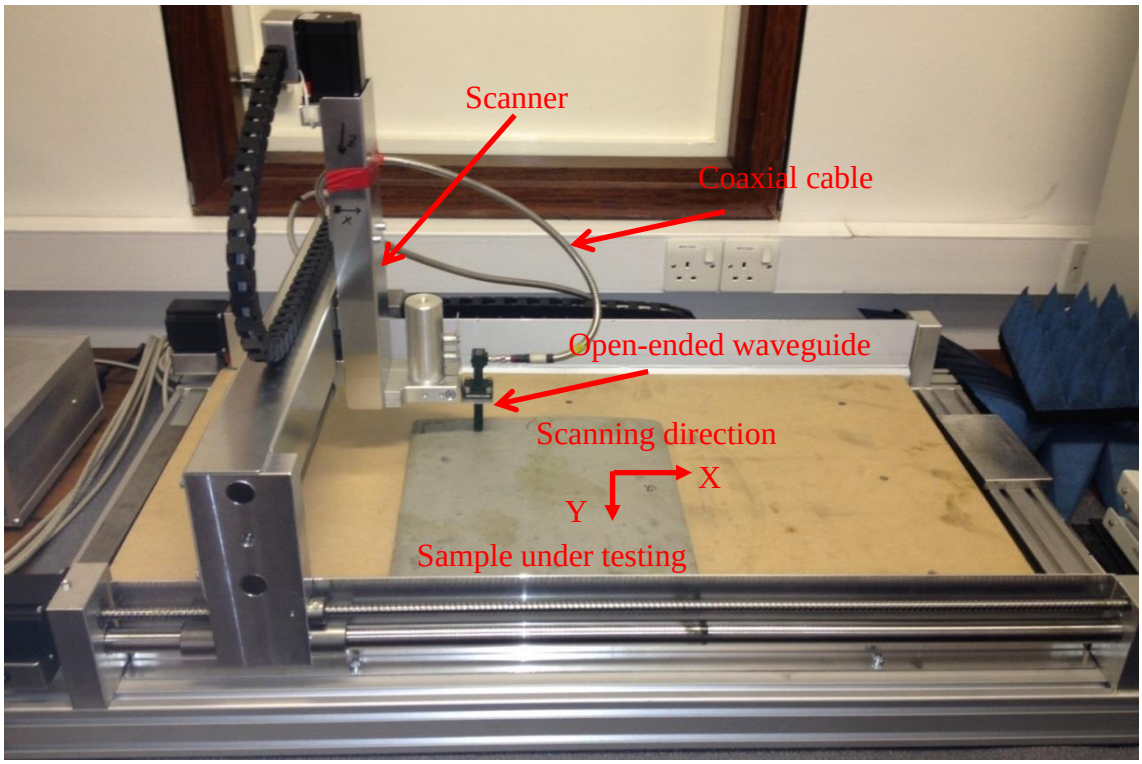

(b) Scanning platform

Figure 6.1 An experimental setup of an open-ended waveguide microwave NDT system.

A vector network analyser (Agilent PNA E8363B) is employed to provide the signal source and to obtain frequency spectrum information from the reflected signal. The

waveguide is connected with the vector network analyser through a coaxial cable. A control PC is used to control and acquire the measurement data from the vector network analyser through an IEEE-488 GPIB (General Purpose Interface Bus). The X-Y scanner controller is connected to the control PC through a parallel port. A Matlab program has been developed and used to control the vector network analyser and X-Y scanner.

During measurement, the frequency range is set from 8.2 GHz to 12.4 GHz. A linear sweep is applied over this frequency range. The frequency resolution is about 0.02 GHz with 201 linear sweep points. The linear sweep frequency technology is used to obtain the reflected frequency spectrum with the vector network analyser. In other words, the vector network analyser measures the reflection coefficient of each operational frequency over the whole frequency range. Lift-off is set at 1.5 mm.

At each measurement location, the waveguide is used to illuminate the sample with a microwave signal and to receive the reflected signal, whose magnitude and phase are then calculated and recorded. These recorded measurement data corresponding to the 2-D scanning space are subsequently processed to produce an image of the sample under test.

Table 6.1 Details of insulated samples.

Sample No.	Identification	Steel base thickness (mm)	Insulation thickness (mm)
D2675/11/3A	A	5	15
D2675/11/3B	B	5	40
D2675/11/3C	C	5	40

A set of steel samples with thick insulation layers has been created. The capability of the proposed systems to differentiate defects under insulation layer has been investigated. As can be seen from Table 6.1, three samples have been created by insulating the steel plates with different thicknesses of insulation.

Figure 6.2 shows the schematic of these steel samples under test. These insulated steel samples with man-made defects were measured with the proposed microwave NDT method.

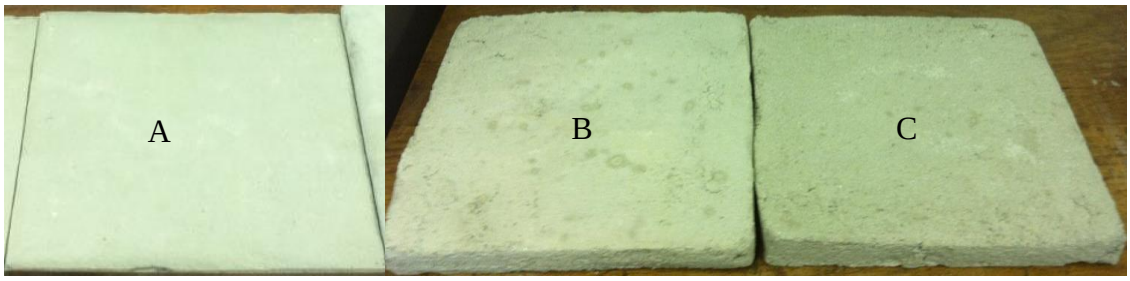

Figure 6.2 Images of insulated samples.

One steel sample contained one hole (19 mm in diameter). The rectangular waveguide probe was used for defect detection, where *a* is the broad dimension of the open-ended rectangular waveguide aperture, and *b* is the narrow dimension of the open-ended rectangular waveguide aperture. The measurement conditions are listed in Table 6.2.

Table 6.2 Parameters setup for microwave NDT

Parameter	Value
Operational frequency range	8.2 GHz - 12.4 GHz
Number of points for linear sweep	201
Waveguide x-y dimensions (a × b)	22.86 mm × 10.16 mm
Scanning setup for steel sample with one	*Lx*=*Ly*= 100 mm

hole under the cement insulation	Scanning step $\Delta x=\Delta y$= 2 mm
	Diameter of hole R= 19 mm
	Insulation thickness= 15 mm
Scanning setup for insulated samples	$Lx=Ly$= 280 mm
	Scanning step $\Delta x=\Delta y$= 2 mm

6.2 Classification and Characterisation of Defect using PCA

A raster-like relative motion of a waveguide probe with respect to the sample gives a dataset that can be visualized as an image.

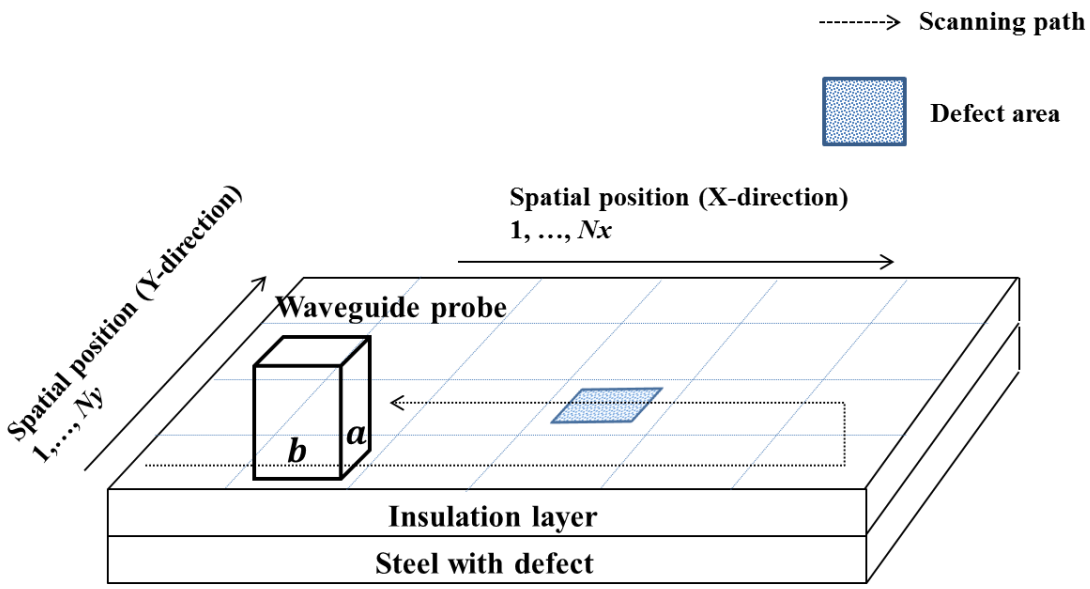

Figure 6.3 Microwave NDT C-scan progress.

As shown in Figure 6.3, the tensor can be considered as representation of the mixing spatial-frequency spectrum observation $\mathbf{Y}$, which is a combination of defect and non-defect spatial-frequency spectrum sources. In $\mathbf{Y}$, the frequencies are given by $f=1,2,\ldots,F$ and F represents the total frequency units. The tensor observation can be

expanded in matrix format to $\mathbf{Y}' = [\text{vec}(\mathbf{Y}(1)), \text{vec}(\mathbf{Y}(2)), \ldots, \text{vec}(\mathbf{Y}(F))]^{\mathbf{T}}$, where $\mathbf{Y}(f)$ denotes the spatial-frequency spectrum matrix with dimensions $N_x \times N_y$ of the *fth* slice of $\mathbf{Y}$. A visual explanation of this tensor flattening process is given in Figure 6.4.

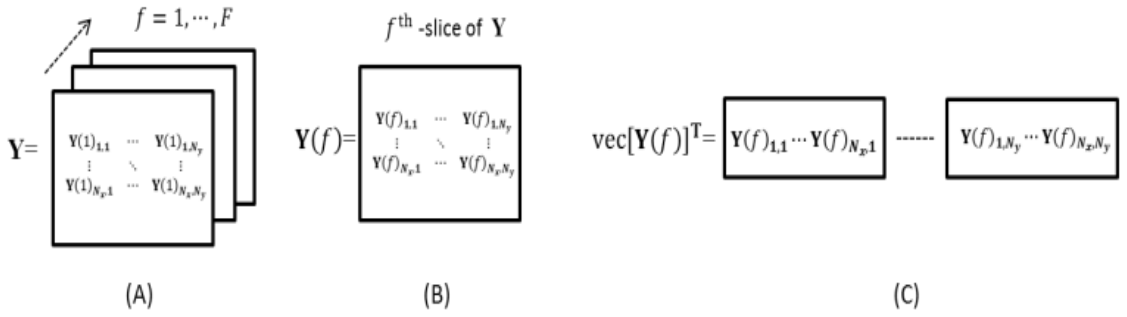

Figure 6.4 (a) Tensor representation of the image sequences $\mathbf{Y}$; (b) f^{th} frame of $\mathbf{Y}$; (c) visual explanation of $\text{vec}(\mathbf{Y}(f))^{\mathbf{T}}$.

In this chapter, both the magnitude $\mathbf{Y}'_M = |\mathbf{Y}'|$ and phase $Y_P^{'} = atan\left(\frac{Im(Y^{'})}{Re(Y^{'})}\right)$ information of $\mathbf{Y}'$ are analysed and then used to generate images of defects. The linear sweep frequency technique is used during the testing, and so multiple operational frequencies have been applied. For further comparison, one operational frequency 12.4 GHz is used to provide 2D images of defects with amplitude and phase. In order to enhance the resolution of the defects' image, principal component analysis has been adopted. The whole X-band frequency range (8.2 GHz to 12.4 GHz) has been used by PCA to extract the information of defects under insulation.

Principal component analysis is extensively used in feature extraction to reduce the dimensionality of the original data by a linear transformation. PCA extracts dominant features from a set of multivariate data. These dominant features retain most of the information, both in the sense of maximum variance of these features and in the sense of minimum reconstruction error. Therefore, PCA is used to extract the defects' information from the influences of rough surface and attenuation of the insulation layer.

The obtained signal contains three uncorrelated source signals: one comes from the surface of the insulation layer, one from within the insulation layer and the third one are from the metal surface.

Because the metal totally reflects microwave signals, the third part of signals is stronger than the other two. However, this signal may be overlapped by the other two with relatively small defects. PCA is used to extract the source of defects from the received signals. $\mathbf{Y}'_M$ is taken as an example of the use of PCA ($\mathbf{Y}'_P$ can be processed using the same step), and can be transformed into uncorrelated sources by means of a whitening matrix based on the eigenvalue decomposition (EVD) of the covariance matrix $E\left\{\mathbf{Y}'_M \mathbf{Y}'^{\mathbf{T}}_M\right\} = \mathbf{EDE}^{\mathbf{T}}$, where $\mathbf{E}$ is the orthogonal matrix of eigenvectors and $\mathbf{D} = \mathrm{diag}\left(\lambda_1, \ldots, \lambda_N\right)$, being $\lambda_1 \geq \ldots \geq \lambda_N$ the eigenvalues. After using PCA to obtain the uncorrelated sources, it is also possible to reduce the transformed output dimension. For example, by choosing $N_s \leq N$, there exists N_s number of uncorrelated sources with a maximally informative subspace of input data $\mathbf{Y}'_M$. In this thesis, both raw data and PCA results are plotted. The plot concretely shows in Figure 6.5 that the resolution of measurement images can be improved using PCA.

To validate the proposed method, one steel sample with a known hole is covered with a 15 mm cement layer. A linear sweep frequency technology has been employed. The results of this sample are presented in Figure 6.5, which shows the line scanning results through the centre of the steel sample under linearly swept frequencies, where the defect area is highlighted with a solid line. The magnitude of the reflection coefficient is used to create images of these defects. The frequency spectrum has been obtained with the linear sweep frequency technique. The hole can be easily detected with higher operational frequencies. However, it is hard to detect the hole in the range of frequencies less than 9 GHz, shown as a dotted line in the Figure 6.5 (a). As shown in

Figure 6.5 (b) after PCA processing, the influence of rough surface and thick insulation have been largely eliminated, the final results have been enhanced compare to original results.

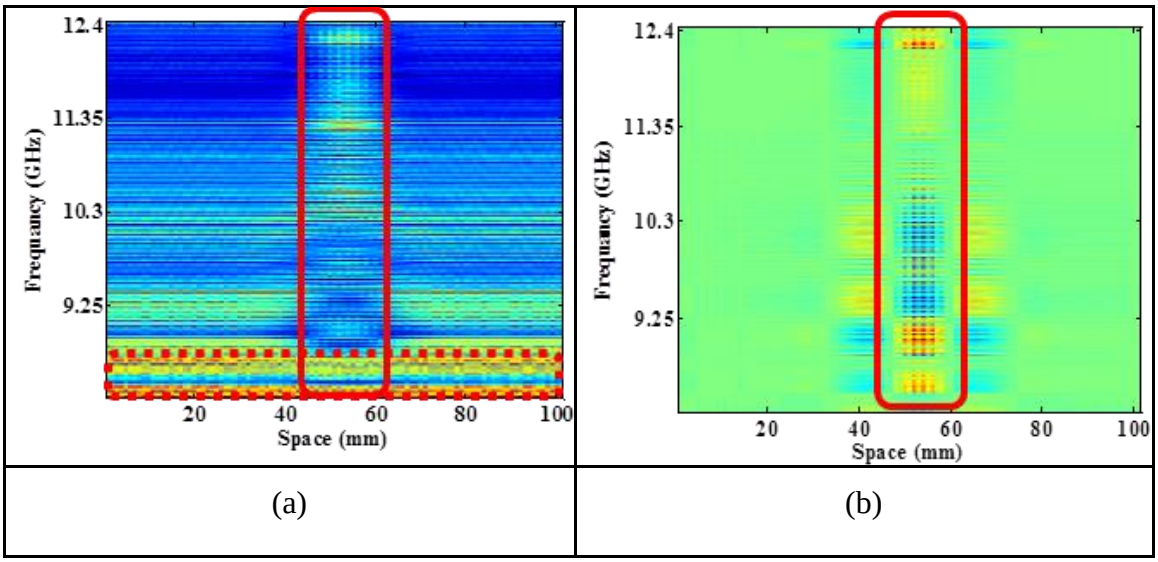

(a) (b)

Figure 6.5 (a) The amplitude spatial-frequency spectrum of steel with a hole under test with line-scan at y = 50 mm; (b) the amplitude spatial-frequency spectrum of steel under test after PCA.

As can be seen from Figure 6.6, the hole can be detected by using both the amplitude and phase of the reflection coefficient. When the probe encounters the opening of a defect, the reflection coefficient is changed, indicating the existence of this defect within the probe aperture. This feature can be used to determine defect size. In fact, the probe observes a non-constant reflection coefficient for a distance b + R when the scan direction is normal to the defect lips, where b is the narrow dimension of the waveguide aperture, and R is the diameter of the hole in the steel sample. During measurement, the scanning direction moves with the dimension of the open-ended rectangular waveguide aperture. The obtained size of the defect is around 32 mm by 30 mm (obtained defect diameter b + R = 10.16 + 19 = 29.16 mm). Error variances between estimated values and real values are less than 3.3%.

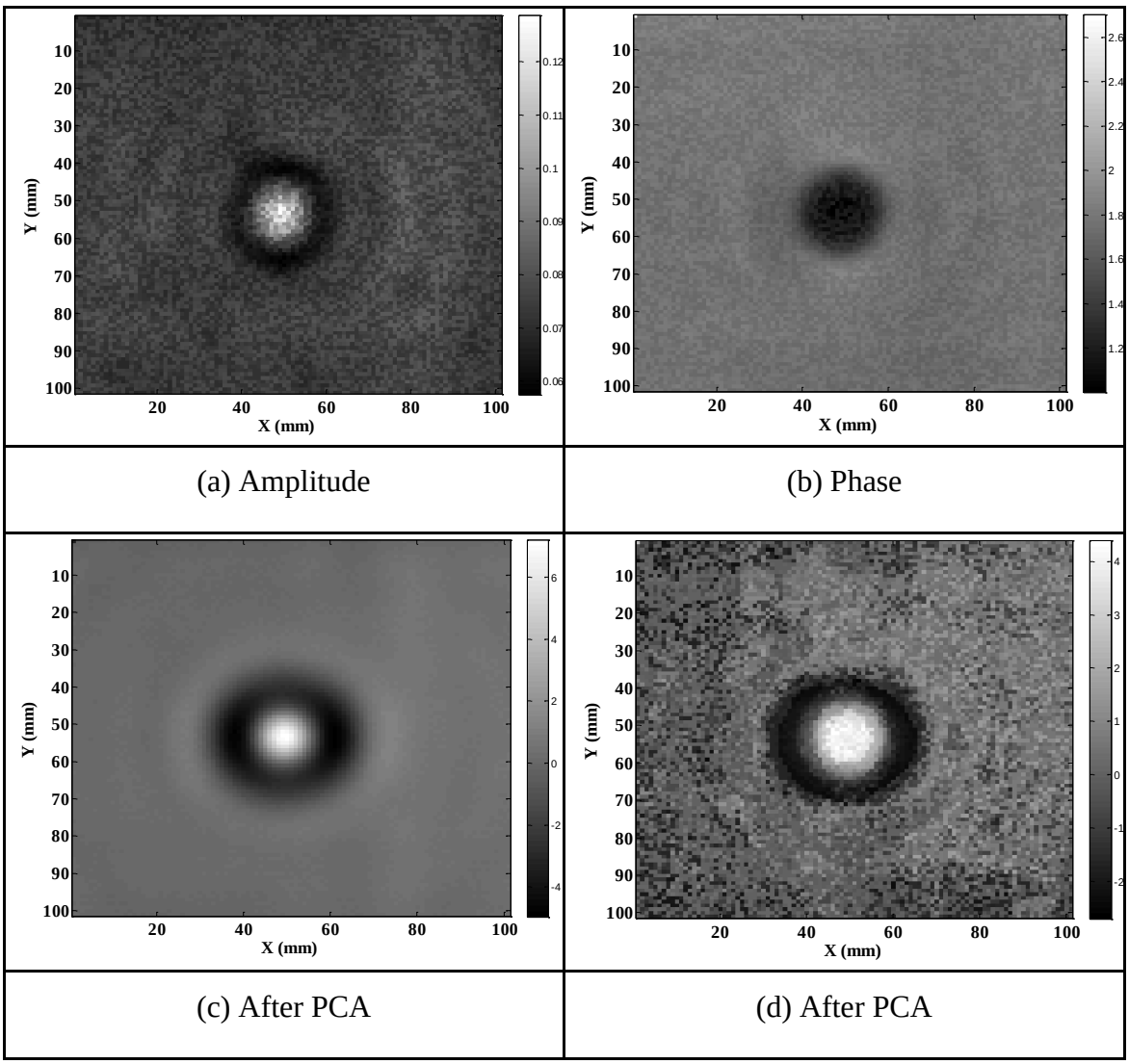

Figure 6.6 Scanning of steel with a hole: (a) amplitude variance; (b) phase variance at 12.4 GHz using X-band waveguide, where with the linear sweep with the X-band frequency range 2D images of the defect can be obtained; (c) amplitude after PCA; and (d) phase after PCA.

Moreover, both amplitude and phase can be used for defect detection under thick insulation, as can be seen from Figure 6.6. Since the surface of the insulation layer is not smooth, phase suffers more influences from variations in thickness and attenuation of insulation layers. As can be seen, the presence of the hole can be easily detected, and a distinct image associated with this hole is produced. One spot surrounded by partial circular ring is representing the existed hole. It is proved that these rings which correspond to the edges of the hole, and their spacing may increase or decrease as a function of the hole diameter, the operational frequency and the dimensions of the

aperture. The rings are not complete circles because of the linear polarization and the aperture dimensions of the waveguide.

As can be seen, the scans produced a signal including the rings is larger than the physical size of the hole. This is advantageous since when the hole is otherwise too small to detect, with this method, the hole could still be detected. Because the reflected signal from non-defect areas share similar spectrum characteristics, and these spectrum characteristics are different from those defect areas, it can be assumed that they are uncorrelated. PCA separates these received signals and projects them into uncorrelated subspaces, and for each subspace the signals share similar features. The first three principal components are used here, accounting for more than 90% of the variance within the data and thus represent the greatest changes within the reflected signals. Thus, most of the reflected signals from non-defect areas have been captured in one PC subspace. On the other hand, the reflected signals from defect areas have been captured in another PC subspace; and therefore these defect areas can be distinguished and the resolution of defect detection results can be enhanced. It can be seen from Figure 6.6 (c) and (d) that more accurate and clear results can be obtained.

6.3 Experimental Results and Discussions

The experimental results and analysis of unknown defects and feature extraction with PCA are discussed in this section.

It can be seen from Figure 6.7 that one small defect has been obtained under 15 mm paint in sample A. The position of the defect has been located. With an operational frequency of 12.4 GHz, the location of this defect has been identified. A comparison of Figure 6.7 (a) with (b) shows that it is much easier to identify the defect using the amplitude rather than phase. But it is still very difficult to estimate the size of the defect. After the application of PCA with the whole X-band frequency range, both amplitude

and phase can be used to estimate the size of the defect, which can be determined easily from Figure 6.7 (c) and (d).

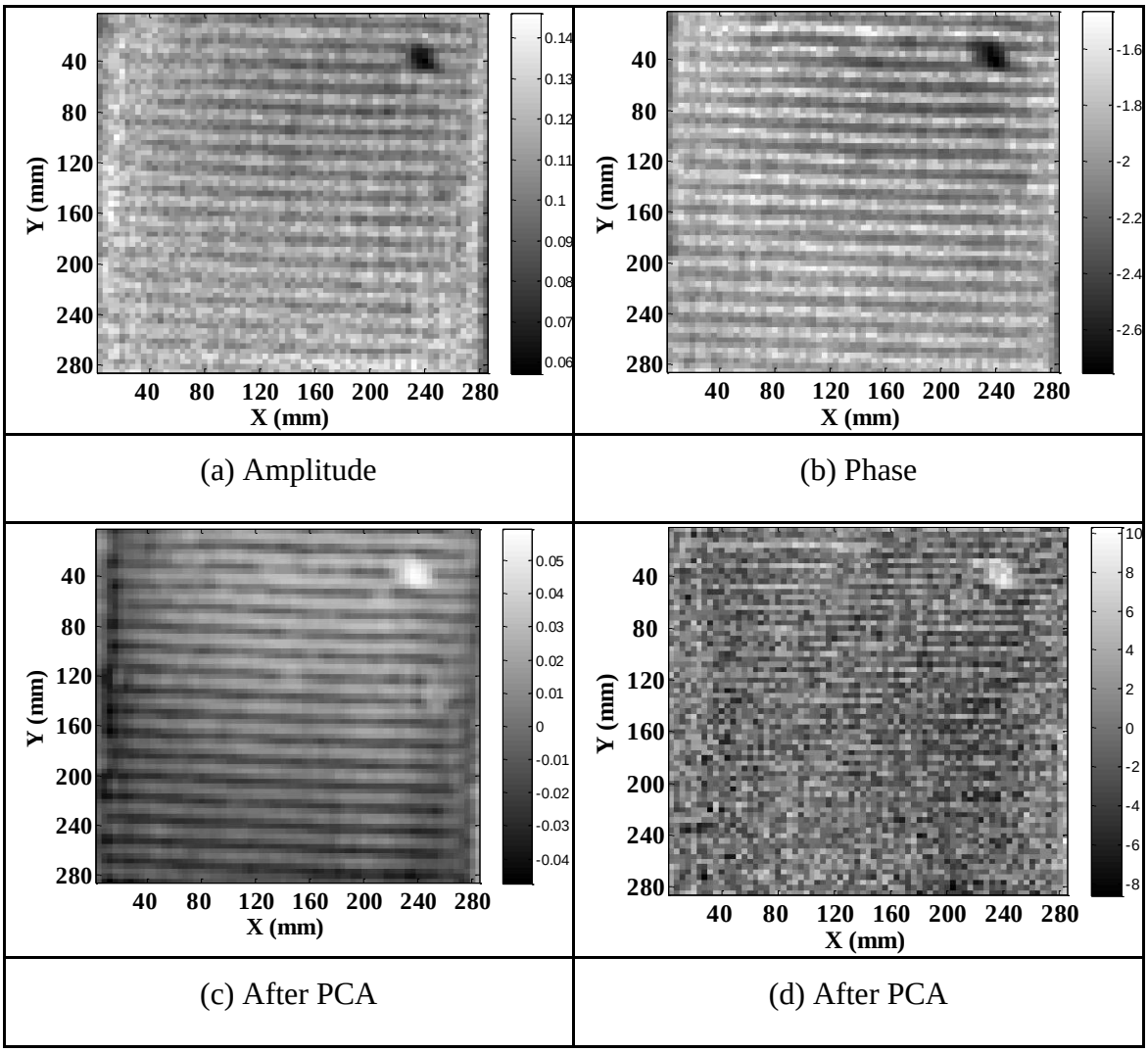

Figure 6.7 Scan of steel under 15 mm insulation: (a) amplitude variance; (b) phase variance at 12.4 GHz using X-band waveguide, so that with the linear sweep with the X-band frequency range 2D images of the defect can be obtained; (c) amplitude after PCA; and (d) phase after PCA.

Texture patterns in Figure 6.7(c) are caused by relative shallow defect and overlapped scanning path. Relative shallow defect results in small variances in magnitude of reflected signals. With 2 mm scanning steps, some scanning area is overlapping due to the relative big waveguide probe which can be overcome by using smaller scanning steps or higher frequency waveguide probe if necessary. PCA is effective in finding

common features among the signals and maximising these common features for pattern reconstruction. The diameter of the defect is around 20 mm.

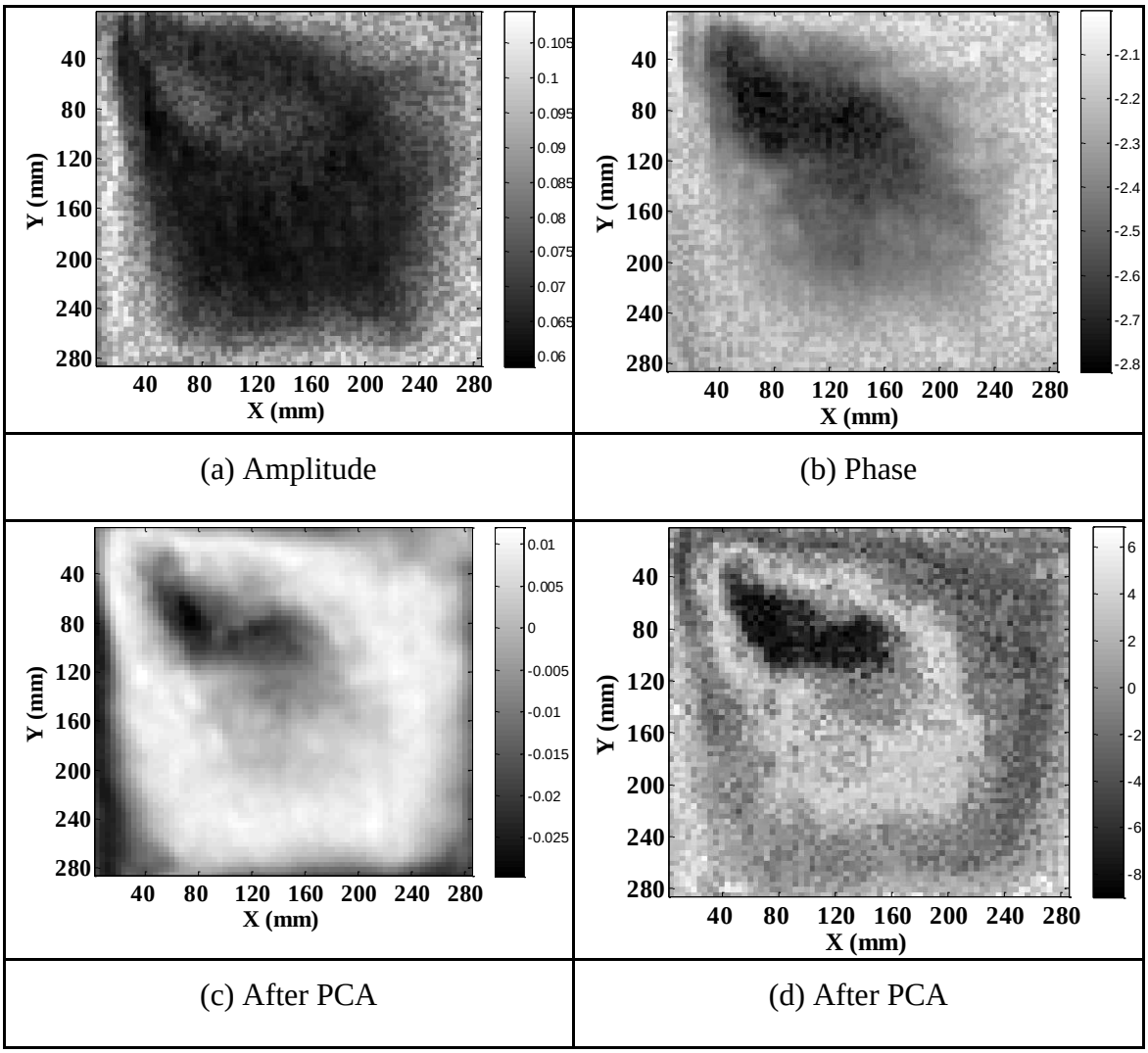

(a) Amplitude

(b) Phase

(c) After PCA

(d) After PCA

Figure 6.8 Scan of steel under 40 mm concrete: (a) amplitude variance; (b) phase variance at 12.4 GHz using the X-band waveguide, where with a linear sweep with X-band frequency range 2D images of the defect can be obtained; (c) amplitude after PCA; and (d) phase after PCA.

Sample B is a steel plate insulated with concrete of 40 mm thickness. A defect has been punched in the metal plate. Location and area of a defect can be detected using phase when only employing one operational frequency, as can be seen in Figure 6.8 (a) and (b). The use of phase is more sensitive than amplitude. The punched area has been located after using PCA with amplitude and phase, as shown in Figure 6.8 (c) and (d). The size of the defect is around 100 mm by 70 mm. More accurate results have been

obtained from these images. Another important finding is that more accurate results have been obtained with amplitude after PCA. After the application of PCA, both amplitude and phase results have been enhanced, and the shape of the defect is identified with the proposed method.

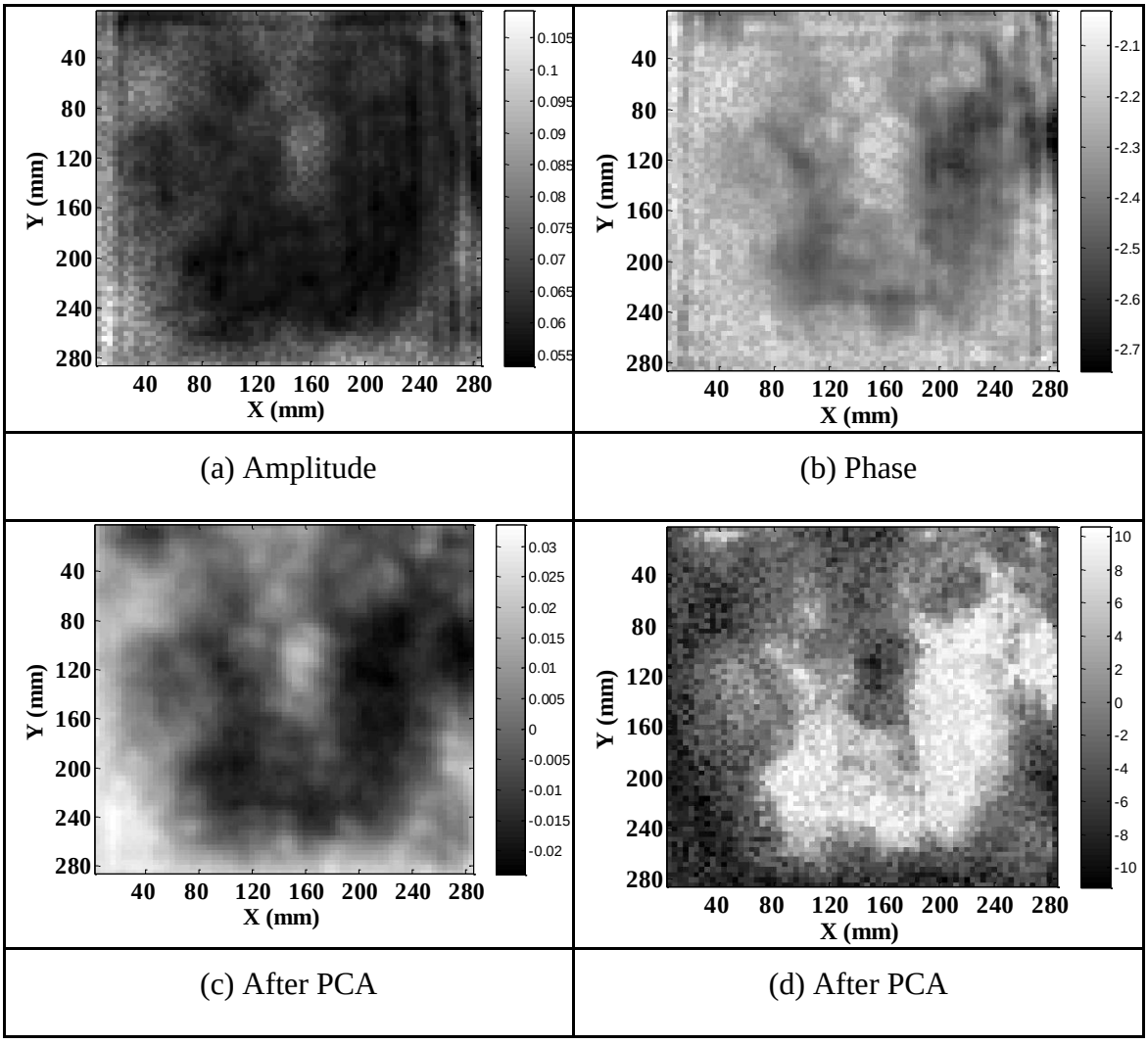

Figure 6.9 Scan of steel under 40 mm concrete: (a) amplitude variance; (b) phase variance at 12.4 GHz using X-band waveguide, so that with a linear sweep with the X-band frequency range 2D images of the defect can be obtained; (c) amplitude after PCA; and (d) phase after PCA.

Sample C is also insulated with 40 mm thick concrete. Comparing the amplitude results with the phase results, the former suffer more influence of variation in insulation thickness and surface roughness. As can be seen in Figure 6.9 (a) and (b), the defect area has been obtained using phase when only one operational frequency is employed.

As can be seen from Figure 6.9 (c) and (d), the defect area has been located after applying PCA. Another important finding is that PCA can be used to separate the influence of the insulation layer. The shape and location of the defect are much clearer after PCA is applied.

6.4 Chapter Summary

The ability of microwaves to penetrate non-conductive material makes microwave techniques attractive for inspection for the presence of defects under non-metallic layers. In this chapter, a novel microwave NDT-based imaging system has been presented which achieves defect detection under thick insulation. This system uses a rectangular waveguide with a vector network analyser for non-destructive testing. The reflection coefficient is used to create images of samples under test. These images indicate the ability of microwaves to detect and locate defects of different sizes and shapes in metal samples.

Simple C-scans reveal the potential of this technique as a tool to inspect the integrity of insulated steel samples. Defect location has been demonstrated to be an easy task when using the suggested technique. In addition to detecting and locating defects, the influence of thickness variations in the insulation layer have been reduced in conjunction with principal component analysis. A new approach to defect classification and characterisation based on the linear sweep frequency and PCA has been demonstrated. PCA globally analyses across the whole frequency range and therefore avoids the interpolation issue faced by conventional Fourier-based methods. The linear sweep frequency technique with PCA largely eliminates the influence of rough surface and thick insulation.

Overall, the results are very encouraging. The microwave-based techniques utilizing open-ended rectangular waveguides can be used to detect the presence of surface

defects in metal under thick insulation. Images have been generated from 2-D raster scans which can determine the size and location of defects under insulation.

Chapter 7. Conclusions and Future Work

This chapter draws conclusions for the study. Based on the research outcomes, recommendations are then made for further work.

7.1 Summary

The limitations of existing NDT&E techniques require novel approaches to handle the challenges posed by insulated structures. One of the main challenges is the inaccessibility of the sample surface under a thick insulation layer. From the literature, it was found that several methods can be used to overcome the problem of thick insulation layers. These involve either high-power acoustic systems, which are bulky in size, or the use of radiography. The latter methods require access to the surface through the removal of insulation or the use of inspection holes. In this study, the potential of HF passive RFID in conjunction with microwave NDT for the monitoring of corrosion and defects under an insulation layer has been investigated.

HF passive RFID tags for sensing can be used to detect a variety of phenomena. Their cost-efficient, small size and battery-free operation are the biggest factors leading researchers to further explore this technology for sensing. A majority of studies of passive RFID sensing involve modifying tags through attaching either special reactive thin films or sacrificial elements to the tags. These methods not only increase costs but also limit the long term monitoring capability of the tags. The method proposed in this study overcomes these problems by investigating the interaction between the tag's coil and ambient metal as the sensing mechanism. No modifications to the tag are required with the proposed method, which allows commercial off-the-shelf tags to be used. Moreover, the sensing area and lift-off tolerance of RFID-based sensing is limited. Therefore, microwave NDT-based imaging is proposed for inspection under thick insulation.

The fundamental operating principle of RFID, as described in Chapter 3, relies on a magnetic flux penetrating between the reader's coil and the tag's coil. In free space, the magnetic flux caused by the reader is penetrating the tag's coil. When a metal is brought in proximity to the tag, an eddy current is introduced in the vicinity of the tag and a demagnetizing field induced by this eddy current reduces the original magnetic field necessary for energy and data transmission. This reduction decreases the amount of energy absorbed by the tag and hence the transmission distance is reduced. As corrosion develops on the metal, the thickness of corrosion layer increases along with decreases in the electrical conductivity and magnetic permeability of the corrosion layer will result in an increase in the penetration of the magnetic flux towards the free space value. Meanwhile, monitoring an area with an RFID tag is limited by the size of the tag, which is insufficient for structural monitoring. Therefore, microwave NDT is developed to overcome the issues of the monitoring of large areas and the effect of lift-off. The most important advantage of microwave NDT is that the microwave signal can penetrate the non-metallic insulation layer without suffering much loss. Meanwhile, this contactless microwave NDT-based imaging leads to good resolution in inspection under thick insulation. The theoretical background of microwave-based NDT for detection under insulation has been presented.

Two initial experimental feasibility studies, as detailed in Chapter 4, were carried out using artificial corrosion samples to investigate the detection capabilities of the proposed systems in differentiating between different surface conditions and corrosion grades. The first sample set consisted of four mild steel corrosion plates with four different conditions of surface preparation. Using peak-to-peak amplitude feature, the HF RFID has been investigated for the detection of general corrosion and surface conditions in mild steel. On the hardware side, four commercially available tags were selected for this study. These tags are of a variety of sizes and shapes to be used for

different surfaces and applications. The reader unit is built with 100 mm by 80 mm reader coil. The measurement results demonstrate that the HF RFID-based sensing system can be used to distinguish between not only a corroded sample and a non-corroded sample but also different corrosion progression conditions.

The second sample set used consisted of another four rectangular mild steel plates with a 30 mm × 30 mm square corroded region in the centre of each plate. These plates were corroded by exposing them to the atmosphere for 1, 3, 6, and 10 months. An approach adopting commercial passive 13.56 MHz RFID tags for the classification of corrosion progression over exposure time has been investigated. The complex impedance feature has been studied for the evaluation of corrosion stages in these mild steel samples. The measurement results show that the HF passive RFID-based sensing system can be used to classify general corrosion stage. Later, laser profilometry and PEC have been used to determine corrosion stage from a physical point of view. The measurement results obtained from the HF passive RFID-based sensing system correlated well with those of laser profilometry and PEC measurement. These investigations have also found that thickness, conductivity, permeability and permittivity can be used to identify stages of corrosion. However, the measurement results have shown that the reader is only capable of energising and reading a tag from a distance of up to 25 mm, which is not sufficient for the type of insulation used later in the study. Therefore, a microwave NDT system is proposed for inspection under insulation. The results of microwave NDT correlate well with those for permittivity. As expected, the tag and microwave signals vary at different stages of corrosion. The results demonstrate that the RFID system and microwave NDT have the ability to differentiate between all of the different stages of corrosion.

Due to the different thickness of insulation, lift-off effects are then considered. The effect of lift-off has been experimentally investigated in Chapter 5. These passive tags obtain all of their energy from the electromagnetic field generated by the reader coil.

Hence the tag signal as measured at the reader end is largely dependent on the relative distance between the coils of the reader and the tag. It has been demonstrated that changes in lift-off can mask variation in the tag's signal due to the different stages of corrosion. One proposed solution to this problem is to apply PCA to extract two features. This solution relies on the assumption that complex impedance is a function of both corrosion variance and lift-off variance. The collinearity between the two features with respect to lift-off is reduced by using PCA. The ability to obtain lift-off independent corrosion measurements using PCA has been demonstrated. The results show that the second principal component PC2 is very robust with respect to lift-off variance. Furthermore, the separated defect pattern reconstruction using NMF method is applied to tackle the problem of the effect of lift-off variation on microwave NDT measurement. The results show that the proposed method works effectively; therefore, a more robust feature can be used for defect detection at large values of lift-off. Several experiments have been carried out to investigate the effectiveness of the microwave NDT method.

In the Chapter 6, an experimental study is conducted into defect detection under thick insulation in order to demonstrate the performance of the proposed microwave NDT system in a more realistic environment. Three insulated steel plates, each with different thicknesses of the insulation layer, contained defects in order to simulate the development of corrosion. The ability of microwave signals to penetrate non-conductive material makes microwave techniques attractive for inspection for the presence of defects under thick insulation layers. The reflection coefficient has been investigated to produce images of these defects. These images indicate the ability of microwaves to size and locate defects under insulation. Simple C-scans reveal the potential of this technique as a tool to inspect the integrity of insulated steel samples. Defect location has been demonstrated to be an easy task to achieve using the suggested technique. In addition to detecting and locating defects, the influence of variations in the thickness of

the insulation layer has been reduced using this technique in conjunction with PCA. A new approach to defect classification and characterisation based on the linear sweep frequency and PCA has also been investigated. PCA globally analyses across the whole frequency range, and therefore avoids the interpolation issue faced by conventional Fourier-based methods. The performance of the proposed method has been evaluated, and it largely eliminates the influence of roughness and lift-off effects.

7.2 Further Work

Future work with the RFID and microwave NDT system will be geared towards improvements in handling other challenges related to insulated materials. These improvements will also be important steps towards commercial feasibility.

7.2.1 RFID-based Sensing Investigation

The inability of the RFID system to monitor large areas limits its potential field of application. Solving this problem requires the redesign of the tag unit [176, 177]. Additionally, the inability of the RFID sensing system to handle large lift-off requires investigations into whether or not carefully placed ferrite material near the tags will improve reading range. New tags employ a dual operational frequencies, which combines HF and UHF, to improve the reliability [178].

HF passive RFID-based monitoring networks can be formed by combining passive RFID tag with SAW (surface acoustic wave) [179]. With cost-efficient and lower power consumption, RFID based approaches may represent a revolutionary solution for the condition and intelligent structural health monitoring of railways, in-service nuclear power plants and aerospace applications [180].

Further studies of RFID sensing should be considered for remote healthcare. People are looking for adopting new technologies to lower their medical costs, which could create

lucrative opportunities for technology providers. RFID-based medical sensors are used for monitoring daily health status via remote applications to lower delivery costs of healthcare [181]. As well as cost-effective passive RFID tags with low power consumption, other sensors could easily be connected for multiple-purpose sensing. In addition, new features of RFID tags based on advanced signal processing can be used for human body temperature and other measurements.

7.2.2 Microwave NDT-based Sensing and Imaging Investigation

For corrosion detection under insulation, the use of microwave NDT can be extended to the detection of water in the insulation layer, since water is a cause of corrosion [182]. Meanwhile, samples with insulation related corrosion can be created to determine whether or not blisters, delamination and other insulation defects can be distinguished with microwave NDT [141]. These different types of defects may look similar when analysing the features of microwave signal. Therefore, new features are required as well as looking into how the responses in insulation to corrosion change over time, such as if blisters may appear as sudden sharp changes compared to defects on metal. For the microwave scanning process over large areas, compressive sensing could also be adopted to reduce scanning time [183].

Future work will also involve looking into methods to obtain quantitative information about conditions under the surface of steel, such as variations in physical parameters. This can be achieved by correlation using advanced feature extraction methods [184].

Furthermore, microwave imaging for medical applications has been of interest to researchers for many years. Microwave scanning can provide images of the distributions of electrical property in the human body. The physiological state of various tissues can be related to their electrical properties. Therefore, one further area microwave NDT could be used for would be to indicate the changing electrical properties of tissues of

interest. In this case, cancer detection based on microwave NDT is a promising area [185].

References

[1] Z. Ahmad, *Principles of Corrosion Engineering and Corrosion Control*, Butterworth Heinemann, 2006.

[2] R. W. Revie, and H. H. Uhlig, *Corrosion and Corrosion Control: An Introduction to Corrosion Science and Engineering: Fourth Edition*, 2008.

[3] N. P. Padture, M. Gell, and E. H. Jordan, "Thermal barrier coatings for gas-turbine engine applications," *Science,* vol. 296, no. 5566, pp. 280-284, 2002.

[4] BBC. [Online]. http://www.bbc.co.uk/news/world-asia-china-25050300 [Accessed: June. 2014]

[5] R. McConnell, "Volatile corrosion inhibitors offer effective protection for processing and shipment of metal-based products," *Metal Finishing,* vol. 106, no. 9, pp. 23-27, 2008.

[6] V. G. M. Annamdas, and C. K. Soh, "Application of electromechanical impedance technique for engineering structures: Review and future issues," *Journal of Intelligent Material Systems and Structures,* vol. 21, no. 1, pp. 41-59, 2010.

[7] W. K. Lu, R. L. Elsenbaumer, and B. Wessling, "Corrosion protection of mild steel by coatings containing polyaniline," *Synthetic Metals,* vol. 71, no. 1-3, pp. 2163-2166, 1995.

[8] P. Priyada, M. Margret, R. Ramar *et al.*, "Intercomparison of gamma scattering, gammatography, and radiography techniques for mild steel nonuniform corrosion detection," *Review of Scientific Instruments,* vol. 82, no. 3, pp. 035115-035115-8, 2011.

[9] P. Huthwaite, R. Ribichini, P. Cawley *et al.*, "Mode selection for corrosion detection in pipes and vessels via guided wave tomography," *IEEE Transactions on Ultrasonics, Ferroelectrics and Frequency Control,* vol. 60, no. 6, pp. 1165-1177, 2013.

[10] J. Ou, and H. Li, "Structural health monitoring in mainland china: Review and future trends," *Structural Health Monitoring,* vol. 9, no. 3, pp. 219-231, 2010.

[11] P. Rizzo, "Water and wastewater pipe nondestructive evaluation and health monitoring: A review," *Advances in Civil Engineering,* vol. 2010, 2010.

[12] R. Baboian, *Corrosion tests and standards : application and interpretation*, 2nd ed., West Conshohocken, PA: ASTM International, 2005.

[13] P. A. Schweitzer, *Metallic materials : physical, mechanical, and corrosion properties*, New York: M. Dekker, 2003.

[14] Q. Xianming, and C. Zhi Ning, "Proximity Effects of Metallic Environments on High Frequency RFID Reader Antenna: Study and Applications," *IEEE Transactions on Antennas and Propagation,* vol. 55, no. 11, pp. 3105-3111, 2007.

[15] C. C. Su, M. H. Chen, and S. H. Chang, “Investigation on the corrosion behavior of materials under insulation,” *Journal of Chinese Corrosion Engineering,* vol. 26, no. 4, pp. 203-210, 2012.

[16] M. G. Fontana, *Corrosion Engineering*: Tata McGraw-Hill, 2005.

[17] Y. Tan, “An overview of techniques for characterizing inhomogeneities in organic surface films and underfilm localized corrosion,” *Progress in Organic Coatings,* vol. 76, no. 5, pp. 791-803, 2013.

[18] E. Ghali, W. Dietzel, and K. U. Kainer, “Testing of general and localized corrosion of magnesium alloys: A critical review,” *Journal of Materials Engineering and Performance,* vol. 13, no. 5, pp. 517-529, 2004.

[19] R. G. Kelly, J. R. Scully, D. Shoesmith, and R. G. Buchheit, *Electrochemical Techniques in Corrosion Science and Engineering*: Taylor & Francis, 2002.

[20] G. S. Frankel, “Pitting corrosion of metals: A review of the critical factors,” *Journal of the Electrochemical Society,* vol. 145, no. 6, pp. 2186-2198, 1998.

[21] G. S. Frankel, and N. Sridhar, “Understanding localized corrosion,” *Materials Today,* vol. 11, no. 10, pp. 38-44, 2008.

[22] N. Larché, D. Thierry, V. Debout *et al.*, “Crevice corrosion of duplex stainless steels in natural and chlorinated seawater,” *Revue de Metallurgie. Cahiers D'Informations Techniques,* vol. 108, no. 7-8, pp. 451-463, 2011.

[23] S. Ramamurthy, and A. Atrens, “Stress corrosion cracking of high-strength steels,” *Corrosion Reviews,* vol. 31, no. 1, pp. 1-31, 2013.

[24] M. Miyasaka, “Corrosion and corrosion protection of seawater pumps,” *Zairyo to Kankyo/ Corrosion Engineering,* vol. 61, no. 12, pp. 464-470, 2012.

[25] R. Tems, and A. Al-Zahrani, "Cost of corrosion in gas sweetening and fractionation plants," *NACE International,* pp. 064441-0644412, 2006.

[26] M. Hattori, A. Nishikata, and T. Tsuru, “EIS study on degradation of polymer-coated steel under ultraviolet radiation,” *Corrosion Science,* vol. 52, no. 6, pp. 2080-2087, 2010.

[27] V. F. Lvovich, *Impedance Spectroscopy: Applications to Electrochemical and Dielectric Phenomena,* John Wiley & Sons, 2012.

[28] S. Shead, “Pigs in the pipes,” *Engineer,* no. NOVEMBER, pp. 35-36, 2013.

[29] K. K. Tandon, “MFL tool hardware for pipeline inspection,” *Materials Performance,* vol. 36, no. 2, pp. 75-79, 1997.

[30] P. Tims, and O. Wilson, “When is corrosion not corrosion? A decade of MFL pipeline inspection,” *Pipes and Pipelines International,* vol. 47, no. 6, pp. 36-48, 2002.

[31] A. A. Carvalho, J. M. A. Rebello, L. V. S. Sagrilo, C. S. Camerini, and I. V. J. Miranda, “MFL signals and artificial neural networks applied to detection and

classification of pipe weld defects," *NDT and E International,* vol. 39, no. 8, pp. 661-667, 2006.

[32] J. Carew, A. Al-Hashem, E. A. Al-Mohemeed, "Intelligent Pigging of a seawater injection pipeline in kuwait," *Materials Performance,* vol. 48, no. 10, pp. 44-47, 2009.

[33] Y. Yao, S. T. E. Tung, and B. Glisic, "Crack detection and characterization techniques-an overview," *Structural Control and Health Monitoring,* 2014.

[34] C. C. Lin, "Structural Control and Health Monitoring: Editorial," *Structural Control and Health Monitoring,* vol. 16, no. 1, pp. 1-6, 2009.

[35] C. K. Lee, J. J. Scholey, S. E. Worthington *et al.*, "Acoustic emission from pitting corrosion in stressed stainless steel plate," *Corrosion Engineering Science and Technology,* vol. 43, no. 1, pp. 54-63, 2008.

[36] G. Rannou, D. Thierry, and N. Le Bozec, "Ultrasonic monitoring of steel corrosion during accelerated corrosion testing and outdoor field exposures," *NACE International,* 2010.

[37] K. Edalati, N. Rastkhah, A. Kermani, "The use of radiography for thickness measurement and corrosion monitoring in pipes," *International Journal of Pressure Vessels and Piping,* vol. 83, no. 10, pp. 736-741, 2006.

[38] X. Li, S. Zhang, Z. Huang, "Fiber optics sensing technique for monitoring corrosion of steel in reinforced concrete," *Corrosion Science and Protection Technology,* vol. 11, no. 3, pp. 172-173, 1999.

[39] H. Ceylan, K. Gopalakrishnan, S. Kim, "Highway infrastructure health monitoring using micro-electromechanical sensors and systems (MEMS)," *Journal of Civil Engineering and Management,* vol. 19, no. SUPPL.1, pp. S188-S201, 2013.

[40] C. Barbosa, N. Costa, L. A. Ferreira, "Weldable fibre Bragg grating sensors for steel bridge monitoring," *Measurement Science and Technology,* vol. 19, no. 12, 2008.

[41] C. Hellier, *Handbook of Nondestructive Evaluation*, Mcgraw-hill, 2001.

[42] Y. He, G. Y. Tian, H. Zhang, "Steel Corrosion Characterization Using Pulsed Eddy Current Systems," *IEEE Sensors Journal,* vol. 12, no. 6, pp. 2113-2120, 2012.

[43] H. Shaikh, N. Sivaibharasi, B. Sasi, "Use of eddy current testing method in detection and evaluation of sensitisation and intergranular corrosion in austenitic stainless steels," *Corrosion Science,* vol. 48, no. 6, pp. 1462-1482, 2006.

[44] T. Chen, G. Y. Tian, A. Sophian, "Feature extraction and selection for defect classification of pulsed eddy current NDT," *NDT and E International,* vol. 41, no. 6, pp. 467-476, 2008.

[45] G. Chen, and Y. Tang, "Aero-engine interior damage recognition based on texture features of borescope image," *Yi Qi Yi Biao Xue Bao/Chinese Journal of Scientific Instrument,* vol. 29, no. 8, pp. 1709-1713, 2008.

[46] J. R. Casas, and P. J. S. Cruz, "Fiber optic sensors for bridge monitoring," *Journal of Bridge Engineering,* vol. 8, no. 6, pp. 362-373, 2003.

[47] R. C. Tennyson, N. Banthia, E. Rivera, "Monitoring structures using long gauge length fibre optic sensors," *Canadian Journal of Civil Engineering,* vol. 34, no. 3, pp. 422-429, 2007.

[48] R. H. Scott, P. Banerji, S. Chikermane, "Commissioning and evaluation of a fiber-optic sensor system for bridge monitoring," *IEEE Sensors Journal,* vol. 13, no. 7, pp. 2555-2562, 2013.

[49] S. K. A. K. Bey, C. C. C. Lam, T. Sun, "Long period grating pair chloride ion sensor for early corrosion prevention," *Journal of Physics: Conference Series,* vol. 85, no. 1, pp. 012022, 2007.

[50] Z. Xuefeng, C. Yanjun, W. Heming, "Research on corrosion detection for steel reinforced concrete structures using the fiber optical white light interferometer sensing technique," *Smart Materials and Structures,* vol. 22, no. 6, pp. 065014, 2013.

[51] C. McCague, M. Fabian, M. Karimi, "Novel Sensor Design Using Photonic Crystal Fibres for Monitoring the Onset of Corrosion in Reinforced Concrete Structures," *Journal of Lightwave Technology,* vol. 32, no. 5, pp. 891-896, 2014.

[52] Y. K. Zhu, G. Y. Tian, R. S. Lu, and H. Zhang, "A review of optical NDT technologies," *Sensors,* vol. 11, no. 8, pp. 7773-7798, 2011.

[53] J. P. Komorowski, N. C. Bellinger, R. W. Gould, "Quantification of corrosion in aircraft structures with double pass retroreflection," *Canadian Aeronautics and Space Journal,* vol. 42, no. 2, pp. 76-82, 1996.

[54] D. S. Forsyth, J. P. Komorowski, A. Marincak, "The edge of light enhanced optical ndi technique," *Canadian Aeronautics and Space Journal,* vol. 43, no. 4, pp. 231-235, 1997.

[55] K. Habib, "Laser optical interferometry as NDT methods for cleaner and sustainable desalination plants: Pitting and crevice corrosion," *Desalination,* vol. 166, no. 1-3, pp. 171-190, 2004.

[56] P. Day, "An automated ultrasonic inspection method for thickness checking of dryer cylinders for paper making machines," *Insight: Non-Destructive Testing and Condition Monitoring,* vol. 45, no. 9, pp. 628-631, 2003.

[57] A. Groysman, "Corrosion monitoring," *Corrosion Reviews,* vol. 27, no. 4-5, pp. 205-343, 2009.

[58] D. Tuzzeo, and F. Lanza Di Scalea, "Noncontact air-coupled guided wave ultrasonics for detection of thinning defects in aluminum plates," *Research in Nondestructive Evaluation,* vol. 13, no. 2, pp. 61-77, 2001.

[59] F. Hernandez-Valle, A. R. Clough, and R. S. Edwards, "Stress corrosion cracking detection using non-contact ultrasonic techniques," *Corrosion Science,* vol. 78, no. 0, pp. 335-342, 2014.

[60] R. S. Edwards, A. Sophian, S. Dixon, “Dual EMAT and PEC non-contact probe: Applications to defect testing,” *NDT and E International,* vol. 39, no. 1, pp. 45-52, 2006.

[61] J. Granillo, and M. Moles, “Portable phased array applications,” *Materials Evaluation,* vol. 63, no. 4, pp. 394-404, 2005.

[62] N. Kono, A. Baba, and K. Ehara, “Ultrasonic multiple beam technique using single phased array probe for detection and sizing of stress corrosion cracking in austenitic welds,” *Materials Evaluation,* vol. 68, no. 10, pp. 1163-1170, 2010.

[63] D. Cerniglia, and A. Pantano, "Experimental and numerical method for nondestructive ultrasonic defect detection," *Nondestructive Testing: Methods, Analyses and Applications,* pp. 63-94, 2011.

[64] F. Hernandez-Valle, A. R. Clough, and R. S. Edwards, “Stress corrosion cracking detection using non-contact ultrasonic techniques,” *Corrosion Science,* vol. 78, pp. 335-342, 2014.

[65] M. Fregonese, H. Idrissi, H. Mazille, “Initiation and propagation steps in pitting corrosion of austenitic stainless steels: monitoring by acoustic emission,” *Corrosion Science,* vol. 43, no. 4, pp. 627-641, 2001.

[66] H. Mazille, R. Rothea, and C. Tronel, “An acoustic emission technique for monitoring pitting corrosion of austenitic stainless steels,” *Corrosion Science,* vol. 37, no. 9, pp. 1365-1375, 1995.

[67] A. Cakir, S. Tuncell, and A. Aydin, “AE response of 316L SS during SSR test under potentiostatic control,” *Corrosion Science,* vol. 41, no. 6, pp. 1175-1183, 1999.

[68] B. A. Lepine, and R. T. Holt, “An eddy current scanning method for the detection of corrosion under fasteners in thick skin aircraft structures,” *Canadian Aeronautics and Space Journal,* vol. 43, no. 1, pp. 28-33, 1997.

[69] G. Y. Tian, A. Sophian, D. Taylor, “Multiple sensors on pulsed eddy-current detection for 3-D subsurface crack assessment,” *IEEE Sensors Journal,* vol. 5, no. 1, pp. 90-96, 2005.

[70] M. Morozov, G. Y. Tian, and P. J. Withers, “Noncontact evaluation of the dependency of electrical conductivity on stress for various Al alloys as a function of plastic deformation and annealing,” *Journal of Applied Physics,* vol. 108, no. 2, pp. 024909, 2010.

[71] M. S. Safizadeh, Z. Liu, B. A. Lepine, “Multifrequency eddy current for the characterization of corrosion in multilayer structures,” *Materials Evaluation,* vol. 62, no. 5, pp. 535-539, 2004.

[72] A. Sophian, G. Y. Tian, D. Taylor, “Electromagnetic and eddy current NDT: A review,” *Insight: Non-Destructive Testing and Condition Monitoring,* vol. 43, no. 5, pp. 302-306, 2001.

[73] M. Afzal, and S. Udpa, “Advanced signal processing of magnetic flux leakage data obtained from seamless gas pipeline,” *NDT and E International,* vol. 35, no. 7, pp. 449-457, 2002.

[74] K. R. Larsen, “Improved magnetic flux leakage technology enhances pipeline inspection,” *Materials Performance,* vol. 47, no. 12, pp. 24-25, 2008.

[75] Y. Wang, X. Wang, and K. Ding, “Design and validation of a new pulsed magnetic flux leakage sensor for detecting corrosion on pipeline,” *Chinese Journal of Sensors and Actuators,* vol. 22, no. 10, pp. 1406-1412, 2009.

[76] D. M. Mittleman, R. H. Jacobsen, and M. C. Nuss, “T-ray imaging,” *IEEE Journal on Selected Topics in Quantum Electronics,* vol. 2, no. 3, pp. 679-692, 1996.

[77] S. P. Mickan, and X. C. Zhang, “T-ray sensing and imaging,” *International Journal of High Speed Electronics and Systems,* vol. 13, no. 2, pp. 601-676, 2003.

[78] R. F. Anastasi, and E. I. Madaras, "Terahertz NDE for under paint corrosion detection and evaluation." *AIP Conference Proceedings,* vol. 820, pp. 515-522, 2006.

[79] D. Zimdars, J. S. White, G. Stuk, “Large area terahertz imaging and non-destructive evaluation applications,” *Insight - Non-Destructive Testing and Condition Monitoring,* vol. 48, no. 9, pp. 537-539, 2006.

[80] C. P. Chiou, R. B. Thompson, W. P. Winfree *et al.*, “Modeling and Processing of Terahertz Imaging in Space Shuttle External Tank Foam Inspection,” *AIP Conference Proceedings,* vol. 820, no. 1, pp. 484-491, 2006.

[81] N. V. Nair, V. R. Melapudi, P. Vemulapalli, “A Wavelet Based Signal Processing Technique for Image Enhancement in Terahertz Imaging Data,” *AIP Conference Proceedings,* vol. 820, no. 1, pp. 492-499, 2006.

[82] A. Redo-Sanchez, N. Karpowicz, J. Xu, "Damage and defect inspection with terahertz waves." *Fourth International Workshop on Ultrasonic and Advanced Methods for Nondestructive Testing and Material Characterization*, pp. 67-78, 2006

[83] J. C. Aldrin, D. J. Roth, J. P. Seebo, “Protocol and Assessment of Signal Processing and Feature Extraction Methods for Terahertz NDE for Spray‐On Foam Insulation,” *AIP Conference Proceedings,* vol. 894, no. 1, pp. 432-439, 2007.

[84] V. Rebuffel, and J. M. Dinten, “Dual-energy X-ray imaging: Benefits and limits,” *Insight: Non-Destructive Testing and Condition Monitoring,* vol. 49, no. 10, pp. 589-594, 2007.

[85] G. Peix, P. Duvauchelle, and J. M. Letang, "X-ray Tomography in Industrial Non-destructive Testing," *Tomography*, pp. 215-238, 2010.

[86] C. Meola, and G. M. Carlomagno, “Application of infrared thermography to adhesion science,” *Journal of Adhesion Science and Technology,* vol. 20, no. 7, pp. 589-632, 2006.

[87] C. Garnier, M. L. Pastor, F. Eyma, “The detection of aeronautical defects in situ on composite structures using non destructive testing,” *Composite Structures,* vol. 93, no. 5, pp. 1328-1336, 2011.

[88] S. Sfarra, C. Ibarra-Castanedo, P. Avdelidis, “A comparative investigation for the nondestructive testing of honeycomb structures by holographic interferometry and infrared thermography,” *Journal of Physics: Conference Series,* vol. 214, 2010.

[89] C. Maierhofer, R. Arndt, M. Röllig, “Application of impulse-thermography for non-destructive assessment of concrete structures,” *Cement and Concrete Composites,* vol. 28, no. 4, pp. 393-401, 2006.

[90] L. Bai, B. Gao, G. Y. Tian, “Spatial and time patterns extraction of eddy current pulsed thermography using blind source separation,” *IEEE Sensors Journal,* vol. 13, no. 6, pp. 2094-2101, 2013.

[91] A. Yin, B. Gao, G. Yun Tian, “Physical interpretation and separation of eddy current pulsed thermography,” *Journal of Applied Physics,* vol. 113, no. 6, 2013.

[92] J. Wilson, G. Y. Tian, I. Z. Abidin, “Modelling and evaluation of eddy current stimulated thermography,” *Nondestructive Testing and Evaluation,* vol. 25, no. 3, pp. 205-218, 2010.

[93] Y. He, G. Y. Tian, M. Pan, “An investigation into eddy current pulsed thermography for detection of corrosion blister,” *Corrosion Science,* vol. 78, no. 0, pp. 1-6, 2014.

[94] A. Nishikata, Y. Ichihara, and T. Tsuru, “An application of electrochemical impedance spectroscopy to atmospheric corrosion study,” *Corrosion Science,* vol. 37, no. 6, pp. 897-911, 1995.

[95] P. L. Bonora, F. Deflorian, and L. Fedrizzi, “Electrochemical impedance spectroscopy as a tool for investigating underpaint corrosion,” *Electrochimica Acta,* vol. 41, no. 7-8, pp. 1073-1082, 1996.

[96] J. H. Wang, F. I. Wei, Y. S. Chang, “The corrosion mechanisms of carbon steel and weathering steel in SO2 polluted atmospheres,” *Materials Chemistry and Physics,* vol. 47, no. 1, pp. 1-8, 1997.

[97] Y. Ma, Y. Li, and F. Wang, “Corrosion of low carbon steel in atmospheric environments of different chloride content,” *Corrosion Science,* vol. 51, no. 5, pp. 997-1006, 2009.

[98] G. Salvago, G. Bollini, and P. L. Cavallotti, "Electrochemical evaluation of localized corrosion probability in stainless steel," *6th International Symposium on Electrochemical Methods in Corrosion Research,* pp. 933-954, 1998.

[99] M. J. Sundaresan, A. Ghoshal, W. N. Martin, “A continuous sensor to measure acoustic waves in plates,” *Journal of Intelligent Material Systems and Structures,* vol. 12, no. 1, pp. 41-56, 2001.

[100] A. Ghoshal, M. J. Sundaresan, M. J. Schulz, “Continuous Sensors for Structural Health Monitoring,” *American Society of Mechanical Engineers, Aerospace Division (Publication) AD,* vol. 60, pp. 387-397, 2000.

[101] M. Alamin, G. Y. Tian, A. Andrews, “Corrosion detection using low-frequency RFID technology,” *Insight: Non-Destructive Testing and Condition Monitoring,* vol. 54, no. 2, pp. 72-75, 2012.

[102] R. A. Potyrailo, C. Surman, S. Go, “Development of radio-frequency identification sensors based on organic electronic sensing materials for selective detection of toxic vapors,” *Journal of Applied Physics,* vol. 106, no. 12, 2009.

[103] K. Finkenzeller, *RFID handbook : fundamentals and applications in contactless smart cards and identification,* 2nd ed., Chichester, England ; Hoboken, N.J.: Wiley, 2003.

[104] B. Nath, F. Reynolds, and R. Want, "RFID technology and applications," *IEEE Pervasive Computing,* vol. 5, no. 1, pp. 22-24, 2006.

[105] J. M. Lin, P. K. Chang, and Z. Q. Hou, "Integrating microarray probes and amplifier on an active rfid tag for biosensing and monitor system design," *Biomedical Engineering - Applications, Basis and Communications,* vol. 21, no. 6, pp. 421-425, 2009.

[106] H. Chu, G. Wu, J. Chen, "Design and simulation of self-powered radio frequency identification (RFID) tags for mobile temperature monitoring," *Science China Technological Sciences,* vol. 56, no. 1, pp. 1-7, 2013.

[107] S. Preradovic, N. C. Karmakar, and I. Balbin, "RFID transponders," *IEEE Microwave Magazine,* vol. 9, no. 5, pp. 90-103, 2008.

[108] B. Wang, M. K. Law, A. Bermak, "A passive RFID tag embedded temperature sensor with improved process spreads immunity for a-30℃ to 60℃ sensing range," *IEEE Transactions on Circuits and Systems I: Regular Papers,* vol. 61, no. 2, pp. 337-346, 2014.

[109] E. M. Amin, M. S. Bhuiyan, N. C. Karmakar, "Development of a Low Cost Printable Chipless RFID Humidity Sensor," *IEEE Sensors Journal,* vol. 14, no. 1, pp. 140-149, 2014.

[110] S. Merilampi, T. Björninen, L. Ukkonen, "Embedded wireless strain sensors based on printed RFID tag," *Sensor Review,* vol. 31, no. 1, pp. 32-40, 2011.

[111] S. D. Nguyen, T. T. Pham, E. F. Blanc, "Approach for quality detection of food by RFID-based wireless sensor tag," *Electronics Letters,* vol. 49, no. 25, pp. 1588-1589, 2013.

[112] I. M. Steinberg, and M. D. Steinberg, "Radio-frequency tag with optoelectronic interface for distributed wireless chemical and biological sensor applications," *Sensors and Actuators, B: Chemical,* vol. 138, no. 1, pp. 120-125, 2009.

[113] G. Marrocco, "RFID antennas for the UHF remote monitoring of human subjects," *IEEE Transactions on Antennas and Propagation,* vol. 55, no. 6 II, pp. 1862-1870, 2007.

[114] R. A. Potyrailol, W. G. Morris, T. Sivavec, "RFID sensors based on ubiquitous passive 13.56-MHz RFID tags and complex impedance detection," *Wireless Communications and Mobile Computing,* vol. 9, no. 10, pp. 1318-1330, 2009.

[115] R. A. Potyrailo, H. Mouquin, and W. G. Morris, "Position-independent chemical quantitation with passive 13.56-MHz radio frequency identification (RFID) sensors," *Talanta,* vol. 75, no. 3, pp. 624-628, 2008.

[116] B. Carkhuff, and R. Cain, "Corrosion sensors for concrete bridges," *IEEE Instrumentation & Measurement Magazine,* vol. 6, no. 2, pp. 19-24, 2003.

[117] W. Leon-Salas, S. Kanneganti, and C. Halmen, "Development of a smart RFID-based corrosion sensor." *IEEE Sensors Journal*, pp. 534-537, 2011.

[118] M. Alamin, G. Y. Tian, A. Andrews, "Corrosion detection using low-frequency RFID technology," *Insight-Non-Destructive Testing and Condition Monitoring,* vol. 54, no. 2, pp. 72-75, 2012.

[119] N. N. Qaddoumi, W. M. Saleh, and M. Abou-Khousa, "Innovative Near-Field Microwave Nondestructive Testing of Corroded Metallic Structures Utilizing Open-Ended Rectangular Waveguide Probes," *IEEE Transactions on Instrumentation and Measurement,* vol. 56, no. 5, pp. 1961-1966, 2007.

[120] A. Redo-Sanchez, J. Tejada, and X. Bohigas, "Bubble Detector in Polyurethane Applications Based on a Microwave System," *IEEE Sensors Journal,* vol. 6, no. 4, pp. 939-944, 2006.

[121] M. Bogosanovic, A. Al Anbuky, and G. W. Emms, "Microwave Non-Destructive Testing of Wood Anisotropy and Scatter," *IEEE Sensors Journal,* vol. 13, no. 1, pp. 306-313, 2012.

[122] S. Kharkovsky, and R. Zoughi, "Microwave and millimeter wave nondestructive testing and evaluation - Overview and recent advances," *IEEE Instrumentation & Measurement Magazine,* vol. 10, no. 2, pp. 26-38, 2007.

[123] Z. W. Wang, Z. MengChu, G. G. Slabaugh, "Automatic Detection of Bridge Deck Condition From Ground Penetrating Radar Images," *IEEE Transactions on Automation Science and Engineering,* vol. 8, no. 3, pp. 633-640, 2011.

[124] P. Joongsuk, and C. Nguyen, "An ultrawide-band microwave radar sensor for nondestructive evaluation of pavement subsurface," *IEEE Sensors Journal,* vol. 5, no. 5, pp. 942-949, 2005.

[125] J. Han, and C. Nguyen, "Development of a Tunable Multiband UWB Radar Sensor and Its Applications to Subsurface Sensing," *IEEE Sensors Journal,* vol. 7, no. 1, pp. 51-58, 2007.

[126] P. Joongsuk, and C. Nguyen, "Development of a new millimeter-wave integrated-circuit sensor for surface and subsurface sensing," *IEEE Sensors Journal,* vol. 6, no. 3, pp. 650-655, 2006.

[127] Z. Abbas, Y. You Kok, A. H. Shaari, "Complex permittivity and moisture measurements of oil palm fruits using an open-ended coaxial sensor," *IEEE Sensors Journal,* vol. 5, no. 6, pp. 1281-1287, 2005.

[128] C. Y. Yeh, and R. Zoughi, "Sizing technique for slots and surface cracks in metals," *Materials Evaluation,* vol. 53, no. 4, pp. 496-501, 1995.

[129] Y. Chin-Yung, and R. Zoughi, "A novel microwave method for detection of long surface cracks in metals," *IEEE Transactions on Instrumentation and Measurement,* vol. 43, no. 5, pp. 719-725, 1994.

[130] C. Huber, H. Abiri, S. I. Ganchev, "Modeling of surface hairline-crack detection in metals under coatings using an open-ended rectangular waveguide," *IEEE*

Transactions on Microwave Theory and Techniques, vol. 45, no. 11, pp. 2049-2057, 1997.

[131] C. Huber, H. Abiri, S. I. Ganchev, “Analysis of the “Crack characteristic signal” using a generalized scattering matrix representation,” *IEEE Transactions on Microwave Theory and Techniques,* vol. 45, no. 4, pp. 477-484, 1997.

[132] F. Mazlumi, S. H. H. Sadeghi, and R. Moini, “Analysis technique for interaction of rectangular open-ended waveguides with surface cracks of arbitrary shape in metals,” *NDT and E International,* vol. 36, no. 5, pp. 331-338, 2003.

[133] C. Maierhofer, “Nondestructive Evaluation of Concrete Infrastructure with Ground Penetrating Radar,” *Journal of Materials in Civil Engineering,* vol. 15, no. 3, pp. 287-297, 2003.

[134] J. T. Case, S. Kharkovsky, R. Zoughi, “Millimeter Wave Holographical Inspection of Honeycome Composites,” *AIP Conference Proceedings,* vol. 975, no. 1, pp. 970-975, 2008.

[135] K. Arunachalam, V. R. Melapudi, L. Udpa, “Microwave NDT of cement-based materials using far-field reflection coefficients,” *NDT and E International,* vol. 39, no. 7, pp. 585-593, 2006.

[136] O. Büyüköztürk, and T. Y. Yu, “Far-field radar NDT technique for detecting GFRP debonding from concrete,” *Construction and Building Materials,* vol. 23, no. 4, pp. 1678-1689, 2009.

[137] B. Gao, H. Zhang, W. L. Woo, “Smooth Nonnegative Matrix Factorization for Defect Detection Using Microwave Nondestructive Testing and Evaluation,” *IEEE Transactions on Instrumentation and Measurement,* vol. 63, no. 4, pp. 923-934, 2013.

[138] H. Zhang, B. Gao, G. Y. Tian, “Metal defects sizing and detection under thick coating using microwave NDT,” *NDT and E International,* vol. 60, pp. 52-61, 2013.

[139] M. A. Abou-Khousa, S. Kharkovsky, and R. Zoughi, “Novel Near-Field Millimeter-Wave Differential Probe Using a Loaded Modulated Aperture,” *IEEE Transactions on Instrumentation and Measurement,* vol. 58, no. 5, pp. 1273-1282, 2009.

[140] M. T. Ghasr, S. Kharkovsky, R. Zoughi, “Comparison of near-field millimeter-wave probes for detecting corrosion precursor pitting under paint,” *IEEE Transactions on Instrumentation and Measurement,* vol. 54, no. 4, pp. 1497-1504, 2005.

[141] N. N. Qaddoumi, A. H. El-Hag, and Y. Saker, “Outdoor Insulators Testing Using Artificial Neural Network-Based Near-Field Microwave Technique,” *IEEE Transactions on Instrumentation and Measurement,* vol. 63, no. 2, pp. 260-266, 2014.

[142] H. Carreon, "Nondestructive materials characterization by magnetic sensing," *Journal of Applied Physics,* vol. 88, pp. 6495-6500, 2011.

[143] K. Finkenzeller, *RFID Handbook: Fundamentals and Applications in Contactless Smart Cards, Radio Frequency Identification and near-Field Communication,* 2nd ed., N.J.: Wiley, 2003.

[144] R. A. Potyrailo, C. Surman, S. Go, “Development of radio-frequency identification sensors based on organic electronic sensing materials for selective detection of toxic vapors,” *Journal of Applied Physics,* vol. 106, no. 12, pp. 124902-6, 2009.

[145] N. Canter, “Tech beat: Conductivity in minerals,” *Tribology and Lubrication Technology,* vol. 64, no. 7, pp. 14-15, 2008.

[146] N. Guskos, G. J. Papadopoulos, V. Likodimos, “Photoacoustic, EPR and electrical conductivity investigations of three synthetic mineral pigments: Hematite, goethite and magnetite,” *Materials Research Bulletin,* vol. 37, no. 6, pp. 1051-1061, 2002.

[147] A. Earnshaw, and N. Greenwood, *Chemistry of the Elements*: Elsevier Science & Technology Books, 1996.

[148] R. A. Potyrailo, and C. Surman, “A passive radio-frequency identification (RFID) gas sensor with self-correction against fluctuations of ambient temperature,” *Sensors and Actuators, B: Chemical*, vol. 185, pp. 587-593, 2013.

[149] R. Zoughi, and S. Bakhtiari, “Microwave nondestructive detection and evaluation of disbonding and delamination in layered-dielectric slabs,” *IEEE Transactions on Instrumentation and Measurement,* vol. 39, no. 6, pp. 1059-1063, 1990.

[150] M. Sayar, D. Seo, and K. Ogawa, “Non-destructive microwave detection of layer thickness in degraded thermal barrier coatings using K- and W-band frequency range,” *NDT and E International,* vol. 42, no. 5, pp. 398-403, 2009.

[151] S. Bakhtiari, N. Qaddoumi, S. I. Ganchev, “Microwave noncontact examination of disbond and thickness variation in stratified composite media,” *IEEE Transactions on Microwave Theory and Techniques,* vol. 42, no. 3, pp. 389-395, 1994.

[152] J. Ma, W. Che, and N. Mao, “A 2D near-field microwave diversity imaging system in turntable mode,” *Microwave and Optical Technology Letters,* vol. 36, no. 5, pp. 356-359, 2003.

[153] C. Fu-Chiarng, and C. Weng Cho, "Code-division multiplexing and frequency-division multiplexing for nonlinear inverse scattering." *IEEE Antennas and Propagation Society International Symposium Conference*, vol. 3, pp. 2128-2131, 1999.

[154] R. Zoughi, and S. Kharkovsky, “Microwave and millimetre wave sensors for crack detection,” *Fatigue and Fracture of Engineering Materials and Structures,* vol. 31, no. 8, pp. 695-713, 2008.

[155] A. A. Afifi, and V. Clark, *Computer-aided multivariate analysis*, London: Chapman & Hall, 1996.

[156] C. Févotte, "Majorization-minimization algorithm for smooth Itakura-Saito nonnegative matrix factorization." *IEEE International Conference on Acoustics, Speech and Signal Processing Proceedings,* pp. 1980-1983, 2011.

[157] C. Févotte, N. Bertin, and J. L. Durrieu, “Nonnegative matrix factorization with the Itakura-Saito divergence: With application to music analysis,” *Neural Computation,* vol. 21, no. 3, pp. 793-830, 2009.

[158] S. Cruces-Alvarez, A. Cichocki, and L. Castedo-Ribas, "An iterative inversion approach to blind source separation," *IEEE Transactions on Neural Networks,* vol. 11, no. 6, pp. 1423-1437, 2000.

[159] D. D. Lee, and H. S. Seung, "Learning the parts of objects by non-negative matrix factorization," *Nature,* vol. 401, no. 6755, pp. 788-791, 1999.

[160] P. Paatero, and U. Tapper, "Positive matrix factorization: a non-negative factor model with optimal utilization of error estimates of data values," *Environmetrics,* vol. 5, no. 2, pp. 111-126, 1994.

[161] R. Kompass, "A generalized divergence measure for nonnegative matrix factorization," *Neural Computation,* vol. 19, no. 3, pp. 780-791, 2007.

[162] Y. Gotoh, H. Hirano, M. Nakano *et al.*, "Electromagnetic nondestructive testing of rust region in steel," *IEEE Transactions on Magnetics,* vol. 41, no. 10, pp. 3616-3618, 2005.

[163] D. de la Fuente, I. Díaz, J. Simancas, "Long-term atmospheric corrosion of mild steel," *Corrosion Science,* vol. 53, no. 2, pp. 604-617, 2011.

[164] S. Feliu, M. Morcillo, and S. Feliu Jr., "The prediction of atmospheric corrosion from meteorological and pollution parameters-I. Annual corrosion," *Corrosion Science,* vol. 34, no. 3, pp. 403-414, 1993.

[165] W. Hou, and C. Liang, "Atmospheric corrosion prediction of steels," *Corrosion,* vol. 60, no. 3, pp. 313-322, 2004.

[166] Y. Ma, Y. Li, and F. Wang, "The atmospheric corrosion kinetics of low carbon steel in a tropical marine environment," *Corrosion Science,* vol. 52, no. 5, pp. 1796-1800, 2010.

[167] M. Morozov, G. Y. Tian, and P. J. Withers, "Noncontact evaluation of the dependency of electrical conductivity on stress for various Al alloys as a function of plastic deformation and annealing," *Journal of Applied Physics,* vol. 108, no. 2, 2010.

[168] N. Qaddoumi, L. Handjojo, T. Bigelow, "Microwave Corrosion Detection Using Open Ended Rectangular Waveguide Sensors," *Materials Evaluation,* vol. 58, no. 2, pp. 178-184, 2000.

[169] N. Qaddoumi, E. Ranu, J. D. McColskey, "Microwave detection of stress-induced fatigue cracks in steel and potential for crack opening determination," *Research in Nondestructive Evaluation,* vol. 12, no. 2, pp. 87-103, 2000.

[170] A. M. Yadegari, R. Moini, S. H. H. Sadeghi, "Output signal prediction of an open-ended rectangular waveguide probe when scanning cracks at a non-zero lift-off," *NDT and E International,* vol. 43, no. 1, pp. 1-7, 2010.

[171] N. Qaddoumi, E. Ranu, J. D. McColskey, "Microwave Detection of Stress-Induced Fatigue Cracks in Steel and Potential for Crack Opening Determination," *Research in Nondestructive Evaluation,* vol. 12, no. 2, pp. 87-104, 2000.

[172] G. Slekas, Z. Kancleris, and R. Ciegis, "Sensitivity of Asymmetrically Necked Planar Millimeter-Wave Detectors," *IEEE Sensors Journal,* vol. 13, no. 4, pp. 1143-1147, 2013.

[173] C. Huber, and R. Zoughi, "Detecting stress and fatigue cracks," *IEEE Potentials,* vol. 15, no. 4, pp. 20-24, 1996.

[174] A. McClanahan, S. Kharkovsky, A. R. Maxon, "Depth Evaluation of Shallow Surface Cracks in Metals Using Rectangular Waveguides at Millimeter-Wave Frequencies," *IEEE Transactions on Instrumentation and Measurement,* vol. 59, no. 6, pp. 1693-1704, 2010.

[175] S. S. Ahmed, A. Schiessl, F. Gumbmann, "Advanced Microwave Imaging," *IEEE Microwave Magazine,* vol. 13, no. 6, pp. 26-43, 2012.

[176] E. Amin, J. Saha, and N. Karmakar, "Smart Sensing Materials for Low-Cost Chipless RFID Sensor," *IEEE Sensors Journal,* vol. 14, no. 7, pp. 2198-2207, 2014.

[177] O. O. Rakibet, C. V. Rumens, J. C. Batchelor, "Epidermal Passive RFID Strain Sensor for Assisted Technologies," *IEEE Antennas and Wireless Propagation Letters,* vol. 13, pp. 814-817, 2014.

[178] P. Iliev, P. Le Thuc, C. Luxey *et al.*, "Dual-band HF-UHF RFID tag antenna," *Electronics Letters,* vol. 45, no. 9, pp. 439-441, 2009.

[179] V. P. Plessky, and L. M. Reindl, "Review on SAW RFID tags," *IEEE Transactions on Ultrasonics, Ferroelectrics and Frequency Control,* vol. 57, no. 3, pp. 654-668, 2010.

[180] W. C. Wilson, D. C. Malocha, N. Y. Kozlovski, "Orthogonal Frequency Coded SAW Sensors for Aerospace SHM Applications," *IEEE Sensors Journal,* vol. 9, no. 11, pp. 1546-1556, 2009.

[181] G. Yang, L. Xie, M. Mantysalo, "A Health-IoT Platform Based on the Integration of Intelligent Packaging, Unobtrusive Bio-Sensor and Intelligent Medicine Box," *IEEE Transactions on Industrial Informatics,* vol. 2, no. 2, pp. 1-10, 2014.

[182] R. E. Jones, F. Simonetti, M. J. S. Lowe, "Use of microwaves for the detection of water as a cause of corrosion under insulation," *Journal of Nondestructive Evaluation,* vol. 31, no. 1, pp. 65-76, 2012.

[183] D. Xiao, and Z. Yunhua, "A Novel Compressive Sensing Algorithm for SAR Imaging," *IEEE Journal of Selected Topics in Applied Earth Observations and Remote Sensing,* vol. 7, no. 2, pp. 708-720, 2014.

[184] R. Scapaticci, I. Catapano, and L. Crocco, "Wavelet-Based Adaptive Multiresolution Inversion for Quantitative Microwave Imaging of Breast Tissues," *IEEE Transactions on Antennas and Propagation,* vol. 60, no. 8, pp. 3717-3726, 2012.

[185] M. Elsdon, O. Yurduseven, and D. Smith, "Early stage breast cancer detection using indirect microwave holography," *Progress in Electromagnetics Research,* vol. 143, pp. 405-419, 2013.